Unraveling the link between Neuropathy Target Esterase NTE/SWS, lysosomal storage diseases, inflammation, abnormal fatty acid metabolism, and leaky brain barrier

Mariana I. Tsap[1], Andriy S. Yatsenko[1], Jan Hegermann[2], Bibiana Beckmann[3], Dimitrios Tsikas[3], Halyna R. Shcherbata[1, 4*]

[1] Institute of Cell Biochemistry, Hannover Medical School, Carl-Neuberg-Strasse 1, 30625, Hannover, Germany

[2] Institute of Functional and Applied Anatomy, Research Core Unit Electron Microscopy, Hannover Medical School, Carl-Neuberg-Strasse 1, 30625, Hannover, Germany

[3] Institute of Toxicology, Hannover Medical School, Carl-Neuberg-Strasse 1, 30625, Hannover, Germany

[4] Mount Desert Island Biological Laboratory, Bar Harbor, ME 04609, USA

* Corresponding author: Shcherbata.Halyna@mh-hannover.de

Keywords: age-dependent neurodegeneration, lysosomal storage disorder, lysosomes, blood-brain barrier, glia, inflammation, lipids, fatty acids, arachidonic acid, eicosanoids, NSAID, neurotoxicity, PNPLA6, neuropathy target esterase, *swiss cheese* gene, Drosophila model, inflammaging

Short summary:

Drosophila model reveals that NTE/SWS -associated neurodegeneration is a lysosomal storage disorder accompanied by a leaky brain permeability barrier, abnormal fatty acid metabolism, and inflammation

ABSTRACT

Mutations in Drosophila Swiss Cheese (SWS) gene or its vertebrate orthologue Neuropathy Target Esterase (NTE) lead to progressive neuronal degeneration in flies and humans. Despite its enzymatic function as a phospholipase is well-established, the molecular mechanism responsible for maintaining nervous system integrity remains unclear. In this study, we found that NTE/SWS is present in surface glia that forms the blood-brain-barrier (BBB) and that NTE/SWS is important to maintain its structure and permeability. Importantly, BBB glia-specific expression of Drosophila *NTE/SWS* or human NTE in the *sws* mutant background fully rescues surface glial organization and partially restores BBB integrity, suggesting a conserved function of NTE/SWS. Interestingly, *sws* mutant glia showed abnormal organization of plasma membrane domains and tight junction rafts accompanied by the accumulation of lipid droplets, lysosomes, and multilamellar bodies. Since the observed cellular phenotypes closely resemble the characteristics described in a group of metabolic disorders known as lysosomal storage diseases (LSDs), our data established a novel connection between NTE/SWS and these conditions. We found that mutants with defective BBB exhibit elevated levels of fatty acids, which are precursors of eicosanoids and are involved in the inflammatory response. Also, as a consequence of a permeable BBB, several innate immunity factors are upregulated in an age-dependent manner, while BBB glia-specific expression of NTE/SWS normalizes inflammatory response. Treatment with anti-inflammatory agents prevents the abnormal architecture of the BBB, suggesting that inflammation contributes to the maintenance of a healthy brain barrier. Considering the link between a malfunctioning BBB and various neurodegenerative diseases, gaining a deeper understanding of the molecular mechanisms causing inflammation due to a defective BBB could help to promote the use of anti-inflammatory therapies for age-related neurodegeneration.

INTRODUCTION

Aging is the major risk factor for neurodegenerative conditions, a group of disorders characterized by the progressive degeneration and dysfunction of the nervous system, which includes Alzheimer's and Parkinson's disease, amyotrophic lateral sclerosis, frontotemporal dementia, and many others. These diseases typically result in the gradual loss of cognitive function, movement control, and other neurological functions. The exact causes of neurodegenerative diseases are often complex and not fully understood, but they can involve a combination of genetic, environmental, and lifestyle factors.

Growing evidence suggests that inflammation plays a crucial role in age-related neurodegenerative diseases [1-5]. Older organisms frequently develop chronic, low-grade inflammation, a condition often named inflammaging, which is characterized by a sustained increase in inflammatory markers without apparent infection or injury [6-9]. This phenomenon presents a potential target for anti-inflammatory therapy in neurodegenerative disorders. Strategies involving modulation of inflammatory signaling pathways have shown promise in both animal models and clinical trials, offering hopeful prospects for neurodegenerative disease therapy [5]. While research aims to identify therapeutic targets to alleviate the impact of inflammaging on neurological health, a more in-depth understanding of the molecular mechanisms underlying inflammaging is needed.

One feature associated with neuroinflammatory degenerative diseases is dysfunction of the blood-brain barrier (BBB) [10]. Disruption of the BBB has been observed in patients with numerous neurodegenerative diseases [11-17]. Since the BBB plays a crucial role in maintaining the homeostasis of the brain environment, its disruption allows the infiltration of immune cells and molecules that can trigger and sustain inflammatory responses within the brain [18].

Furthermore, dysfunction in lysosomal pathways also has been implicated in Alzheimer's and Parkinson's disease and many other neurodegenerative disorders [19]. The lysosome-endosomal system is tightly associated with the maintenance of cell homeostasis and viability, regulation of cell death, oncogenesis, autophagy and inflammation [20]. In particular, lysosomes are cellular organelles responsible for degrading cellular waste and maintaining cellular health. Dysfunction of lysosomal processes can lead to the accumulation of damaged cellular components and trigger inflammatory responses, contributing to the overall inflammaging phenomenon [20, 21].

Fatty acid metabolism is another aspect linked to inflammaging [22-24]. Changes in lipid composition and metabolism, particularly an increase in pro-inflammatory fatty acids, have been observed in inflammaging. These alterations can contribute to the perpetuation of inflammatory signaling and potentially impact neurodegenerative conditions [25, 26]. Thus, understanding the interplay between the BBB, lysosomes, fatty acid metabolism and inflammaging is crucial for unravelling the intricate mechanisms involved in age-related neurodegenerative diseases.

In addition, human age-related neurodegenerative diseases can be accelerated by different stresses, which include a wide array of factors such as infection, trauma, diet, or exposure to toxic substances. Interestingly, abnormalities in the human Neuropathy Target Esterase (NTE), encoded by PNPLA6 (Patatin Like Phospholipase Domain Containing 6) gene are linked to both neurodegeneration types: toxin-induced and hereditary. NTE is a transmembrane protein anchored to the cytoplasmic face of the endoplasmic reticulum and acts as a phospholipase that regulates lipid membrane homeostasis [27-29]. Continuous inhibition of NTE activity by the organophosphorus

compound tri-ortho-cresyl phosphate (TOCP) causes axonal degeneration in the central nervous system (CNS) and peripheral nervous system (PNS), a neuropathy that was consequently named Organophosphate-Induced Delayed Neuropathy (OPIDN) [30, 31]. Moreover, mutations in the NTE gene cause Gordon-Holmes or Boucher-Neuhäuser syndromes [32-35] and a motor neuron disease called hereditary spastic paraplegia type 39 (HSP 39), in which distal parts of long spinal axons degenerate, leading to limb weakness and paralysis [36, 37]. Genetically, HSP classification is based on the genes of origin called Spastic Paraplegia Genes, which is a large group (>80) of genes [38]. Over the past few years, research has shown that HSP is associated with endo-lysosomal system abnormalities [39-43].

Human studies play a crucial role in understanding the real-world impact of aging and neurodegeneration. However, for various reasons like a long lifespan, ethical considerations, heterogeneity, cohort effects, limited controls, etc., humans may not always be ideal subjects for age-related research. To address these challenges, human studies are often complemented by research in model organisms, providing a comprehensive perspective on aging mechanisms and interventions. In particular, modelling human neurodegenerative diseases in various model organisms can provide us with needed knowledge about the first hallmarks of neurodegeneration and also signaling mechanisms that are disrupted upon aging. It was shown that NTE is widely expressed in the mouse brain, and its activity is essential for lipid homeostasis in the nervous system [44, 45]. NTE deficiency results in the distal degeneration of the longest spinal axons, accompanied by swelling that encompasses accumulated axoplasmic material [28]. Specific deletion of NTE in the neuronal tissue induces neurodegeneration [46]. Despite its known molecular function, the mechanism by which it maintains nervous system integrity during hereditary and toxin-induced neurodegeneration remains unknown. *Drosophila melanogaster* is an excellent genetic model organism to investigate the molecular mechanisms of age-dependent neurodegenerative diseases, and it has been widely used to identify potential drug targets against neurodegenerative diseases [47, 48]. Moreover, the fly nervous system is a great system to shed light on the evolutionarily conserved signaling pathways underlying disease pathology. In Drosophila, more than 70% of genes related to human diseased are conserved [49]. Studying human disease-related genes in Drosophila avoids the ethical issues of biomedical research involving human subjects.

Moreover, Drosophila serves as a well-defined model to study immune reactivity. Flies exhibit a robust immune response to septic injury, involving hemocytes (macrophage-like cells) that efficiently clear pathogens through phagocytosis. This involves the recruitment of immune cells and the activation of immune-related genes. For instance, the signaling cascade of the glial cells missing (gcm) transcription factor, which governs immune cell development and is triggered by aging and acute challenges, is conserved from flies to humans [50]. Additionally, the immune response includes antimicrobial peptides (AMPs) secreted by fat body cells, activated by Toll and immune deficiency (IMD) pathways. The IMD pathway, triggered by Gram-negative bacteria, facilitates macrophage invasion into the inflamed brain, mediated by glia cells [51]. Macrophages in the brain can phagocytose synaptic material, impacting locomotor abilities and longevity, highlighting the delicate balance in evolutionary inflammatory responses [52]. Together, Drosophila satisfies many of the requirements to study human diseases that allows scientists, not only dissection on cellular and molecular levels but also investigation of behavior and neurodegeneration during aging [53-55]. Considering the increasing evidence linking inflammation and neurodegeneration in humans, gaining

insights into the interplay between neuroinflammation and neurodegenerative processes in the Drosophila brain should be beneficial.

In this study, we used a Drosophila NTE/SWS model for human neurodegeneration. Swiss Cheese protein (NTE/SWS) is a highly conserved lysophospholipase that can regulate phosphatidylcholine metabolism [29, 56]. It was also shown that NTE/SWS can act as a regulator of the PKA-C3 catalytic subunit of protein kinase A [57, 58]. Loss of Drosophila NTE/SWS and vertebrate NTE has been shown to result in lipid droplet accumulation, which is involved in neurodegeneration pathogenesis [59-61]. Loss of *sws* leads to age-dependent neurodegeneration (Figure 1B, arrows), CNS vacuolization and abnormal glial morphology accompanied by the formation of multilayered glial structures in the adult Drosophila brain [62, 63]. Recent studies have shown that the pan-glial knockdown of *sws* leads to increased levels of reactive oxygen species (ROS), which in turn induces oxidative stress [64]. However, the role of NTE/SWS in distinct glial types is not clearly understood.

Similar to multiple other organisms, the Drosophila nervous system is composed of neurons and glial cells. Commonly recognized nomenclature identifies six distinct glial cell types based on morphology and function: perineurial and subperineurial glia, cortex glia, astrocyte-like and ensheathing glia, and finally the PNS-specific wrapping glial cells [65, 66]. All organisms with a complex nervous system developed BBB to isolate their neurons from blood [67]. In higher vertebrates, this diffusion barrier is established by polarized endothelial cells that form extensive tight junctions [68], whereas in lower vertebrates and invertebrates the BBB is entirely formed by glial cells, which are additionally sealed by septate junctions (SJs) [67]. The Drosophila BBB includes two glial cell layers: the perineurial glial cells (PG) are primarily involved in nutrient uptake, whereas the main diffusion barrier is made by the subperineurial glia (SPG), which form pleated SJs [69-71]. Glial cells in the Drosophila BBB a crucial role in the immune response as they contribute to the maintenance of the BBB and respond to immune challenges [52, 72-74].

Here we showed that NTE/SWS is present in the surface glia of Drosophila brain that form the BBB and that NTE/SWS is important for the integrity and permeability of the barrier. Importantly, glia-specific expression of Drosophila *NTE/SWS* or human NTE in the *sws* mutant background fully rescues surface glial organization and partially restores BBB integrity, suggesting a conserved function of NTE/SWS. An important observation upon *sws* deficit was the formation of intracellular accumulations within lysosomes, which is a characteristic feature of lysosomal storage disorders. Additionally, NTE/SWS regulates lipid metabolism, distribution of cell junction proteins, and organization of membrane rafts in BBB glia. Moreover, our research revealed that mutants with defective BBB exhibit elevated levels of several innate immunity factors as well as free fatty acids, which are known to play a role in inflammatory pathways. Importantly, the BBB phenotype can be alleviated by the administration of anti-inflammatory agents. These findings emphasize the complex interplay between SWS, BBB function, inflammation, and innate immunity, providing potential avenues for therapeutic interventions in related disorders.

RESULTS

SWS is expressed in the surface glia of Drosophila brain

Our previous data showed that NTE/SWS function is important for both glia and neuronal cells in the brain [61, 64]. After downregulation of NTE/SWS in neurons, adult flies show a decrease in longevity, locomotor and memory deficits, and severe progression of neurodegeneration in the brain [61]. We have shown that NTE/SWS plays a role in the development of the learning center of the brain involved in short-term and long-term memory storage, olfactory control, and startle-induced locomotion [61]. In addition, we found that flies with NTE/SWS deficiency in neurons or glia show mitochondrial abnormalities as well as accumulation of ROS and lipid droplets [61, 64]. Now we have decided to determine the cell type in which NTE/SWS plays a determining role in the maintenance of brain health.

Similar to its human counterpart, NTE, which is found in virtually all tissues, including the nervous system (https://www.proteinatlas.org/ENSG00000032444-PNPLA6/tissue), NTE/SWS is ubiquitously expressed in Drosophila brain, detected by immunohistochemical analysis using SWS-specific antibodies (Figure 2 – figure supplement 1A). NTE/SWS is a transmembrane phospholipase anchored to the cytoplasmic side of the endoplasmic reticulum to regulate lipid membrane homeostasis. Its cytoplasmic localization makes it difficult to determine precisely in which brain cell type it has more pronounced expression, as neurons and glia have very complex shapes and forms. Therefore, additional markers must be used to discriminate NTE/SWS expression in the brain. To address this, we expressed membrane-bound GFP under control of the *sws* promoter (*sws-Gal4; UAS-CD8::GFP*), which allows labeling of membranes of cells in which the *sws* promoter is active. Importantly, *sws* was strongly expressed in the glia that surround the brain and form the blood-brain selective permeability barrier (Figure 1E-F). In Drosophila, the BBB is entirely made by two glial cell layers: perineurial glia and subperineurial glia (PG and SPG, Figure 1C-D). With the help of sophisticated septate junctions, SPG cells form a tight barrier that prevents paracellular diffusion and separates the central nervous system from hemolymph. Since the BBB is protecting the brain from toxic substances, and NTE/SWS deregulation is associated with toxicity-induced neurodegeneration, we investigated whether NTE/SWS has a functional role in BBB maintenance and its selective permeability.

Downregulation of NTE/SWS cell-autonomously affects surface glia integrity

To test if loss of NTE/SWS affects the barrier structure, we analyzed the expression pattern of Coracle (CoraC), which is a major component of SJs [75]. In controls, CoraC is strongly expressed by subperineurial glia cells, shown as a smooth line at the brain surface (Figure 2A, green arrow). Upon *sws* loss, the CoraC pattern at the brain surface was broken and contained lesions and membrane aggregations (Figure 2B, magenta arrow).

Previous characterization of the *sws* loss-of-function mutant showed that NTE/SWS deficiency resulted in the formation of membranous glial structures, especially in the lamina cortex [62]. Since NTE/SWS is ubiquitously expressed, we utilized the double driver line (*repo, nSyb-Gal4,* Figure 2 – figure supplement 1F-F') to achieve its downregulation in both neuronal and glial cells (Figure 2 – figure supplement 1C). Since these animals had the same disorganized structure of brain surface as the loss-of-function mutant, we concluded that NTE/SWS functions specifically in the nervous system to preserve brain surface structure. Moreover, downregulation of *sws* in all glial

cells (*repo>sws*^{RNAi}) resulted in the same phenotype (Figure 2 – figure supplement 2C). At the same time, upon *sws* downregulation in neurons, we did not observe formation of lesions and membrane clusters in the brain surface (Figure 2 – figure supplement 2E), indicating a cell-autonomous function of NTE/SWS in glia to maintain BBB organization.

To test if NTE/SWS has a cell-autonomous role in the brain barrier cells, we used already existing SPG driver lines (*moody-Gal4; UAS-CD8::GFP* and *Gli-Gal4; UAS-CD8::GFP,* Figure 2 – figure supplement 1D-E) and *UAS-sws*^{RNAi}. We found that, similar to pan-glial *sws* knockdown, its downregulation specifically in SPG cells caused the formation of lesions and membrane clusters within the brain surface (Figure 2C, Figure 2 – figure supplement 2D, blue and magenta arrows). Importantly, expression of Drosophila or human NTE in these glia cells rescued this phenotype (Figure 2D and 2H, Figure 2 – figure supplement 2F), demonstrating the conserved function of this protein in SPG cells for brain surface formation and possibly maintenance of the brain barrier.

There have been remarkable recent advancements in the field of protein structure prediction, offering valuable tools for exploring three-dimensional structures with unprecedented effectiveness. We used the AlphaFold2 prediction and the PyMol tools [76] to display predicted structure models of the human NTE and Drosophila NTE/SWS proteins. Both proteins contain a highly conserved patatin-like phospholipase (EST) domain (Figure 2 – figure supplement 3, EST domain in magenta). EST domains in NTE/SWS (952-1118) and human NTE (981-1147) demonstrated a remarkably high level of confidence, exhibiting helical structures with predicted local distance difference test scores (pLDDT) exceeding 90 (Figure 2 – figure supplement 3). The EST domain exhibits a distinctive architectural pattern comprising three layers of α/β/α structure. Its central region is formed by a six-stranded β-sheet, flanked by α-helices in the front and back. Upon comparing the predicted structures of EST-SWS and EST-NTE, we observed a significant overlap between them (Figure 2 – figure supplement 3). These findings offer additional evidence of the high conservation of functional domains in NTE/SWS and the close relationship between these proteins across different species.

Together, the remarkable similarities observed between human and Drosophila SWE/NTE protein structure along with their shared involvement in the formation and maintenance of the brain barrier in Drosophila emphasize their close relationship and suggest a conserved function in BBB maintenance.

Downregulation of NTE/SWS results in multilamellar accumulations

Next, we aimed to understand the nature of the SPG phenotype caused by *sws* deficiency. SPG cells have a very specific shape; they are thin and very large. Fewer than fifty SPG cells surround one adult brain hemisphere and a single SPG cell can cover the size of one half of the imaginal disc of the eye, covering an area equivalent to approximately 10,000 epithelial cells [67, 77, 78]. Therefore, to better visualize the defects in surface glia organization upon *sws* loss, we introduced *moody-Gal4*; *UAS-CD8::GFP* (*moody>CD8::GFP)* constructs into the *sws*^{1} mutant background, which allowed analysis of SPG cell membranes. To our surprise, we observed that almost all lesions that were formed near the brain surface contained membrane material marked by *CD8::GFP* (Figure 2F). This was in sharp contrast to the control, where SPG membranes formed a distinct GFP-positive line (Figure 2E). Importantly, the same excessive SPG cell membranes were observed inside the lesions formed upon *sws* downregulation explicitly in SPG cells (Figure 2G), confirming that NTE/SWS is required cell-autonomously in SPG cells for the proper architecture of the surface glia.

Next, we wanted to understand the origin of these excessive membranes observed in *sws*-deficient glial cells. This task appeared to be quite challenging, as SPG cells form a very thin polarized endothelium, not even reaching 1 μm thickness in most areas [67]. In addition, SPG cells localize in very close proximity to each other and to neurons, making the analysis of subcellular protein localization challenging. Therefore, to dissect in more detail the *sws*-related phenotype of accumulated SPG membranes inside the lesions on the brain surface, we used an electron microscopy approach.

We found that *sws* mutants showed the formation of various multilamellar bodies in the brain, which were not observed in the control (Figure 3A-B'). These atypical structures ranged in size from 5 to 15 μm and contained concentrically laminated and multilayered membranes (yellow arrows), lipid droplets (red arrows) and other partially degraded organelles or cytoplasmic constituents. We hypothesized that these inclusions most likely correspond to secondary lysosomes in the phase of digesting endosomal cargo, which are a hallmark of lysosomal storage disorders (LSDs).

To authenticate the nature of membranous accumulation in *sws* mutants, we used endosomal and lysosomal markers. Rab7 is a small GTPase that belongs to the Rab family and controls transport to late endocytic compartments such as late endosomes and lysosomes [79]. Immunohistochemical analysis demonstrated that in contrast to controls, where Rab7 was present in relatively small and evenly dispersed throughout the brain late endosomes and lysosomes (Figure 3D, red), in *sws*-deficient brains, accumulation of Rab7-positive compartments was observed. Moreover, Rab7-positive structures colocalized with atypical membrane aggregates of SPG cells (Figure 3D', yellow). The same assemblies were observed upon *sws* downregulation in SPG cells (Figure 3D'', yellow).

Rab7 controls biogenesis of lysosomes and clustering and fusion of late endosomes and lysosomes [80]. Therefore, to support the idea that these abnormal cellular accumulations are of lysosomal origin, we used an additional marker – CathepsinL, which is a key lysosomal proteolytic enzyme expressed in most eukaryotic cells [81]. We found that *sws* loss or its downregulation in barrier-forming glia cells resulted in the appearance of CathepsinL-positive inclusions that co-localized with GFP-labeled membrane aggregates formed in the mutant SPG cells (Figure 3E-E'', yellow). We conclude that the structures observed upon NTE/SWS deregulation are abnormally enlarged lysosomes.

Next, we quantified the number of brain hemispheres with atypical Rab7- or CathepsinL-positive accumulations. In the control groups, very few (<10%) of the analyzed brains showed accumulation of Rab7 or CathepsinL. However, in mutants with *sws* loss of function and with *sws* SPG-specific downregulation, a significant increase in the frequency of brains containing Rab7- or CathepsinL -positive aggregates was observed (Figure 3F and 3G). Since *sws*-associated neurodegeneration is age-dependent [61-63, 82, 83], we tested if abnormal lysosomes positive for Rab7 and CathepsinL increase with age. Analysis of the brains of 15-day-old *sws* downregulation in SPG cells demonstrated ~2-fold increase in the percentage of brains with lysosomal accumulations within the brain surface in comparison to 1-day-old animals (Figure 3F and 3G). These data demonstrate for the first time that NTE/SWS –associated phenotypes might be additionally characterized by the excessive storage of cellular material in lysosomes that is accelerated by age.

Importantly, similar abnormal buildup of cellular material in lysosomes have been found in hippocampal neuropil [46] and spinal axons of NTE-deficient mice [28]. While these structures have not been specifically described as lysosomal defects, the presence of similar dense bodies containing concentrically laminated and multilayered membranes

in NTE-deficient mice suggests that, similar to Drosophila, NTE/SWS -related phenotypes in mammals may also be associated with excessive storage of cellular material in lysosomes. Lysosomal changes and dysfunction have been involved in the initiation and development of numerous diseases, such as cancer, autoimmune, cardiovascular, neurodegenerative and LSDs [84, 85]. In particular, LSDs are a group of rare metabolic disorders caused by inherited defects in genes that encode proteins vital for lysosomal homeostasis, such as lysosomal hydrolases or membrane proteins. LSDs often manifest as neurodegenerative disorders. Therefore, next, we wanted to investigate how lysosomal accumulation in SPG cells affects their functions, resulting in progressive brain degeneration.

Downregulation of NTE/SWS affects brain permeability barrier

The main function of SPG cells is to protect the central nervous system from being exposed to molecules that are harmless to peripheral organs but toxic to brain neurons. SPG cells form a thick polarized endothelium, selective permeability of which is achieved by forming very tight SJs that provide structural strength and a barrier that controls the flow of various solutes from outside the brain [67, 77, 78]. Since our data show that the expression pattern of a key SJ protein, CoraC, is dramatically perturbed in *sws*-mutant brains (Figure 2A-B), we decided to test if deregulation of NTE/SWS can affect the ability of SPG cells to form a selective permeability barrier.

As a result of abnormal BBB function, the CNS becomes permeable to small molecules such as dextran-coupled dyes. To test BBB permeability, the 10 kDa dextran dye was injected into the abdomen of flies (Figure 4A). After injection, animals were allowed to recover for at least 12 hours, followed by the dissection and analysis of adult brains. In controls, dextran dye predominantly remained at the outer surface of the brain (Figure 4B-B'). In contrast, the dye was detected inside almost all of the sws^{1} mutant brains (Figure 4C-C'). Moreover, the downregulation of *sws* in different types of glial cells also caused increased permeability of brain barrier in more than 80% of the analyzed brains (Figure 4D). Expression of NTE/SWS and human NTE in glia in sws^{1} mutant rescued the organization of the surface glia (Figure 2H) and partially rescued the barrier phenotype, suggesting that human NTE and Drosophila NTE/SWS are important for the BBB integrity in Drosophila (Figure 4D). Taken together, our results demonstrate that SPG cells with NTE/SWS deficiency are characterized by defective brain barrier function and lysosomal accumulation of excess cellular material, which includes membranes.

Next, we wanted to understand whether the compromised brain barrier in *sws* mutants triggers the activation of any cellular stress pathways, including apoptosis, ferroptosis, oxidative stress, ER stress, and inflammation. We treated mutant flies for 14 days with different anti-inflammatory substances and stress suppressors and analyzed whether observed glial phenotypes could be suppressed by any medication. We analyzed CoraC expression and compared the frequencies of abnormal brain surface appearance in the drug-treated versus untreated animals (Figure 5 – figure supplement 1A-B). We revealed that sodium salicylate, a non-steroidal anti-inflammatory drug (NSAID) and rapamycin, which activates autophagy by inhibiting Tor [86], showed the best ability to suppress surface glia phenotypes in *sws* mutants (Figure 5 – figure supplement 1B-C'). This indicates that an activated inflammatory response is associated with *sws* deficit.

moody$^{\Delta C17}$ *flies with a permeable BBB show glial phenotype similar to sws mutants*

A leaky BBB allows different toxic substances and bacteria to enter the central nervous system and affect neurons and glial cells, which can lead to cell death and increased inflammation in mammals [87]. To test if a permeable brain barrier in general is causing inflammation in Drosophila, we decided to test if an additional mutant with defective BBB has an increased inflammatory response in the brain. We focused on a *moody*$^{\Delta C17}$ mutant that has been previously shown to have a defective brain barrier [88].

Firstly, we tested whether the *moody* mutant shows a phenotype similar to that observed in *sws* mutants by analysis of the CoraC expression pattern. We observed that the surface brain layer in *moody* mutants or upon *moody* downregulation in SPG by *moody-Gal4* (*moody>moody*^{RNAi}) contained lesions and had an abnormal membrane assembly, resembling CoraC expression pattern in *sws* mutants (Figure 5 – figure supplement 2A-C and Figure 2B, magenta arrows).

Secondly, we analyzed if anti-inflammatory factors can reduce glial phenotypes in *moody* mutants, similar to *sws* mutants. We found that in *moody* mutants, the surface glia phenotype analyzed using CoraC as a marker could also be suppressed by NSAID and rapamycin (Figure 5A, Figure 5 – figure supplement 1D-D'). The fact that anti-inflammatory factors can reduce glial phenotypes in both *sws* and *moody* mutants indicates that inflammation, triggered as a result of a compromised brain barrier, plays a role in a feedback loop that exacerbates the abnormal surface glia organization (Figure 5G). At the same time, inflammation inhibitors only partially rescued the BBB phenotype in *moody* and *sws* mutants, suggesting the involvement of additional pathways in maintaining the BBB.

Mutants with defective BBB show upregulation of several innate immunity factors and free fatty acids

Next, we tested whether inflammatory pathways are activated in both mutants with permeable barriers. The molecular mechanisms of innate immunity between flies and mammals are highly evolutionarily conserved. For example, Drosophila Toll and IMD pathways are nuclear factor kappa B (NF-κB)-based signaling pathways that share similarities with the Toll-like receptor and tumor necrosis factor receptor 1 signaling pathways in mammals [50, 73, 89, 90]. It has been previously shown that in glial cells, activation of the IMD pathway results in phosphorylation of the NF-κB transcription factor Relish, which is translocated to the nucleus to induce expression of the AMPs Attacin A, Cecropin A, and Diptericin [52, 73]. We performed qPCR analysis and measured the mRNA levels of these AMPs in heads of *sws* and *moody* loss-of-function mutants. We found that the mRNA levels of all three AMPs were significantly upregulated in mutants in comparison to relevant controls (Figure 5B). These data demonstrate that both mutants with defective BBB exhibit an increased inflammatory response.

In addition, polyunsaturated fatty acids have been shown to play a key role in inflammatory processes. Their oxygenated products, called eicosanoids, induce and regulate inflammation via G-protein coupled receptor (GPCR) signaling pathways [91]. To find out whether levels of polyunsaturated and saturated fatty acids are changed, we measured levels of free fatty acids (FFAs) from accurately weighed heads of control flies and mutants with defective BBB (*sws*^{1} and *moody* $^{\Delta C17}$). FFAs were measured by gas chromatography-mass spectrometry (GC-MS) as described recently [92]. We found that both mutants with defective BBB show upregulated levels of linoleic acid, α- and γ-

linolenic acid, eicosanoic acid, arachidonic acid, and eicosapentaenoic acid (EPA) when compared to controls (Figure 5C). Additionally, levels of other FFAs involved in inflammatory response, 9-cis-tetradecenoic acid, palmitic acid, palmitoleic acid, stearic acid, and oleic acid [93, 94] were elevated upon *sws* or *moody* loss (Figure 5C). These data show that in both mutants with a compromised BBB, the inflammatory response is accompanied by the accumulation of FFAs.

Given that the loss of *sws* results in age-dependent neurodegeneration [62], we investigated whether the increased inflammatory response is progressing with age. We performed qPCR analysis and quantified mRNA levels of AMPs (Attacin A, Cecropin A, and Diptericin) in the heads of *sws* mutants and flies that had *sws* downregulation only in SPG cells (*moody>sws*^{RNAi}) of 15-day-old flies and 30-day-old flies. We confirmed that the mRNA levels of all three AMPs were significantly upregulated in mutants of both ages in comparison to the relevant controls (Figure 5D, black asterisks). Furthermore, we observed a significant age-related increase in the expression of inflammatory genes in both *sws* mutants and flies with *sws* downregulation in SPG cells (*moody>sws*^{RNAi}, Fig. 5D, red asterisks), thereby illustrating the correlation between age-related NTE/SWS neurodegeneration and inflammatory processes. Importantly, expression of Drosophila NTE/SWS in SPG cells in *sws*^{1} mutant background normalized levels of inflammatory genes expression in flies of both ages (15- and 30-day-old flies), confirming that the increased inflammatory response is a consequence of the defective BBB (Figure 5D, green asterisks). Moreover, downregulating *sws* in glial cells during adulthood, after BBB formation, resulted in an increased inflammatory response (Figure 5 – figure supplement 1E). Since previous studies have demonstrated the induction of neurodegeneration by the overactivation of innate immune-response pathways, especially elevated expression of AMPs [89], our data showing increased levels of AMPs in aging flies with a defective BBB further strengthen the connection between the BBB, AMPs, and neuroinflammation and reinforce the causative link between BBB breakdown and inflammaging.

Upon infections and autoimmune conditions, macrophages have the capability to infiltrate the brain, aiding in pathogen removal but also posing the potential risk of causing tissue damage. It has been recently shown that the IMD pathway attracts and facilitates the invasion of hemolymph-borne macrophages across the BBB into the inflamed brain during pupal stages [52]. To investigate whether the neuroinflammatory response in *sws* mutants is associated with the entry of macrophages into the brain, we introduced *srp(Hemo)3xmCherry*, which enables the labeling of macrophages [95], into the *sws*^{1} mutant background. In contrast to control brains, we observed the presence of macrophages within the brain in both developing and adult brains of *sws*^{1}*; srp(Hemo)3xmCherry* mutants (yellow arrowheads, Figure 5 – figure supplement 1F-G). Moreover, using the anti-NimC1 antibody [96], macrophage infiltration into the adult brain was detected in flies with *sws* downregulation specifically in SPG cells (*moody>GFP, sws*^{RNAi}, yellow arrowheads, Figure 5E-F). This suggests that the presence of an inflammatory response in mutants with a compromised BBB is associated with macrophage entry into the brain.

sws and moody mutants have distinct surface glia phenotypes

However, while both *sws* and *moody* mutants have defective BBB, the nature of these mutations and their involvement in cellular processes are very different. Moody is a GPCR that is expressed in SPGs and localizes to the sites of SJ formation [69, 88, 97, 98]. Its cellular function is to control continued cell growth of SPG by differentially regulating actomyosin contractility and SJ organization [98]. NTE/SWS is a

transmembrane ER protein that hydrolyzes phosphatidylcholine and binds to and inhibits the C3 catalytic subunit of protein kinase A [57]. To understand how such different mutations could result in similar outcomes, we first analyzed if *moody* loss would result in lysosomal material accumulation. Electron microscopy analyses demonstrated that unlike in *sws* mutant brains, no intracellular accumulations with extra cellular material were observed upon *moody* loss (compare Figure 3B-B' and Figure 5 – figure supplement 2F). Furthermore, no accumulation of endosomal-lysosomal pathway components such as Rab7 were detected within SPG cells of *moody* mutants (Figure 5 – figure supplement 2G-H). At the same time, as previously described [69, 88, 97, 98], we observed that in the absence of *moody*, SJs were formed, but they were disorganized (Figure 5 – figure supplement 2F, arrow).

We compared in greater detail the SJ organization in both mutants using a molecular component of SJs, Neurexin IV (Nrx-IV). In comparison to the wild type, upon *sws* loss, SJs were not properly assembled and exhibited irregular membrane clusters and disruptions (Figure 6A, C). In contrast, the *moody* mutant exhibited a frayed SJ phenotype (Figure 6B). Since Moody coordinates the continuous organization of junctional strands in an F-actin-dependent manner, as a result of its loss, SJ strands fail to extend properly during cell growth (Figure 6C). While the role of Moody in SJ formation is understood [69, 88, 97, 98], the mechanism by which NTE/SWS may be involved in this process is unclear. The in-depth examination of cell junctional structures in *sws* mutants using electron microscopy revealed their improper assembly, characterized by the accumulation of irregular membrane clusters and disruptions in septa organization (Figure 6E-F, yellow arrowheads). Cell junctions are a special type of plasma membrane domain whose transmembrane proteins form a complex, mechanically stable multiprotein structure [99]. The lipid component of cell junctions exhibits a typical membrane raft structure [100-104].

The main feature of membrane rafts is that they contain an enriched fraction of cholesterol and sphingolipids and are able to dynamically orchestrate specific membrane proteins involved in cell adhesion, signal transduction, protein transport, pathogen entry into the cell, *etc.* Since NTE/SWS regulates lipid membrane homeostasis, we hypothesized that it influences the composition of membrane rafts. Analysis of SPG membranes in *sws*-deficient brains shows abnormal clustering of SJs proteins and disorganized membrane domains, implying that NTE/SWS phospholipase plays a role in organizing SPG membrane architecture (Figure 6C). As lysosomes play a crucial role in lipid catabolism and transport, any disruptions in their function can have repercussions on cellular lipid homeostasis, thereby influencing the composition of membrane rafts. To investigate whether the observed SJ phenotype in *sws* mutants can be replicated by inducing lysosomal dysfunctions, we downregulated in SPG cells several key lysosomal genes: *moody>Dysb*^{RNAi}, *moody>Npc1a*^{RNAi}, *moody>Pldn*^{RNAi}, *and moody>spin*^{RNAi}*.* Significantly, the downregulation of any of these genes led to abnormal formation of SJs and membrane organization in SPG cells (Figure 6 – figure supplement 1A-E). This suggests that the lysosomal control of membrane homeostasis has a significant impact on the appearance of SJs.

In summary, our data show that the phospholipase NTE/SWS plays a crucial role in lysosome biogenesis and organization of the architectural framework of BBB membranes. We propose that since NTE/SWS regulates lipid membrane homeostasis, is loss results in the disruption of membrane rafts, which includes SJs, leading to brain barrier permeability. As a result, the inflammatory response accompanied by the accumulation of free fatty acids is activated in mutant brains, leading to progressive neurodegeneration that can be alleviated by the use of anti-inflammatory drugs.

DISCUSSION

The physiological functions of the BBB, maintaining and protecting the homeostasis of the CNS, are evolutionarily conserved across species [105]. Even though there is already plenty of evidence connecting BBB dysfunction to neurodegenerative diseases, the underlying mechanism is not fully understood. The BBB is formed by microvascular endothelial cells lining the cerebral capillaries penetrating the brain and spinal cord of most mammals and other organisms with a well-developed CNS [106]. Interestingly, NTE is highly expressed not only in the nervous system but also in endothelial cells, suggesting that BBB might be affected upon NTE-associated neurodegenerations (The Human Protein Atlas - https://www.proteinatlas.org/ENSG00000032444-PNPLA6/single+cell+type).

Here we made an intriguing discovery regarding the presence of NTE/SWS in the surface glia responsible for forming the BBB, where it plays a crucial role in ensuring the selective permeability of the BBB and the proper organization of surface glia. Moreover, here we discovered that NTE/SWS -associated neurodegeneration is accompanied by abnormal membrane accumulation within defective lysosomes, indicating importance of NTE/SWS in proper function of lysosomes. It has been demonstrated for some LSDs, for example, Krabbe's disease, to be pathologically characterized by rapidly progressive demyelination of the central nervous system and peripheral nervous system and accumulation of macrophages in the demyelinating lesions [107]. Considering that NTE/SWS is involved in the maturation of non-myelinating Schwann cells during development and de-/remyelination after neuronal injury [36], suggesting that lysosomal function of NTE/SWS might be essential for proper myelination in vertebrates. Interestingly, we found that loss of *sws* or its downregulation in barrier-forming glia led to accumulations of Rab7 and CathepsinL in these cells, demonstrating that NTE/SWS – associated neuropathies might be additionally characterized by excessive storage of cellular material in lysosomes. Importantly, neuroinflammation has been reported in several LSDs. The most abundant lysosomal proteases, Cathepsins have been shown to contribute to neuroinflammation as well as to induce neuronal apoptosis [108].

Over the past few years, there has been a growing appreciation of the organizing principle in cell membranes, especially within the plasma membrane, where such domains are often referred to as "lipid rafts". Such lipid rafts were defined as transient, relatively ordered membrane domains, the formation of which is driven by lipid–lipid and lipid–protein interactions [109]. Previously, it has been demonstrated that NTE/SWS is crucial for membrane lipid homeostasis, and *sws* mutants exhibit increased levels of phosphatidylcholine [104]. Phosphatidylcholine, a key component of most organellar membranes, possesses an amphiphilic nature, enabling it to energetically self-assemble into continuous bilayers [110]. This ability to spontaneously self-organize can explain the appearance of multilayered membrane structures in the lysosomes of *sws* mutants. Furthermore, phosphatidylcholine plays a vital role in generating spontaneous curvature, essential for membrane bending and tubulation in vesicular transport processes within the cell [111]. Therefore, abnormal levels of phosphatidylcholine may impact the lysosome fission and fusion steps, leading to the accumulation of defective lysosomes in *sws* mutants. Since lysosomes are involved in lipid catabolism and transport, disruptions in their function can additionally affect cellular lipid homeostasis [112]. Consequently, alterations in lipid composition due to abnormal NTE/SWS phospholipase function and defective lysosomes in *sws*-mutant cells could affect the constitution of the plasma membrane and its ability to form lipid-driven membrane rafts. Lipid rafts are characterized by the clustering of specific membrane lipids through spontaneous separation of glycolipids, sphingolipids, and cholesterol in a liquid-ordered

phase [113]. Their assembly dynamics depend on the relative availability of different lipids and membrane proteins [103]. Lipid rafts play significant roles in multiple cellular processes, including signaling transduction [109]. Interestingly, tight junctions are considered as raft-like membrane compartments [102], as they represent membrane microdomains crucial for the spatial organization of cell junctions and regulation of paracellular permeability [100, 101]. Therefore, we propose that abnormal organization of tight junctions in the SPG cells of *sws* mutants is caused by abnormal organization of plasma membrane domains.

Lysosomes play an essential role in the breakdown and recycling of intracellular and extracellular material, including lipids, proteins, nucleic acids, and carbohydrates. Any dysfunction of lysosomal system components has catastrophic effects and leads to a variety of fatal diseases [114]. LSDs are often linked to changes in plasma membrane lipid content and lipid raft stoichiometry [115, 116], inflammation [117, 118] and ER stress responses [119, 120]. In the past few years, treatments for LSDs were only able to deal with signs and symptoms of the disorders. One possible approach is to identify an available source for the deficient enzyme using therapeutic methods such as bone marrow transplantation (BMT), enzyme replacement therapy (ERT), substrate reduction therapy (SRT), chemical chaperone therapy (CCT), and gene therapy. At the present time, such strategies are aimed at relieving the severity of symptoms or delaying the disease's progression, yet do not provide a complete cure [121]. However, since we and others [82] have shown that overexpression of human NTE can ameliorate mutant phenotype, it can be speculated that, depending on the causative mutation, ERT might be an option as treatment of NTE/SWS -related disorders.

It has been demonstrated that the ER establishes contacts between its tubules and late endosomes (LEs)/lysosomes, visualized in unpolarized cells as well as in neurons derived from brain tissue. Moreover, disruption of ER tubules causes accumulation of enlarged and less-motile mature lysosomes in the soma, suggesting that ER shape and proper function orchestrate axonal late endosome/lysosome availability in neurons [122, 123]. Considering the ER localization of NTE/SWS in the cell, we propose that abnormal lipid composition in the membrane upon *sws* loss has a significant effect on lysosome structure and functions. Furthermore, ER forms contact sites with plasma membrane through vesicle-associated membrane protein (VAMP)-associated protein VAP [124]. Loss of VAP results in neurodegeneration, such as sporadic amyotrophic lateral sclerosis or Parkinson's disease [125, 126]. Mitochondria-ER contact sites play a crucial role in many vital cellular homoeostatic functions, including mitochondrial quality control, lipid metabolism, calcium homeostasis, unfolded protein response, and ER stress. Disruptions in these functions are commonly observed in neurodegenerative disorders like Parkinson's disease, Alzheimer's disease, and amyotrophic lateral sclerosis [127]. Interestingly, knockdown of *sws* in neurons reduces mitochondria number in the brain and in wing axons [61]. SWS-deficient animals show activation of ER stress response, characterized by elevated levels of GRP78 chaperone and increased splicing of XBP, an ER transcription factor that triggers transcriptional ER stress responses. Neuronal overexpressing XBP1 and treating flies with tauroursodeoxycholic acid (TUDCA), a chemical known to attenuate ER stress-mediated cell death, alleviated locomotor deficits and neurodegeneration in *sws* mutants assayed by vacuolization area [83]. Reduced levels of Sarco/Endoplasmic Reticulum Ca^{2+} ATPase (SERCA) observed in *sws* mutants were linked to disrupted lipid compositions as well. Promoting cytoprotective ER stress pathways may provide therapeutic relief for NTE-related neurodegeneration and motor symptoms [83].

Moreover, we found that BBB disruption is accompanied by elevated levels of free fatty acids, involved in multiple extremely important biological processes. Fatty acids are locally produced in the endothelium and later are transported inside the brain across the BBB [128]. We discovered that Drosophila mutants with leaky BBB showed upregulated levels of such fatty acids as palmitoleic, oleic, linoleic, linolenic, arachidonic, and eicosapentaenoic acids, suggesting abnormal metabolism of unsaturated fatty acids upon barrier dysfunction. In particular, *sws* loss results in increased levels of some saturated free fatty acids (FFAs), including palmitic and stearic acids. FFAs or non-esterified fatty acids, are known to be significant sources of ROS, which lead to the event of oxidative stress [129], resulting in lipotoxicity associated with ER stress, calcium dysregulation, mitochondrial dysfunction, and cell death [130]. Previously it has been demonstrated ROS accumulation and activated ER stress response upon *sws* loss in neurons and glia [61, 64, 83], which might be a result of increased levels of FFAs. In addition, neuronal *sws* knockdown results in the upregulation of antioxidant defense genes [61]. We found that BBB breakdown is accompanied by abnormal fatty acids metabolism, and rapamycin can suppress the abnormal glial phenotype formed in BBB Drosophila mutants. Interestingly, saturated FFAs have been shown to lead to target of rapamycin (mTOR) complex 1 activation and cell apoptosis in podocytes [131]. Moreover, rapamycin significantly diminishes FFA-induced podocyte apoptosis [131], supporting its potential ability to suppress possible outcomes of FFA upregulation in the Drosophila brain, thus improving glial phenotype in mutants with BBB breakdown.

Polyunsaturated fatty acids (PUFAs) are known to be primary precursors of lipid mediators that are abundant immunomodulators [132]. Lipid mediators are signaling molecules, such as eicosanoids, and are implicated in inflammation. More recently, lipid molecules that are pro-inflammatory, and those involved in the resolution of inflammation have become important targets of therapeutic intervention in chronic inflammatory conditions. According to published research, PUFAs metabolism was additionally associated with Alzheimer's disease and dementia [133, 134]. The focus of particular interest has recently been on the PUFAs' involvement in the continued inflammatory response because, in contrast to acute inflammation, chronic inflammatory processes within the central nervous system are crucial for the development of brain pathologies [135, 136]. In our study, we found that brain permeability barrier breakdown is accompanied by abnormal fatty acids metabolism and that an aspirin analogue - a non-steroidal anti-inflammatory drug (NSAID) - showed the best ability to suppress abnormal glial phenotype, indicating that activated inflammatory response possibly plays an important role in maintaining a healthy brain barrier. Thus, feedback signaling loop exists between the condition of the brain permeability barrier, lipid metabolism, and the extent of inflammation.

According to the World Health Organization (WHO), the current decade is considered the Decade of Healthy Aging. As the speed of population aging is accelerating worldwide, the proportion of older people will increase from one in eight people aged 60 years or over in 2017 to one in six by 2030 and one in five by 2050 [137, 138]. Globally, there is a little evidence that older people today are in better health than previous generations (https://www.who.int/home/cms-decommissioning). If people who enter extended age of life are in good health, they will continue to participate and be an integral part of families and communities and will strengthen societies; however, if the added years are dominated by poor health, social isolation or dependency on care, the implications for older people and for society are much more negative. Therefore, aging of the world population has become one of the most important demographic problems/challenges of modern society. Moreover, the global strategy on aging and

health of the older population includes not only treating but also preventing some of the world's leading age-related diseases using biomarkers as indicators of any aspects of health change [139]. Unfortunately, most neurodegenerative diseases in humans currently have no cure, and only palliative care is available. Current research is primarily focused on promoting the development of therapies that can prevent the onset of a number of age-related neurodegenerative diseases. Specific and effective treatments are urgently needed. However, their advance hinges upon a deeper understanding of the molecular mechanisms underlying progressive neurodegeneration. Understanding the molecular mechanisms of inflammaging activated by abnormal fatty acid metabolism and testing new and available drugs in a model organism such as Drosophila may help us to promote the use of anti-inflammatory therapy and dietary supplements for neurodegeneration and get closer to preventing and curing the diseases that lead to malfunctions in the aged brain.

MATERIALS AND METHODS

Drosophila stocks

Fly stocks were maintained at 25°C on a standard cornmeal-agar diet in a controlled environment (constant humidity and light-dark cycle). As controls *OregonR* and w^{1118} lines were used. The sws^{1} mutant and the *UAS-sws* lines were gifts from Doris Kretzschmar [62]. To obtain *sws* transheterozygotes, sws^{1} and sws^{4}, obtained from Bloomington Drosophila Stock Center (BDSC 28121), mutant alleles were used. To express transgenes in a *sws*-dependent manner, a *sws* driver line (*sws-Gal4*), obtained from the Kyoto Stock Center (104592), was used. *y* w* P{GawB}*sws^{NP4072} */ FM7c* line was created using the strategy of the Gal4 enhancer trap element P{GawB} insertion [140, 141]. To define an expression pattern of the driver lines, a *UAS-nlsLacZ, UAS-CD8::GFP* transgenic line, kindly donated by Frank Hirth, was used. To induce human NTE gene expression, a *UAS-hNTE* transgenic line (kindly donated by Robert Wessells) was used. To downregulate *sws* expression, *UAS-*sws^{RNAi} (BDSC 61338) was used. Glia-specific Gal4 driver lines - *repo-Gal4, UAS-CD8::GFP/TM6B*, *Gliotactin-Gal4, UAS-CD8::GFP* and *moody-Gal4, UAS-CD8::GFP* - were gifts from Mikael Simons. A neuronal Gal4 driver, *nSyb-Gal4* was obtained from BDSC (BDSC 51945). In addition, to phenocopy *sws* loss-of-function in the nervous system, a double driver line was generated (*repo-Gal4, nSyb-Gal4, UAS-CD8::GFP/TM6B, Sb),* which allowed the expression of the transgenes in both neuronal and glial cells. To induce *sws* downregulation in glia after the BBB was formed, we used *tub-Gal80*^{ts}*; repo-Gal4/TM6B* driver line. The *moody* $^{\Delta C17}$ mutant was a gift from Christian Klämbt. To downregulate *moody* expression, *UAS-moody*^{RNAi} (BDSC 66326) was used. *UAS-Dysb*^{RNAi} (BDSC 67316), *UAS-Npc1a*^{RNAi} (BDSC 37504), *UAS-Pldn*^{RNAi} (BDSC 67884), *UAS-spin*^{RNAi} (BDSC 27702) lines were used to analyze SJs of lysosomal storage mutants. *srp(Hemo)3xmCherry* line (kindly donated by Angela Giangrande) was used to analyze the macrophage entry through the BBB.

Histology of Drosophila brains

For analysis of adult brain morphology, 7 µm paraffin-embedded sections were cut from fly heads. To prepare Drosophila brain sections, the fly heads were immobilized in collars in the required orientation and fixed in Carnoy fixative solution (6:3:1 = ethanol:chloroform:acetic acid) at 4 °C overnight. Tissue dehydration and embedding in paraffin was performed as described previously [142]. Histological sections were prepared using a Hyrax M25 (Zeiss) microtome and stained with hematoxylin and eosin as described previously [143]. All chemicals for these procedures were obtained from Sigma Aldrich.

Immunohistochemistry

Fly brains of 1-day-old and 15-day-old animals were dissected in 1x Phosphate Buffered Saline (1x PBS) and then fixed in 4% formaldehyde diluted in 1x PBS for 20 minutes at room temperature. Next, brains were washed with PBT (0.2% Triton X-100 in 1x PBS) 4 times, followed by block with PBTB (2 g/l Bovine Serum Albumin, 5% Normal Goat Serum, 0.5 g/l sodium azide) for one hour at room temperature and then incubated at 4°C in with primary antibodies diluted in PBTB on nutator overnight. The following day, samples were washed with 1x PBT four times followed by block for 1h and 2h incubation with secondary antibodies at room temperature. Next, samples were washed 4 times with PBT (one of the washes contained DAPI to mark nuclei). Lastly, medium (70% glycerol, 3% n-propyl gallate in 1x PBS) was added to samples for later mounting on the slides. The following primary antibodies were used: mouse anti-Repo (1:50), mouse anti-CoraC (1:50), and mouse anti-Rab7 (1:50), rat anti-DE-Cadherin (1:50) from the Developmental Studies Hybridoma Bank (DSHB); chicken anti-GFP (#ab13970, 1:1000) and rabbit anti-mCherry (#ab167453, 1:1000) from Abcam; mouse Anti-β-Galactosidase (#Z3781, 1:200) from Promega; rabbit anti-SWS (1:1000 from Doris Kretzschmar); mouse anti-CathepsinL (#1515-CY-010, 1:400) from R&D Systems; rabbit anti-NrxIV (1:1000 from Christian Klämbt); mouse anti-NimC1 (1:300 from István Andó). The following secondary antibodies were used: goat anti-chicken Alexa 488 (1:500), goat anti-rat Alexa 488 (1:500), goat anti-rat Alexa 647 (1:500), goat anti-rabbit Alexa 488 (1:500), and goat anti-rabbit Alex 568 (1:500) from Thermo Fisher Scientific; goat anti-mouse IgG2a Cy3 (1:400), goat anti-mouse IgG1 647, and goat anti-mouse IgG1 Cy3 (1:500) from Jackson ImmunoResearch Laboratory. For visualization of cell nuclei, DAPI dye was used (1:1000, Sigma). Samples were analyzed using a confocal microscope (Zeiss LSM 700). For making figures, Adobe Photoshop software was used.

RNA preparation and real-time quantitative PCR (RT-qPCR)

Total RNA was extracted from 15-day-old and 30-day-old fly brains using Trizol reagent (Invitrogen) following the manufacturer's protocol. To detect *sws* mRNA, the forward and reverse primers AGACATACGCCGTGAATACCG and GCGACGACTGTGTGGACTTG, respectively were used. To detect expression of innate immunity factors, the following forward and reverse primers were used: *Attacin A (*forward and reverse primers CACAACTGGCGGAACTTTGG and AAACATCCTTCACTCCGGGC, respectively*)*, *Cecropin A (*forward and reverse primers AAGCTGGGTGGCTGAAGAAA and TGTTGAGCGATTCCCAGTCC, respectively*),* and *Diptericin (*forward and reverse primers TACCCACTCAATCTTCAGGGAG and TGGTCCACACCTTCTGGTGA, respectively*)*. As an endogenous control for qPCR reactions, Ribosomal Protein L32 (RpL32) with the following forward and reverse primers AAGATGACCATCCGCCCAGC and GTCGATACCCTTGGGCTTGC, respectively, was used. The threshold cycle (CT) was defined as the fractional cycle number at which the fluorescence passes a fixed threshold. The ΔCT value was determined by subtracting the average RpL32 mRNA CT value from the average tested CT value of target mRNA, correspondingly. The ΔΔCT value was calculated by subtracting the ΔCT of the control sample from the ΔCT of the experimental sample. The relative amounts of miRNAs or target mRNA is then determined using the expression $2^{-\Delta\Delta CT}$.

Permeability assay

Flies were injected into the abdomen with a solution containing 10 kDa dextran dye labeled with Texas Red (#D1864) from Molecular Probes. Flies were then allowed to recover for more than 12 hours before the dissection, followed by the analysis for dextran dye presence in the brain. Fly heads of 15-day-old animals were dissected in 1x

Phosphate Buffered Saline (1x PBS) and then fixed in 4% formaldehyde diluted in 1x PBS for 1 hour at room temperature. Then fly brains were dissected in 1x Phosphate Buffered Saline (1x PBS) and fixed in 4% formaldehyde diluted in 1x PBS for 20 minutes at room temperature. Next, brains were washed with PBT (0.2% Triton X-100 in 1x PBS) 4 times, followed by block with PBTB (2 g/l Bovine Serum Albumin, 5% Normal Goat Serum, 0.5 g/l sodium azide) for one hour at room temperature and then washed 2 times with PBT (one of the washes contained DAPI to mark nuclei). Lastly, medium (70% glycerol, 3% n-propyl gallate in 1x PBS) was added to samples for later mounting on the slides.

In vivo Drosophila treatments

TUDCA (#580549), 4-PBA (#567616), Valsartan (#PHR1315), Fenofibrate (#F6020), Sodium Salicylate (#S3007), Rapamycin (#R0395), Deferoxamine mesylate salt (#D9533), Liproxstatin-1 (#SML1414), and Sphingosine (#860025P) from Sigma Aldrich were added to 5% Glucose solution at a final concentration showed by Supplementary file 5. Then, these glucose-dissolved components were fed by micropipettes to the flies that were kept for 14 days on a diet food without any sugar. To visualize the uptake of chemicals, solutions were also colored by 2, 5% w/v of Brilliant Blue (#80717) from Sigma Aldrich.

Extraction and derivatization of free fatty acids from flies

Accurately weighed heads of 15-day-old flies were treated with 1000-µL aliquots of acetonitrile in autosampler glass vials (1.8 mL), the samples were sealed and vortexed several times and then stored in a refrigerator overnight (4°C). Next day, the samples were wormed up to room temperature and centrifuged (10 min, 3345xg, 4°C). Aliquots (950 µL) of the clear supernatants were decanted carefully transferred to autosampler glass vials (1.8 mL). The samples were spiked with 10-µL aliquots of a 1000-µM stock solution of sterculic acid (C19H34O2; 10 nmol; 8-cyclopropen-octadecenoic acid corresponds to C19:1") which served as the internal standard (IS) for all free fatty acids (FFAs). The solvent was evaporated entirely under a stream of nitrogen gas. The solid residues were reconstituted in anhydrous acetonitrile (100 µL). Then, 10 µL Hünig base (*N,N*-diisopropylethylamine) and 10 µL 33 vol% pentafluorobenzyl (PFB) bromide in anhydrous acetonitrile were added. Subsequently, the FFAs were derivatized by heating for 60 min at 30°C to generate the PFB esters of the FFAs. Solvents and reagents were evaporated to dryness under a stream of nitrogen gas. The residues were treated with 1000-µL aliquots of toluene and the derivatives were extracted by vortex-mixing for 120 s. After centrifugation (10 min, 3345xg, 4°C), 300-µL aliquots of the clear and colorless supernatants were transferred into microvials placed in autosampler glass vials (1.8 mL) for GC-MS analysis. A standard control sample containing 1 mL acetonitrile, 1 µL 10 mM arachidonic acid (C20:4, 10 nmol) and 10 µL 1 mM IS (10 nmol) was derivatized as described above for the fly samples after were evaporation to dryness under a stream of nitrogen gas. After centrifugation (10 min, 3345xg, 4°C), 100-µL of the clear and colorless supernatant were transferred into an autosampler glass vial (1.8 mL), diluted with toluene (1:10, v/v) and subjected to GC-MS analysis as described below.

GC-MS analysis of free fatty acids from flies

GC-MS analyses were performed on a GC-MS apparatus consisting of a single quadrupole mass spectrometer model ISQ, a Trace 1210 series gas chromatograph and an AS1310 autosampler from ThermoFisher (Dreieich, Germany). A fused-silica capillary column Optima 17 (15 m length, 0.25 mm I.D., 0.25 µm film thickness) from Macherey-Nagel (Düren, Germany) was used. Aliquots of 1 µL were injected in the splitless mode. Injector temperature was kept at 280°C. Helium was used as the carrier

gas at a constant flow rate of 1.0 mL/min. The oven temperature was held at 40°C for 0.5 min and ramped to 210°C at a rate of 15°C/min, and then to 320°C at a rate of 35°C/min. Interface and ion-source temperatures were set to 300°C and 250°C, respectively. Electron energy was 70 eV and electron current 50 µA. Methane (constant flow rate of 2.4 mL/min) was used as the reactant gas for negative-ion chemical ionization (NICI). The electron multiplier voltage was set to 1300 V. Authentic commercially available reference compounds were used to determine the retention times of the derivatives and to generate their mass spectra. The selected ions [M−PFB]− with mass-to-charge (*m/z*) ratios and retention times of the derivatives are summarized in Supplementary file 6b. Quantitative measurements were performed by selected-ion monitoring (SIM) of the ions listed in Supplementary file 6b with a dwell time of 50 ms and SIM width of 0.5 amu for each ion in three window ranges. The results of the GC-MS analyses of the control standard sample that contained 10 nmol arachidonic acid and 10 nmol internal standard are summarized in Supplementary file 6c. The highest peak area ratio of FFA to the internal standard (FFA/IS) was obtained for arachidonic acid (0.098). This in accordance with the ratio observed in the standard curve (Figure 5 – figure supplement 3A). A lower FFA/IS was obtained for palmitic acid (0.026). As palmitic acid was not externally added to the control standard sample, it is assumed that palmitic fatty acid is ubiquitous present as a contamination in the laboratory materials. An FFA/IS value of 0.027 was obtained for a fatty acid, which co-elutes with nonadecanoic acid (C19:0). As this fatty acid was not externally added to the control standard sample nor it is expected to be a laboratory contamination, it can be hypothesized that it is a contamination in the commercially available preparation of the internal standard which is quasi a C19:0 fatty acid. The FFA/IS values of the other FFAs are remarkably lower (<0.0065), which suggest that they cannot be considered as appreciable contaminations (Figure 5 – figure supplement 3B).

Transmission Electron Microscopy

After dissection, brains of 15-day-old flies were fixed overnight immediately by immersion in 150 mM HEPES containing 1.5% glutaraldehyde and 1.5% formaldehyde at pH 7.35. Preparation for TEM was done as described [144]. Imaging was done in a Zeiss EM 900 at 80 kV, equipped with a side mount CCD camera (TRS).

Quantification and Statistical analysis

To analyze the activation of the inflammatory response, RT-qPCR analysis of AMPs mRNA levels from heads of each genotype was performed. AVE±SEM was calculated. The experiments were performed in at least two biological replicates for each genotype. Two-tailed Student's tests were used to test for statistical significance (*p < 0.05, **p < 0.005, ***p < 0.001, See Supplementary file 1).

To analyze the frequency of brain hemispheres with defective brain surfaces, Z-stack confocal images of the entire adult brain were captured. The brain surface was identified by CoraC expression. The numbers of brain hemispheres exhibiting a normal brain surface, those containing lesions, or those with both lesions and membrane clusters on the brain surface were quantified. For the comparison of observed phenotypes, two-way tables and chi-square tests were used (*p < 0.05, **p < 0.005, ***p < 0.001, See Supplementary file 2).

To assess the frequency of brain hemispheres with the accumulation of Rab7-positive or CathepsinL-positive structures in surface glia, Z-stack confocal images of the entire adult brain were captured. The surface glia were identified by *moody-Gal4, UAS-CD8::GFP* expression. The numbers of brain hemispheres with Rab7 or CathepsinL accumulation in the surface glia were quantified. For the comparison of observed

phenotypes, two-way tables and chi-square tests were used (*p < 0.05, **p < 0.005, ***p < 0.001, See Supplementary file 3).
To analyze the frequency of brain hemispheres with a permeable BBB, Z-stack confocal images of the entire adult brain were captured. The permeable BBB was identified by 10 kDa dextran dye labeled with Texas Red localization inside the fly brain. The numbers of brain hemispheres with a permeable BBB were quantified. All experiments were performed in at least three biological replicates for each genotype. For the comparison of observed phenotypes, two-way tables and chi-square tests were used (*p < 0.05, **p < 0.005, ***p < 0.001, See Supplementary file 4).
To analyze the frequency of brain hemispheres with defective brain surfaces in *in vivo* Drosophila treatment assays, the brain surface was identified by CoraC expression. The numbers of brain hemispheres with formed lesions and membrane clusters on the brain surface were quantified. The reduction in the percentage of the glial phenotype, assayed by CoraC expression pattern in *sws* and *moody* mutants treated with different chemicals compared to untreated mutants, was quantified. All experiments were performed in at least three biological replicates for each genotype. For the comparison of observed phenotypes, two-way tables and chi-square tests were used (*p < 0.05, **p < 0.005, ***p < 0.001, See Supplementary file 5).
To analyze the changes in FFA levels in fly mutant heads, GS-MS measurements of FFAs were performed. One-way Anova tests were used for statistical analysis (*p < 0.05, **p < 0.005, ***p < 0.001, See Supplementary file 6).

ACKNOWLEDGMENTS

We would like to thank Doris Kretzschmar, Mikael Simons, Christian Klämbt, Hugo Bellen, Angela Giangrande, István Andó and Stanislava Chtarbanova-Rudloff for sharing flies and reagents with us. Marko Shcherbatyy for drawing a scheme. Christian Klämbt and Volkan Seyrantepe for contributions to phenotype description. All Shcherbata lab members for critical reading of the manuscript and helpful suggestions. This research was supported by the VolkswagenStiftung (grants 90218 and 97750), the German Research Foundation (DFG) grant numbers 521749003 and INST 192/574-1 FUGG, the Institutional Development Award (IDeA) from the National Institute of General Medical Sciences (NIGMS) of the National Institutes of Health (NIH) under grant numbers P20GM103423 and P20GM104318 and EMBO YIP.

DECLARATION OF INTERESTS

The authors declare no competing interests.

This study includes no data deposited in external repositories.

FIGURE/FIGURE SUPPLEMENT LEGENDS

Figure 1. NTE/SWS is expressed in Drosophila brain and its loss leads to severe neurodegeneration

A-B. Hematoxylin and eosin (H&E)-stained paraffin-embedded brain sections of the 30-day-old control (*Oregon R x white*^{1118}, **A**) and 30-day-old *sws*^{1}/*sws*^{4} transheterozygous flies (**B**). Arrows indicate neurodegeneration at the brain surface. Scale bar: 50 µm.

C-D. Schemes of glia organization in the adult Drosophila brain - Perineurial glia (PG, blue), Subperineurial glia (SPG, light green), Cortex glia (pink), Astrocyte-like glia (turquoise) and Ensheathing glia (yellow).

E-F. Expression pattern of *sws-Gal4* determined by combining of the transcriptional activator Gal4 under control of the *sws* gene promotor (*sws-Gal4*) and the *UAS-CD8::GFP* construct. Fluorescence images of the brain show that *sws* is expressed in all brain cells and strongly expressed in the surface glia (**E** - single section, **F** - Z-stack maximum projection). For NTE/SWS antibody staining pattern see Figure 2 – figure supplement 1A-B. Glia cells are marked with Repo (red), *sws* expression is marked by the membrane *CD8::GFP* (green), and nuclei are marked with DAPI (blue). Scale bar: 50 µm.

Figure 2. Downregulation of NTE/SWS affects surface glia architecture

A-D. Adult brains stained with CoraC (green) and DAPI (magenta). **A**. In controls (*Oregon R x white*^{1118}), CoraC expression is pictured as the smooth line at the surface of the brain (green arrow). In *sws*^{1} mutants (**B**) and in mutants with *sws* downregulation in SPG cells (*moody>sws*^{RNAi}, **C**), the outer glial cell layer labeled by CoraC is irregular and contains either lesions (blue arrow) or lesions and membrane clusters (magenta arrow). Expression of human NTE (*sws*^{1}*; moody>hNTE,* **D**) in SPG cells in mutant background results in the brain surface appearance which is similar to control (green arrow). Scale bar: 50 µm.

E-G. Adult brains stained with CoraC (red), GFP (green) and DAPI (blue) to detect SPG cell membranes marked by co-expression of CoraC and *moody>CD8::GFP* (red+green=yellow). **E.** A smooth line of SPG cell membranes is observed at the surface of control brains (*moody>CD8::GFP*). **F.** In *sws* loss-of-function mutants (*sws*^{1}*; moody>CD8::GFP*), most of the vacuoles formed near the brain surface are filled with the GFP-positive SPG membranes. **G.** Downregulation of *sws* specifically in SPG cells *(moody>sws*^{RNAi}) results in the appearance of the same excessive SPG cell membranes inside the brain lesions. Scale bar: 50 µm.

H. Bar graph shows the percentage of the brain hemispheres with defective brain surface. The percentage of the brain hemispheres with normal brain surface is shown in green, the percentage of the brain hemispheres containing lesions is shown in blue, and the percentage of the brain hemispheres with formed lesions and membrane clusters within the brain surface is shown in purple. Two-way tables and chi-square test were used for statistical analysis. *p < 0.05, **p < 0.005, ***p < 0.001, black asterisks – compared to *Gal4-driver x OR*, red asterisks – compared to *Gal4-driver x UAS-sws*^{RNAi}, number of adult brain hemispheres ≥ 43, at least three biological replicates (see Supplementary file 2).

Figure 2 - figure supplement 1. NTE/SWS expression pattern, *sws* mRNA levels and expression patterns of the Gal4 driver lines used in the study

A-B. Adult brains stained with anti-SWS antibodies (red) and DAPI (blue). **A-A".** Adult brains stained with anti-SWS antibodies (red) and DAPI (blue) show that NTE/SWS is expressed in most if not all brain cells in the control (*Oregon R*). **B-B".** In sws^{1} mutant brains, NTE/SWS expression is dramatically reduced. Scale bar: 50 µm.

C. RT-qPCR analysis of *sws* mRNA levels from flies with glial, neuronal, or glial and neuronal *sws* downregulation (*repo>*sws^{RNAi}, *nSyb>*sws^{RNAi} and *repo, nSyb>*sws^{RNAi}) confirms the efficacy of sws^{RNAi} (red) and *UAS-sws* (blue) constructs. AVE±SEM is indicated. Two-tailed Student's test was used to test for statistical significance, *p < 0.05, **p < 0.005, ***p < 0.001 (see Supplementary file 1).

D-D'. Expression pattern of *moody-Gal4* determined by combining of the transcriptional activator Gal4 under control of the *moody* gene promotor (*moody-Gal4*) and the *UAS-CD8::GFP* and *UAS-nLacZ* constructs. Fluorescence images of the brain show that *moody* is strongly expressed in the surface glia. Glia cells are marked with Repo (red), *moody* expression is indicated by the membrane *CD8::GFP* (green) and nuclear β-Galactosidase (βGal, white), and nuclei are marked with DAPI (blue). Scale bar: 50 µm.

E–E'. Expression pattern of *Gli-Gal4* determined by combining of the transcriptional activator Gal4 under control of the *Gliotactin* gene promotor (*Gli-Gal4*) and the *UAS-CD8::GFP* and *UAS-nLacZ* constructs. Fluorescence images of the brain show that *Gliotactin* is strongly expressed in the surface glia. Glia cells are marked with Repo (red), *Gli* expression is indicated by the membrane CD8::GFP (green) and nuclear β-Galactosidase (βGal, white), and nuclei are marked with DAPI (blue). Scale bar: 50 µm.

F–F'. Expression pattern of the double driver line (*repo, nSyb-Gal4*) determined by combining of the transcriptional activator Gal4 under control of the glial *repo* and neuronal *nSyb* promotors (*repo, nSyb-Gal4*) driving *UAS-CD8::GFP* and *UAS-nLacZ* transgenic constructs. Fluorescence images of the brain show that Repo and nSyb are strongly expressed thought the entire brain. Neuronal cell nuclei are marked by the nuclear β-Galactosidase expression driven by *nSyb-Gal4* (βGal, green), glial cell nuclei are marked by expression of the nuclear β-Galactosidase (βGal, green) driven by *repo-Gal4* and anti-Repo antibodies (red) (red+green=yellow) (**F**). Fluorescence images of the brain show that *repo, nSyb-Gal4* is strongly expressed in glia and neurons marked by the membrane CD8::GFP (green) (**F'**). Scale bar: 50 µm.

Figure 2 - figure supplement 2. *sws* downregulation in neurons does not result in the formation of lesions and membrane clusters within the brain surface, and expression of Drosophila NTE/SWS in glia cells rescued glial phenotype

A-F. Adult brains stained with CoraC (white). In control (*Oregon R x white*^{1118}), CoraC expression is pictured as the smooth line at the surface of the brain (green arrow). In *sws*^{1} mutants (**B**) and in mutants with *sws* downregulation in all glia cells and specifically in SPG cells (*repo>sws*^{RNAi} and *Gli>sws*^{RNAi}, **C** and **D,** respectively), the outer glial cell layer labeled by CoraC is irregular and contains lesions and membrane clusters (magenta arrows). Animals with *sws* downregulation in neurons (*nSyb>sws*^{RNAi}, **E**) do not have lesions and membrane clusters within the brain surface (green arrow). Expression of Drosophila NTE/SWS (*sws*^{1}*; moody>sws,* **F**) in SPG cells in mutant background results in the brain surface appearance which is similar to control (green arrow). Scale bar: 50 μm.

Figure 2 - figure supplement 3. 3D structures of human NTE and Drosophila SWS

The 3D structures of the human NTE and Drosophila NTE/SWS proteins, generated using the AlphaFold2 and PyMOL tools. Both proteins contain a highly conserved patatin-like phospholipase domain known as the EST domain. In the NTE/SWS protein, this domain is located between amino acid residues 952 and 1118, while in the NTE protein, it spans residues 981 to 1147. The EST domain is characterized by a three-layer α/β/α architecture with a central six-stranded β-sheet sandwiched essentially between α-helices front and back. Comparison of the predicted structures of EST-SWS and EST-NTE show that they overlap. The EST domains in both proteins exhibit a high level of confidence as helices, with predicted local distance difference test scores (pLDDT) exceeding 90, indicating high accuracy and reliability in their structural predictions.

Figure 3. Downregulation of NTE/SWS results in intracellular accumulations

A-C. Electron microscopy images of the surface area of the adult brains. **A.** In controls (*white*^{1118}), glia cells that do not contain any abnormal subcellular structures. Scale bar: 1 µm. **B-B'**. *sws*^{1} mutant brains have irregular surface and abnormal accumulation of endomembranous structures (yellow arrows) and lipid droplets (red arrows). Scale bar: 5 µm. **C.** *moody>sws*^{RNAi} fly brain has same abnormal accumulations of endomembranous structures (yellow arrows) as *sws* mutant. Scale bar: 5 µm.

D-D". Adult brains stained with Rab7 (red) to detect lysosomes and late endosomes, GFP (*moody>CD8::GFP,* green) to mark SPG cell membranes and DAPI (blue) to mark nuclei. **D.** A smooth line of SPG cell membranes is observed at the surface of control brains (*moody>CD8::GFP,* green), Rab7 is present in relatively small amounts and evenly dispersed throughout in the brain (red). **D'.** In *sws* loss-of-function mutants (*sws*^{1}*; moody>CD8::GFP*), Rab7-positive structures colocalized with atypical membrane aggregates of GFP-positive SPG membranes (red+green=yellow). **D".** Downregulation of *sws* specifically in SPG cells *(moody> sws*^{RNAi}) results in the appearance of the same assemblies in the SPG cells (yellow). Scale bar: 50 µm.

E-E". Adult brains stained with CathepsinL (red) to detect lysosomes, GFP (*moody>CD8::GFP,* green) to mark SPG cell membranes and DAPI (blue) to mark nuclei. **E.** A smooth line of SPG cell membranes is observed at the surface of control brains (*moody>CD8::GFP,* green), CathepsinL is present in relatively small amounts in the brain (red). **D'.** In *sws* loss-of-function mutants (*sws*^{1}*; moody>CD8::GFP*), CathepsinL-positive structures colocalized with atypical membrane aggregates of GFP-positive SPG membranes (red+green=yellow). **E".** Downregulation of *sws* specifically in SPG cells *(moody> sws*^{RNAi}) results in the appearance of the same assemblies in the SPG cells (yellow). Scale bar: 50 µm.

F. Bar graph shows the percentage of brains with accumulated Rab7 structures at the brain surface. Two-way tables and chi-square test were used for statistical analysis. *p < 0.05, **p < 0.005, ***p < 0.001, black asterisks – compared to *moody-Gal4 x OR*, red asterisks – compared to 1-day-old *moody-Gal4 x UAS-sws*^{RNAi}, number of adult brain hemispheres ≥ 44, at least three biological replicates (see Supplementary file 3).

G. Bar graph shows the percentage of brains with accumulated CathepsinL structures at the brain surface. Two-way tables and chi-square test were used for statistical analysis. *p < 0.05, **p < 0.005, ***p < 0.001, black asterisks – compared to *moody-Gal4 x OR*, red asterisks – compared to 1-day-old *moody-Gal4 x UAS-sws*^{RNAi}, number of adult brain hemispheres ≥ 49, at least three biological replicates (see Supplementary file 3).

Figure 4. Downregulation of NTE/SWS affects brain permeability barrier

A. Scheme of 10 kDa dextran dye permeability assay (see also Materials and Methods for a detailed description of the procedure).

B-C. Localization of dextran dye more than 12 hours after injection in control (*Oregon R*) flies (**B-B'**) and in *sws*^{1} mutant (**C-C'**). Note that dextran dye can be detected in the cells present inside the mutant brain in contrast to control, where dye stays at the outer surface of the brain. Scale bar: 100 µm.

D. Bar graph shows the percentage of the brains with the defective permeability barrier. Two-way tables and chi-square test were used for statistical analysis. *p < 0.05, **p < 0.005, ***p < 0.001, black asterisks – compared to *Gal4-driver x OR*, red asterisks – compared to *Gal4-driver x UAS-sws*^{RNAi}, number of adult brain hemispheres ≥ 44, at least three biological replicates (see Supplementary file 4).

Figure 5. Mutants with defective BBB have an increased age-dependent inflammatory response and elevated levels of FFA

A. Bar graph shows the reduction in the percentage of the glial phenotype, assayed by CoraC expression pattern, in *sws*^{1} (red) and *moody* (olive) mutants that were treated with NSAID and rapamycin in comparison to untreated mutants. This suggests that inflammation accelerates surface glia phenotype. Two-way tables and chi-square test were used for statistical analysis, number of adult brain hemispheres ≥ 104, $p < 0.05$, $^{**}p < 0.005$, $^{***}p < 0.001$, at least three biological replicates (see Supplementary file 5).

B. RT-qPCR analysis of AMPs mRNA levels from relevant controls (green) and *sws*^{1} (red) and *moody* (olive) mutant fly heads shows significantly upregulated expression of inflammatory response genes: *Attacin A, Cecropin A,* and *Diptericin*. AVE±SEM is indicated. Two-tailed Student's test was used to test for statistical significance, $^{*}p < 0.05$, $^{**}p < 0.005$, $^{***}p < 0.001$ (see Supplementary file 1).

C. GS-MS measurements of free fatty acids (FFA) indicate the relative increase of several free fatty acids in the heads of *sws*^{1} (red) and *moody* (olive) mutants compared to relevant controls (*Oregon R* and *white*^{1118,} green). One-way Anova test was used for statistical analysis, $^{*}p < 0.05$, $^{**}p < 0.005$, $^{***}p < 0.001$ (see Supplementary file 6a).

D. RT-qPCR analysis of AMPs mRNA levels from the heads of 15-day-old and 30-day-old relevant controls (green), *sws*^{1} (red), and *moody>sws*^{RNAi} (orange) mutants shows the age-dependent upregulation of the expression of inflammatory response genes (*Attacin A, Cecropin A,* and *Diptericin)*. Moreover, expression of Drosophila NTE/SWS (*sws*^{1}*; moody>sws,* blue) in SPG cells in mutant background normalizes levels of AMPs. The AVE±SEM is shown. Two-tailed Student's test was used to test for statistical significance. $p < 0.05$, $^{**}p < 0.005$, $^{***}p < 0.001$ (see Supplementary file 1). Black asterisks – *sws*^{1} compared to *Oregon R*; *moody>sws*^{RNAi} compared to *moody>/Oregon R* of the same age. Green asterisks – rescue, *sws*^{1}*; moody>sws* compared to *sws*^{1}*.* Red asterisks – ageing, 30-day-old compared to 15-day-old flies.

E-F. Adult brains stained with NimC1 (red), GFP (green) and DAPI (blue) to reveal the macrophage entry in the brain. Note that no macrophages marked by NimC1 (red) are detected in the control brain (*moody>CD8::GFP,* **E**), while NimC1-positive marcrophages are detected in *moody>GFP, sws*^{RNAi} brain (yellow arrowheads, **F**). Scale bar: 20 µm.

G. Mutants with defective brain barrier have upregulated innate immunity factors and exhibit elevated levels of free fatty acids involved in mediating the inflammatory response. Treatment with anti-inflammatory agents alleviates BBB phenotypes, suggesting that a signaling loop that links the condition of the brain barrier permeability, lipid metabolism, and inflammation.

Figure 5 - figure supplement 1. *sws* mutants show increased inflammation and macrophage entry into the brains

A-B. And anti-inflammatory drugs partially suppress glial phenotypes in *sws* mutants. **A.** For the drug feeding assay, vials with sugar-free food with 2 micropipettes filled with dyed drug solution were used. **B**. Bar graph shows the changed percentage of the brains of *sws* mutants with the glial phenotype, assayed with CoraC, which were treated with different stress and inflammation inhibitors in comparison to untreated mutants. Two-way tables and chi-square test were used for statistical analysis. *p < 0.05, **p < 0.005, ***p < 0.001, number of adult brain hemispheres ≥ 73, at least three biological replicates (see Supplementary file 5).

C-C'. Adult brains of *sws* mutants stained with CoraC (white). In sws^{1} mutants treated with control solution (**C**), the outer glial cell layer labeled by CoraC is irregular and contains membrane clusters (red arrowhead). In sws^{1} mutants treated with sodium salicylate (**C'**) the outer glial cell layer contains lesions (red arrowhead) and less membrane clusters. Scale bar: 50 µm. **D-D'.** Adult brains of *moody* mutants stained with CoraC (white). In *moody* mutants treated with control solution (**D**), the outer glial cell layer labeled by CoraC is irregular and contains membrane clusters (olive arrowhead). In *moody* mutants treated with sodium salicylate (**D'**), the outer glial cell layer contains lesions (olive arrowhead) and no membrane clusters.

E. *sws* downregulation in glial cells during adulthood, after the BBB is formed, leads to the increased inflammatory response. RT-qPCR analysis of AMPs mRNA levels from control (*tub-*$Gal80^{ts}$*; repo>/Oregon R*, green) and *tub-*$Gal80^{ts}$*; repo>*sws^{RNAi} (red) fly heads shows upregulated expression of inflammatory response genes: *Attacin A, Cecropin A,* and *Diptericin*. AVE±SEM is indicated (see Supplementary file 1).

F-G. Larval and adult brains stained with mCherry (white) to reveal the macrophage entry in the brain, indicating that control *(Oregon R/srp(Hemo)3xmCherry)* brains (**F**) show almost no macrophages marked by mCherry inside the developing and adult brains. Larval and adult brains of sws^{1}*; srp(Hemo)3xmCherry* mutants (**G**) show macrophages inside the larval and adult brains (yellow arrowheads). Scale bar: 50 µm

Figure 5 - figure supplement 2. *moody* flies with a permeable BBB have similar to *sws* mutants brain surface appearance, but distinct septate junction phenotypes, and *moody*$^{\Delta C17}$ mutant shows no accumulation of endosomal-lysosomal pathway components such as Rab7

A-C. Adult brains stained with CoraC (white) to reveal brain surface. CoraC expression in control brains (*Oregon R x white*^{1118}, **A**) is depicted as the smooth line at the surface of the brain (green arrow). In *moody*$^{\Delta C17}$ mutant brains (**B**) and upon *moody* downregulation in SPG cells (*moody>moody*^{RNAi}, **C**), CoraC-positive outer cell layer contains lesions and membrane clusters (magenta arrows). Scale bar: 20 µm. **D.** Bar graph shows the percentage of the brains with a defective brain surface. Two-way tables and chi-square test were used for statistical analysis, *** $p < 0.001$, number of adult brain hemispheres ≥ 20 (see Supplementary file 2).

E-F. Electron microscopy images of the adult brain surface area in control (*white*^{1118}, **E**) and *moody*$^{\Delta C17}$ mutants (**F**). As previously described [69], the septate junctions in *moody*$^{\Delta C17}$ mutants cannot properly stretch out during cell growth and appear abnormal when compared to controls (black arrows). Scale bar: 1 µm.

G-H. Adult brains stained with Rab7 (red), NrxIV (green) and DAPI (blue) show no abnormal accumulation of Rab7 vesicles in the *Oregon R* control (**G**) and *moody*$^{\Delta C17}$ mutant (**H**) brains.

Figure 5 - figure supplement 3. GC-MS analysis of free fatty acids

A. GC-MS measurement of arachidonic acid (C20:4) with the internal standard (IS). The peak area ratio (PAR) of *m/z* 303 for 20:4 to *m/z* 295 for the IS was linear in the range 0 to 4000 pmol of C20:4 at the fixed amount of 10000 pmol of the IS. The graph shows an example for the quantitative measurement of arachidonic acid (C20:4) with the internal standard (IS). The peak area ratio of m/z 303 for 20:4 to m/z 295 for the IS was linear in the range 0 to 4000 pmol C20:4 at the fixed amount of 10000 pmol of the IS. C20:4 and IS were baseline-separated by chromatography (14.84 min; RSD, 0% vs. 15.14 min; RSD, 0.03%) and entirely by mass spectrometry (m/z 295 vs m/z 303). The IS was found not to contribute to C20:4 by contaminating arachidonic acids or by its 13C isotope. On a molar basis, C20:4 produced about 10 times lower peak areas than the IS in a relevant concentration range of arachidonic acid.

B. Peak area ratios of free fatty acids (FFA) to the internal standard (IS) obtained from GC-MS analysis of a control standard samples that contained 10 nmol arachidonic acid (C20:4) and 10 nmol of the IS. This Figure was constructed with the data of Supplementary file 6c. Each symbol represents a free fatty acid. The horizontal red line at a FFA/IS value of 0.0065 suggests that FFA/IS values higher than 0.0065 can be considered to present in the control standard sample and/or as laboratory contaminations. For more details see the text. t_R, retention time.

Figure 6. Septate junction and membrane domain organization in mutants with defective brain permeability barrier

A-C. Adult brains stained with a septate junction marker NrxIV (white). Scale bar: 50 µm. **A**. In control (*Oregon R*) brain, septate junctions formed by SPG glia are depicted as condensed and distinct strand. The scheme depicts the intact BBB formed by perineurial glia (PG) and subperineurial glia (SPG). The SPG cells establish well-formed septate junctions (SJs) and exhibit organized membrane domains. Furthermore, the lysosomes are fully functional.

B. In *moody*$^{\Delta C17}$ mutants, due to SPG membrane overgrowth, septate junctions are frayed. The scheme illustrates a defective BBB where the proper extension of septate junction strands during cell growth is impaired, resulting in increased permeability. However, despite this issue, the membrane domains remain well-formed, and the lysosomes within the barrier continue to function effectively.

C. In *sws*^{1} mutants, septate junctions and membrane domains are not properly organized. By analyzing SPG membranes in *sws* mutants, abnormal clustering of SJ proteins and disorganized membrane domains are observed. Furthermore, *sws*-deficient brains exhibit excessive storage of cellular material within lysosomes. The scheme shows that SWS-related lipid dysregulation is accompanied by dysfunctional lysosomes, impaired distribution of cell junction proteins, and disrupted organization of membrane domains in surface glia.

D-F. Electron microscopy images of the septate junction area at the surface of the control (*white*^{1118}, **D**) and *sws*^{1} mutant (**E-F**) adult brains. Green arrowheads indicate septate junctions in control and yellow arrowheads indicate septate junctions in *sws*^{1} mutant brains. Scale bar: 250 nm.

Figure 6 - figure supplement 1. Lysosomal mutants show abnormal septate junction formation

A-E. Adult brains stained with CoraC (red), NrxIV (green) and DAPI (blue) to reveal septate junction structures of the surface glia. In control (*moody>/Oregon R,* **A**) brain, septate junctions formed by SPG glia are depicted as condensed and distinct strands. In the lysosomal pathway mutants - *moody>Dysb*^{RNAi} (**B**), *moody>Npc1a*^{RNAi} (**C**), *moody>Pldn*^{RNAi} (**D**), *and moody>spin*^{RNAi} (**E**) flies, septate junctions are not properly organized (yellow arrows). Scale bar: 20 µm.

SUPPLEMENTARY FILE LEGENDS

Supplementary file 1. Relative mRNA levels

[a] - the ΔCT value is determined by subtracting the average CT value of endogenous control gene (Rpl32) from the average mRNA CT value.

[b] - the calculation of ΔΔCT involves subtraction by the ΔCT calibrator value (ΔCT value in control).

[c] - the range is given for relative levels determined by evaluating the expression: $2^{-\Delta\Delta CT}$.

AVE±SEM values are reported from experiments done in at least duplicates. Two-tailed Student's test was used to test for statistical significance.

p^a – compared to the relevant control

p^b – compared to 15-day-old animals of the same genotype

p^c – compared to *sws*^{1} mutant of the same age

Supplementary file 2. NTE/SWS expression in the surface glia is important for the integrity of Drosophila BBB

[a] – compared to control (*OR x w*^{1118})

[b] – compared to *Gal4-driver x OR*

[c] – compared to *Gal4-driver x UAS-sws*^{RNAi}

The values are reported from experiments done in triplicates. For statistical analyses of the observed phenotypes, two-way tables and χ^2-test were used.

Supplementary file 3. NTE/SWS deficit in the surface glia results in the accumulation of Rab7- and CathepsinL-positive structures

[a] – compared to *Gal4-driver x OR* animals of the same age

[b] – compared to 1-day-old animals of the same genotype

The values are reported from experiments done in triplicates. For statistical analyses of the observed phenotypes, two-way tables and χ^2-test were used.

Supplementary file 4. NTE/SWS deficit in the surface glia results in permeable BBB

[a] – compared to control (*OR x w*^{1118})

[b] – compared to *Gal4-driver x OR*

[c] – compared to *Gal4-driver x UAS-sws*^{RNAi}

The values are reported from experiments done in triplicates. For statistical analyses of the observed phenotypes, two-way tables and χ^2-test were used.

Supplementary file 5. The effect of treatment with different anti-inflammatory substances and stress suppressors on the frequency of the surface glia phenotype in *sws* and *moody* mutants

[a] – compared to *sws*^{1} (no drug treatment)

[b] – compared to *moody*$^{\Delta C17}$ (no drug treatment)

The values are reported from experiments done in triplicates. For statistical analyses of the observed phenotypes, two-way tables and χ^2-test were used.

Supplementary file 6a. *sws* and *moody* mutants show upregulated levels of free fatty acids (FFAs)

For statistical analyses one-way ANOVA test was used.

C14:1 - 9-cis-Tetradecenoic acid

C16:0 - Palmitic acid
C16:1 - Palmitoleic acid
C18:0 - Stearic acid
C18:1 - Oleic acid
C18:2 - Linoleic acid
C18:3 - α- and γ-Linolenic acid
C20:0 - Eicosanoic acid
C20:4 - Arachidonic acid
C20:5 - Eicosapentaenoic acid

Supplementary file 6b. *sws* and *moody* mutants show upregulated levels of free fatty acids (FFAs)

Summary of the ions monitored in the SIM mode
SIM#1 (12.00-14.50 min):
m/z 197.4, 199.4, 225.4, 227.4, 253.4, 255.4, 267.4, 269.4
SIM#2 (14.50-15.00 min):
m/z 281.4, 283.4, 279.4, 295.4, 297.4
SIM#3 (15.00-17.00 min):
m/z 301.4, 303.4, 309.4, 311.4, 325.4, 337.4, 339.4, 365.4, 367.4

References

1. Zuo L, Prather ER, Stetskiv M, Garrison DE, Meade JR, Peace TI, et al. Inflammaging and Oxidative Stress in Human Diseases: From Molecular Mechanisms to Novel Treatments. Int J Mol Sci. 2019;20(18). Epub 2019/09/13. doi: 10.3390/ijms20184472. PubMed PMID: 31510091; PubMed Central PMCID: PMCPMC6769561.
2. Liu Z, Ren Z, Zhang J, Chuang CC, Kandaswamy E, Zhou T, et al. Role of ROS and Nutritional Antioxidants in Human Diseases. Front Physiol. 2018;9:477. Epub 2018/06/06. doi: 10.3389/fphys.2018.00477. PubMed PMID: 29867535; PubMed Central PMCID: PMCPMC5966868.
3. Rojas-Gutierrez E, Munoz-Arenas G, Trevino S, Espinosa B, Chavez R, Rojas K, et al. Alzheimer's disease and metabolic syndrome: A link from oxidative stress and inflammation to neurodegeneration. Synapse. 2017;71(10):e21990. Epub 2017/06/27. doi: 10.1002/syn.21990. PubMed PMID: 28650104.
4. Liu Z, Zhou T, Ziegler AC, Dimitrion P, Zuo L. Oxidative Stress in Neurodegenerative Diseases: From Molecular Mechanisms to Clinical Applications. Oxid Med Cell Longev. 2017;2017:2525967. Epub 2017/08/09. doi: 10.1155/2017/2525967. PubMed PMID: 28785371; PubMed Central PMCID: PMCPMC5529664.
5. Zhang W, Xiao D, Mao Q, Xia H. Role of neuroinflammation in neurodegeneration development. Signal Transduct Target Ther. 2023;8(1):267. Epub 2023/07/12. doi: 10.1038/s41392-023-01486-5. PubMed PMID: 37433768; PubMed Central PMCID: PMCPMC10336149.
6. Chitnis T, Weiner HL. CNS inflammation and neurodegeneration. J Clin Invest. 2017;127(10):3577-87. Epub 2017/09/06. doi: 10.1172/JCI90609. PubMed PMID: 28872464; PubMed Central PMCID: PMCPMC5617655.
7. Franceschi C, Garagnani P, Parini P, Giuliani C, Santoro A. Inflammaging: a new immune-metabolic viewpoint for age-related diseases. Nat Rev Endocrinol. 2018;14(10):576-90. Epub 2018/07/27. doi: 10.1038/s41574-018-0059-4. PubMed PMID: 30046148.
8. McGeer PL, McGeer EG. Inflammation and the degenerative diseases of aging. Ann N Y Acad Sci. 2004;1035:104-16. Epub 2005/02/01. doi: 10.1196/annals.1332.007. PubMed PMID: 15681803.
9. Li X, Li C, Zhang W, Wang Y, Qian P, Huang H. Inflammation and aging: signaling pathways and intervention therapies. Signal Transduct Target Ther. 2023;8(1):239. Epub 2023/06/09. doi: 10.1038/s41392-023-01502-8. PubMed PMID: 37291105; PubMed Central PMCID: PMCPMC10248351.
10. Takata F, Nakagawa S, Matsumoto J, Dohgu S. Blood-Brain Barrier Dysfunction Amplifies the Development of Neuroinflammation: Understanding of Cellular Events in Brain Microvascular Endothelial Cells for Prevention and Treatment of BBB Dysfunction. Front Cell Neurosci. 2021;15:661838. Epub 2021/10/01. doi: 10.3389/fncel.2021.661838. PubMed PMID: 34588955; PubMed Central PMCID: PMCPMC8475767.
11. Sweeney MD, Sagare AP, Zlokovic BV. Blood-brain barrier breakdown in Alzheimer disease and other neurodegenerative disorders. Nat Rev Neurol. 2018;14(3):133-50. Epub 2018/01/30. doi: 10.1038/nrneurol.2017.188. PubMed PMID: 29377008; PubMed Central PMCID: PMCPMC5829048.
12. Spencer JI, Bell JS, DeLuca GC. Vascular pathology in multiple sclerosis: reframing pathogenesis around the blood-brain barrier. J Neurol Neurosurg Psychiatry. 2018;89(1):42-52. Epub 2017/09/02. doi: 10.1136/jnnp-2017-316011. PubMed PMID: 28860328.
13. Munji RN, Soung AL, Weiner GA, Sohet F, Semple BD, Trivedi A, et al. Profiling the mouse brain endothelial transcriptome in health and disease models reveals a core blood-brain barrier dysfunction module. Nature neuroscience. 2019;22(11):1892-902. Epub 2019/10/16. doi: 10.1038/s41593-019-0497-x. PubMed PMID: 31611708; PubMed Central PMCID: PMCPMC6858546.
14. Blyth BJ, Farhavar A, Gee C, Hawthorn B, He H, Nayak A, et al. Validation of serum markers for blood-brain barrier disruption in traumatic brain injury. J Neurotrauma. 2009;26(9):1497-507. Epub 2009/03/05. doi: 10.1089/neu.2008.0738. PubMed PMID: 19257803; PubMed Central PMCID: PMCPMC2822805.
15. Gray MT, Woulfe JM. Striatal blood-brain barrier permeability in Parkinson's disease. J Cereb Blood Flow Metab. 2015;35(5):747-50. Epub 2015/03/12. doi: 10.1038/jcbfm.2015.32. PubMed PMID: 25757748; PubMed Central PMCID: PMCPMC4420870.

16. Zhou YT, Xu YN, Ren XY, Zhang XF. Inactivation of microglia dampens blood-brain barrier permeability and loss of dopaminergic neurons in paraquat-lesioned mice. Food Chem Toxicol. 2023;174:113692. Epub 2023/02/27. doi: 10.1016/j.fct.2023.113692. PubMed PMID: 36842752.
17. Whitson HE, Colton C, El Khoury J, Gate D, Goate A, Heneka MT, et al. Infection and inflammation: New perspectives on Alzheimer's disease. Brain Behav Immun Health. 2022;22:100462. Epub 2022/09/20. doi: 10.1016/j.bbih.2022.100462. PubMed PMID: 36118272; PubMed Central PMCID: PMCPMC9475126.
18. Segarra M, Aburto MR, Acker-Palmer A. Blood-Brain Barrier Dynamics to Maintain Brain Homeostasis. Trends Neurosci. 2021;44(5):393-405. Epub 2021/01/12. doi: 10.1016/j.tins.2020.12.002. PubMed PMID: 33423792.
19. Issa AR, Sun J, Petitgas C, Mesquita A, Dulac A, Robin M, et al. The lysosomal membrane protein LAMP2A promotes autophagic flux and prevents SNCA-induced Parkinson disease-like symptoms in the Drosophila brain. Autophagy. 2018;14(11):1898-910. Epub 2018/07/11. doi: 10.1080/15548627.2018.1491489. PubMed PMID: 29989488; PubMed Central PMCID: PMCPMC6152503.
20. Peng W, Minakaki G, Nguyen M, Krainc D. Preserving Lysosomal Function in the Aging Brain: Insights from Neurodegeneration. Neurotherapeutics. 2019;16(3):611-34. Epub 2019/06/12. doi: 10.1007/s13311-019-00742-3. PubMed PMID: 31183763; PubMed Central PMCID: PMCPMC6694346.
21. Aman Y, Schmauck-Medina T, Hansen M, Morimoto RI, Simon AK, Bjedov I, et al. Autophagy in healthy aging and disease. Nat Aging. 2021;1(8):634-50. Epub 2021/12/14. doi: 10.1038/s43587-021-00098-4. PubMed PMID: 34901876; PubMed Central PMCID: PMCPMC8659158.
22. Calder PC. n-3 PUFA and inflammation: from membrane to nucleus and from bench to bedside. Proc Nutr Soc. 2020:1-13. Epub 2020/07/07. doi: 10.1017/S0029665120007077. PubMed PMID: 32624016.
23. Chew H, Solomon VA, Fonteh AN. Involvement of Lipids in Alzheimer's Disease Pathology and Potential Therapies. Front Physiol. 2020;11:598. Epub 2020/06/26. doi: 10.3389/fphys.2020.00598. PubMed PMID: 32581851; PubMed Central PMCID: PMCPMC7296164.
24. Emre C, Do KV, Jun B, Hjorth E, Alcalde SG, Kautzmann MI, et al. Age-related changes in brain phospholipids and bioactive lipids in the APP knock-in mouse model of Alzheimer's disease. Acta Neuropathol Commun. 2021;9(1):116. Epub 2021/07/01. doi: 10.1186/s40478-021-01216-4. PubMed PMID: 34187579; PubMed Central PMCID: PMCPMC8244172.
25. Dumas JA, Bunn JY, LaMantia MA, McIsaac C, Senft Miller A, Nop O, et al. Alteration of brain function and systemic inflammatory tone in older adults by decreasing the dietary palmitic acid intake. Aging Brain. 2023;3:100072. Epub 2023/07/06. doi: 10.1016/j.nbas.2023.100072. PubMed PMID: 37408793; PubMed Central PMCID: PMCPMC10318304.
26. Freitas HR, Ferreira GDC, Trevenzoli IH, Oliveira KJ, de Melo Reis RA. Fatty Acids, Antioxidants and Physical Activity in Brain Aging. Nutrients. 2017;9(11). Epub 2017/11/22. doi: 10.3390/nu9111263. PubMed PMID: 29156608; PubMed Central PMCID: PMCPMC5707735.
27. Glynn P. Neuropathy target esterase and phospholipid deacylation. Biochim Biophys Acta. 2005;1736(2):87-93. doi: 10.1016/j.bbalip.2005.08.002. PubMed PMID: 16137924.
28. Read DJ, Li Y, Chao MV, Cavanagh JB, Glynn P. Neuropathy target esterase is required for adult vertebrate axon maintenance. J Neurosci. 2009;29(37):11594-600. Epub 2009/09/18. doi: 10.1523/JNEUROSCI.3007-09.2009. PubMed PMID: 19759306; PubMed Central PMCID: PMCPMC3849655.
29. Lush MJ, Li Y, Read DJ, Willis AC, Glynn P. Neuropathy target esterase and a homologous Drosophila neurodegeneration-associated mutant protein contain a novel domain conserved from bacteria to man. Biochem J. 1998;332 (Pt 1):1-4. Epub 1998/05/13. doi: 10.1042/bj3320001. PubMed PMID: 9576844; PubMed Central PMCID: PMCPMC1219444.
30. Richardson RJ, Hein ND, Wijeyesakere SJ, Fink JK, Makhaeva GF. Neuropathy target esterase (NTE): overview and future. Chemico-biological interactions. 2013;203(1):238-44. Epub 2012/12/12. doi: 10.1016/j.cbi.2012.10.024. PubMed PMID: 23220002.

31. Richardson RJ, Fink JK, Glynn P, Hufnagel RB, Makhaeva GF, Wijeyesakere SJ. Neuropathy target esterase (NTE/PNPLA6) and organophosphorus compound-induced delayed neurotoxicity (OPIDN). Adv Neurotoxicol. 2020;4:1-78. Epub 2020/06/11. doi: 10.1016/bs.ant.2020.01.001. PubMed PMID: 32518884; PubMed Central PMCID: PMCPMC7271139.
32. Deik A, Johannes B, Rucker JC, Sanchez E, Brodie SE, Deegan E, et al. Compound heterozygous PNPLA6 mutations cause Boucher-Neuhauser syndrome with late-onset ataxia. J Neurol. 2014;261(12):2411-23. doi: 10.1007/s00415-014-7516-3. PubMed PMID: 25267340; PubMed Central PMCID: PMCPMC4245359.
33. Synofzik M, Gonzalez MA, Lourenco CM, Coutelier M, Haack TB, Rebelo A, et al. PNPLA6 mutations cause Boucher-Neuhauser and Gordon Holmes syndromes as part of a broad neurodegenerative spectrum. Brain. 2014;137(Pt 1):69-77. Epub 2013/12/21. doi: 10.1093/brain/awt326. PubMed PMID: 24355708; PubMed Central PMCID: PMCPMC3891450.
34. Synofzik M, Kernstock C, Haack TB, Schols L. Ataxia meets chorioretinal dystrophy and hypogonadism: Boucher-Neuhauser syndrome due to PNPLA6 mutations. J Neurol Neurosurg Psychiatry. 2015;86(5):580-1. doi: 10.1136/jnnp-2014-307793. PubMed PMID: 24790214.
35. Topaloglu AK, Lomniczi A, Kretzschmar D, Dissen GA, Kotan LD, McArdle CA, et al. Loss-of-function mutations in PNPLA6 encoding neuropathy target esterase underlie pubertal failure and neurological deficits in Gordon Holmes syndrome. J Clin Endocrinol Metab. 2014;99(10):E2067-75. Epub 2014/07/18. doi: 10.1210/jc.2014-1836. PubMed PMID: 25033069; PubMed Central PMCID: PMCPMC5393493.
36. McFerrin J, Patton BL, Sunderhaus ER, Kretzschmar D. NTE/PNPLA6 is expressed in mature Schwann cells and is required for glial ensheathment of Remak fibers. Glia. 2017;65(5):804-16. Epub 2017/02/17. doi: 10.1002/glia.23127. PubMed PMID: 28206686; PubMed Central PMCID: PMCPMC5357176.
37. Rainier S, Bui M, Mark E, Thomas D, Tokarz D, Ming L, et al. Neuropathy target esterase gene mutations cause motor neuron disease. Am J Hum Genet. 2008;82(3):780-5. doi: 10.1016/j.ajhg.2007.12.018. PubMed PMID: 18313024; PubMed Central PMCID: PMCPMC2427280.
38. Fereshtehnejad SM, Saleh PA, Oliveira LM, Patel N, Bhowmick S, Saranza G, et al. Movement disorders in hereditary spastic paraplegia (HSP): a systematic review and individual participant data meta-analysis. Neurol Sci. 2023;44(3):947-59. Epub 2022/11/29. doi: 10.1007/s10072-022-06516-8. PubMed PMID: 36441344; PubMed Central PMCID: PMCPMC9925593.
39. Allison R, Edgar JR, Pearson G, Rizo T, Newton T, Gunther S, et al. Defects in ER-endosome contacts impact lysosome function in hereditary spastic paraplegia. J Cell Biol. 2017;216(5):1337-55. Epub 2017/04/09. doi: 10.1083/jcb.201609033. PubMed PMID: 28389476; PubMed Central PMCID: PMCPMC5412567.
40. Lim Y, Cho IT, Schoel LJ, Cho G, Golden JA. Hereditary spastic paraplegia-linked REEP1 modulates endoplasmic reticulum/mitochondria contacts. Ann Neurol. 2015;78(5):679-96. Epub 2015/07/24. doi: 10.1002/ana.24488. PubMed PMID: 26201691; PubMed Central PMCID: PMCPMC4681538.
41. Namekawa M, Muriel MP, Janer A, Latouche M, Dauphin A, Debeir T, et al. Mutations in the SPG3A gene encoding the GTPase atlastin interfere with vesicle trafficking in the ER/Golgi interface and Golgi morphogenesis. Mol Cell Neurosci. 2007;35(1):1-13. Epub 2007/02/27. doi: 10.1016/j.mcn.2007.01.012. PubMed PMID: 17321752.
42. Renvoise B, Chang J, Singh R, Yonekawa S, FitzGibbon EJ, Mankodi A, et al. Lysosomal abnormalities in hereditary spastic paraplegia types SPG15 and SPG11. Ann Clin Transl Neurol. 2014;1(6):379-89. Epub 2014/07/08. doi: 10.1002/acn3.64. PubMed PMID: 24999486; PubMed Central PMCID: PMCPMC4078876.
43. Chang J, Lee S, Blackstone C. Spastic paraplegia proteins spastizin and spatacsin mediate autophagic lysosome reformation. J Clin Invest. 2014;124(12):5249-62. Epub 2014/11/05. doi: 10.1172/JCI77598. PubMed PMID: 25365221; PubMed Central PMCID: PMCPMC4348974.
44. Glynn P, Holton JL, Nolan CC, Read DJ, Brown L, Hubbard A, et al. Neuropathy target esterase: immunolocalization to neuronal cell bodies and axons. Neuroscience. 1998;83(1):295-302. PubMed PMID: 9466418.

45. Moser M, Stempfl T, Li Y, Glynn P, Buttner R, Kretzschmar D. Cloning and expression of the murine sws/NTE gene. Mech Dev. 2000;90(2):279-82. Epub 2000/01/21. doi: 10.1016/s0925-4773(99)00239-7. PubMed PMID: 10640712.
46. Akassoglou K, Malester B, Xu J, Tessarollo L, Rosenbluth J, Chao MV. Brain-specific deletion of neuropathy target esterase/swisscheese results in neurodegeneration. Proc Natl Acad Sci U S A. 2004;101(14):5075-80. Epub 2004/03/31. doi: 10.1073/pnas.0401030101. PubMed PMID: 15051870; PubMed Central PMCID: PMCPMC387376.
47. Ma M, Moulton MJ, Lu S, Bellen HJ. 'Fly-ing' from rare to common neurodegenerative disease mechanisms. Trends Genet. 2022;38(9):972-84. Epub 2022/04/29. doi: 10.1016/j.tig.2022.03.018. PubMed PMID: 35484057; PubMed Central PMCID: PMCPMC9378361.
48. Kretzschmar D. PNPLA6/NTE, an Evolutionary Conserved Phospholipase Linked to a Group of Complex Human Diseases. Metabolites. 2022;12(4). Epub 2022/04/22. doi: 10.3390/metabo12040284. PubMed PMID: 35448471; PubMed Central PMCID: PMCPMC9025805.
49. Ugur B, Chen K, Bellen HJ. Drosophila tools and assays for the study of human diseases. Dis Model Mech. 2016;9(3):235-44. Epub 2016/03/05. doi: 10.1242/dmm.023762. PubMed PMID: 26935102; PubMed Central PMCID: PMCPMC4833332.
50. Pavlidaki A, Panic R, Monticelli S, Riet C, Yuasa Y, Cattenoz PB, et al. An anti-inflammatory transcriptional cascade conserved from flies to humans. Cell Rep. 2022;41(3):111506. Epub 2022/10/20. doi: 10.1016/j.celrep.2022.111506. PubMed PMID: 36261018.
51. De Gregorio E, Spellman PT, Tzou P, Rubin GM, Lemaitre B. The Toll and Imd pathways are the major regulators of the immune response in Drosophila. EMBO J. 2002;21(11):2568-79. Epub 2002/05/29. doi: 10.1093/emboj/21.11.2568. PubMed PMID: 12032070; PubMed Central PMCID: PMCPMC126042.
52. Winkler B, Funke D, Benmimoun B, Speder P, Rey S, Logan MA, et al. Brain inflammation triggers macrophage invasion across the blood-brain barrier in Drosophila during pupal stages. Sci Adv. 2021;7(44):eabh0050. Epub 2021/10/28. doi: 10.1126/sciadv.abh0050. PubMed PMID: 34705495; PubMed Central PMCID: PMCPMC8550232.
53. Carney TD, Hebalkar RY, Edeleva E, Cicek IO, Shcherbata HR. Signaling through the dystrophin glycoprotein complex affects the stress-dependent transcriptome in Drosophila. Dis Model Mech. 2023;16(1). Epub 2023/01/04. doi: 10.1242/dmm.049862. PubMed PMID: 36594281; PubMed Central PMCID: PMCPMC9922874.
54. Yatsenko AS, Shcherbata HR. Distant activation of Notch signaling induces stem cell niche assembly. PLoS genetics. 2021;17(3):e1009489. Epub 2021/03/30. doi: 10.1371/journal.pgen.1009489. PubMed PMID: 33780456; PubMed Central PMCID: PMCPMC8031783.
55. Yatsenko AS, Kucherenko MM, Xie Y, Urlaub H, Shcherbata HR. Exocyst-mediated membrane trafficking of the lissencephaly-associated ECM receptor dystroglycan is required for proper brain compartmentalization. Elife. 2021;10. Epub 2021/02/24. doi: 10.7554/eLife.63868. PubMed PMID: 33620318; PubMed Central PMCID: PMCPMC7929561.
56. Zaccheo O, Dinsdale D, Meacock PA, Glynn P. Neuropathy target esterase and its yeast homologue degrade phosphatidylcholine to glycerophosphocholine in living cells. J Biol Chem. 2004;279(23):24024-33. doi: 10.1074/jbc.M400830200. PubMed PMID: 15044461.
57. Bettencourt da Cruz A, Wentzell J, Kretzschmar D. Swiss Cheese, a protein involved in progressive neurodegeneration, acts as a noncanonical regulatory subunit for PKA-C3. J Neurosci. 2008;28(43):10885-92. Epub 2008/10/24. doi: 10.1523/JNEUROSCI.3015-08.2008. PubMed PMID: 18945896; PubMed Central PMCID: PMCPMC2723165.
58. Wentzell JS, Cassar M, Kretzschmar D. Organophosphate-induced changes in the PKA regulatory function of Swiss Cheese/NTE lead to behavioral deficits and neurodegeneration. PloS one. 2014;9(2):e87526. Epub 2014/02/22. doi: 10.1371/journal.pone.0087526. PubMed PMID: 24558370; PubMed Central PMCID: PMCPMC3928115.
59. Chang P, He L, Wang Y, Heier C, Wu Y, Huang F. Characterization of the Interaction of Neuropathy Target Esterase with the Endoplasmic Reticulum and Lipid Droplets. Biomolecules.

2019;9(12). Epub 2019/12/15. doi: 10.3390/biom9120848. PubMed PMID: 31835418; PubMed Central PMCID: PMCPMC6995513.
60. Farmer BC, Walsh AE, Kluemper JC, Johnson LA. Lipid Droplets in Neurodegenerative Disorders. Front Neurosci. 2020;14:742. Epub 2020/08/28. doi: 10.3389/fnins.2020.00742. PubMed PMID: 32848541; PubMed Central PMCID: PMCPMC7403481.
61. Melentev PA, Ryabova EV, Surina NV, Zhmujdina DR, Komissarov AE, Ivanova EA, et al. Loss of swiss cheese in Neurons Contributes to Neurodegeneration with Mitochondria Abnormalities, Reactive Oxygen Species Acceleration and Accumulation of Lipid Droplets in Drosophila Brain. Int J Mol Sci. 2021;22(15). Epub 2021/08/08. doi: 10.3390/ijms22158275. PubMed PMID: 34361042; PubMed Central PMCID: PMCPMC8347196.
62. Kretzschmar D, Hasan G, Sharma S, Heisenberg M, Benzer S. The swiss cheese mutant causes glial hyperwrapping and brain degeneration in Drosophila. J Neurosci. 1997;17(19):7425-32. Epub 1997/09/20. PubMed PMID: 9295388.
63. Dutta S, Rieche F, Eckl N, Duch C, Kretzschmar D. Glial expression of Swiss cheese (SWS), the Drosophila orthologue of neuropathy target esterase (NTE), is required for neuronal ensheathment and function. Dis Model Mech. 2016;9(3):283-94. Epub 2015/12/05. doi: 10.1242/dmm.022236. PubMed PMID: 26634819; PubMed Central PMCID: PMCPMC4826977.
64. Ryabova EV, Melentev PA, Komissarov AE, Surina NV, Ivanova EA, Matiytsiv N, et al. Morpho-Functional Consequences of Swiss Cheese Knockdown in Glia of Drosophila melanogaster. Cells. 2021;10(3). Epub 2021/04/04. doi: 10.3390/cells10030529. PubMed PMID: 33801404; PubMed Central PMCID: PMCPMC7998100.
65. Yildirim K, Petri J, Kottmeier R, Klambt C. Drosophila glia: Few cell types and many conserved functions. Glia. 2019;67(1):5-26. Epub 2018/11/18. doi: 10.1002/glia.23459. PubMed PMID: 30443934.
66. Trebuchet G, Cattenoz PB, Zsamboki J, Mazaud D, Siekhaus DE, Fanto M, et al. The Repo Homeodomain Transcription Factor Suppresses Hematopoiesis in Drosophila and Preserves the Glial Fate. J Neurosci. 2019;39(2):238-55. Epub 2018/12/07. doi: 10.1523/JNEUROSCI.1059-18.2018. PubMed PMID: 30504274; PubMed Central PMCID: PMCPMC6360283.
67. Limmer S, Weiler A, Volkenhoff A, Babatz F, Klambt C. The Drosophila blood-brain barrier: development and function of a glial endothelium. Front Neurosci. 2014;8:365. Epub 2014/12/03. doi: 10.3389/fnins.2014.00365. PubMed PMID: 25452710; PubMed Central PMCID: PMCPMC4231875.
68. Armulik A, Genove G, Mae M, Nisancioglu MH, Wallgard E, Niaudet C, et al. Pericytes regulate the blood-brain barrier. Nature. 2010;468(7323):557-61. Epub 2010/10/15. doi: 10.1038/nature09522. PubMed PMID: 20944627.
69. Babatz F, Naffin E, Klambt C. The Drosophila Blood-Brain Barrier Adapts to Cell Growth by Unfolding of Pre-existing Septate Junctions. Dev Cell. 2018;47(6):697-710 e3. Epub 2018/11/30. doi: 10.1016/j.devcel.2018.10.002. PubMed PMID: 30482667.
70. Schwabe T, Li X, Gaul U. Dynamic analysis of the mesenchymal-epithelial transition of blood-brain barrier forming glia in Drosophila. Biol Open. 2017;6(2):232-43. Epub 2017/01/22. doi: 10.1242/bio.020669. PubMed PMID: 28108476; PubMed Central PMCID: PMCPMC5312092.
71. Kremer MC, Jung C, Batelli S, Rubin GM, Gaul U. The glia of the adult Drosophila nervous system. Glia. 2017;65(4):606-38. Epub 2017/01/31. doi: 10.1002/glia.23115. PubMed PMID: 28133822; PubMed Central PMCID: PMCPMC5324652.
72. van Alphen B, Stewart S, Iwanaszko M, Xu F, Li K, Rozenfeld S, et al. Glial immune-related pathways mediate effects of closed head traumatic brain injury on behavior and lethality in Drosophila. PLoS Biol. 2022;20(1):e3001456. Epub 2022/01/27. doi: 10.1371/journal.pbio.3001456. PubMed PMID: 35081110; PubMed Central PMCID: PMCPMC8791498.
73. Kounatidis I, Chtarbanova S. Role of Glial Immunity in Lifespan Determination: A Drosophila Perspective. Front Immunol. 2018;9:1362. Epub 2018/06/27. doi: 10.3389/fimmu.2018.01362. PubMed PMID: 29942319; PubMed Central PMCID: PMCPMC6004738.
74. Shu S, Jiang M, Deng X, Yue W, Cao X, Zhang K, et al. Heterochromatic silencing of immune-related genes in glia is required for BBB integrity and normal lifespan in drosophila. Aging Cell.

2023;22(10):e13947. Epub 2023/08/18. doi: 10.1111/acel.13947. PubMed PMID: 37594178; PubMed Central PMCID: PMCPMC10577565.
75. Yi P, Johnson AN, Han Z, Wu J, Olson EN. Heterotrimeric G proteins regulate a noncanonical function of septate junction proteins to maintain cardiac integrity in Drosophila. Dev Cell. 2008;15(5):704-13. Epub 2008/11/13. doi: 10.1016/j.devcel.2008.10.001. PubMed PMID: 19000835; PubMed Central PMCID: PMCPMC2736786.
76. Jumper J, Evans R, Pritzel A, Green T, Figurnov M, Ronneberger O, et al. Highly accurate protein structure prediction with AlphaFold. Nature. 2021;596(7873):583-9. Epub 2021/07/16. doi: 10.1038/s41586-021-03819-2. PubMed PMID: 34265844; PubMed Central PMCID: PMCPMC8371605 have filed non-provisional patent applications 16/701,070 and PCT/EP2020/084238, and provisional patent applications 63/107,362, 63/118,917, 63/118,918, 63/118,921 and 63/118,919, each in the name of DeepMind Technologies Limited, each pending, relating to machine learning for predicting protein structures. The other authors declare no competing interests.
77. Hartenstein V. Morphological diversity and development of glia in Drosophila. Glia. 2011;59(9):1237-52. Epub 2011/03/26. doi: 10.1002/glia.21162. PubMed PMID: 21438012; PubMed Central PMCID: PMCPMC3950653.
78. Silies M, Yuva Y, Engelen D, Aho A, Stork T, Klambt C. Glial cell migration in the eye disc. J Neurosci. 2007;27(48):13130-9. Epub 2007/11/30. doi: 10.1523/JNEUROSCI.3583-07.2007. PubMed PMID: 18045907; PubMed Central PMCID: PMCPMC6673417.
79. Guerra F, Bucci C. Multiple Roles of the Small GTPase Rab7. Cells. 2016;5(3). Epub 2016/08/23. doi: 10.3390/cells5030034. PubMed PMID: 27548222; PubMed Central PMCID: PMCPMC5040976.
80. Feng Y, He D, Yao Z, Klionsky DJ. The machinery of macroautophagy. Cell Res. 2014;24(1):24-41. Epub 2013/12/25. doi: 10.1038/cr.2013.168. PubMed PMID: 24366339; PubMed Central PMCID: PMCPMC3879710.
81. Xu T, Nicolson S, Sandow JJ, Dayan S, Jiang X, Manning JA, et al. Cp1/cathepsin L is required for autolysosomal clearance in Drosophila. Autophagy. 2021;17(10):2734-49. Epub 2020/10/29. doi: 10.1080/15548627.2020.1838105. PubMed PMID: 33112206; PubMed Central PMCID: PMCPMC8526001.
82. Sujkowski A, Rainier S, Fink JK, Wessells RJ. Delayed Induction of Human NTE (PNPLA6) Rescues Neurodegeneration and Mobility Defects of Drosophila swiss cheese (sws) Mutants. PloS one. 2015;10(12):e0145356. Epub 2015/12/17. doi: 10.1371/journal.pone.0145356. PubMed PMID: 26671664; PubMed Central PMCID: PMCPMC4684404.
83. Sunderhaus ER, Law AD, Kretzschmar D. ER responses play a key role in Swiss-Cheese/Neuropathy Target Esterase-associated neurodegeneration. Neurobiol Dis. 2019;130:104520. Epub 2019/06/25. doi: 10.1016/j.nbd.2019.104520. PubMed PMID: 31233884; PubMed Central PMCID: PMCPMC6690343.
84. Cao M, Luo X, Wu K, He X. Targeting lysosomes in human disease: from basic research to clinical applications. Signal Transduct Target Ther. 2021;6(1):379. Epub 2021/11/09. doi: 10.1038/s41392-021-00778-y. PubMed PMID: 34744168; PubMed Central PMCID: PMCPMC8572923.
85. Hebbar S, Khandelwal A, Jayashree R, Hindle SJ, Chiang YN, Yew JY, et al. Lipid metabolic perturbation is an early-onset phenotype in adult spinster mutants: a Drosophila model for lysosomal storage disorders. Mol Biol Cell. 2017;28(26):3728-40. Epub 2017/10/20. doi: 10.1091/mbc.E16-09-0674. PubMed PMID: 29046397; PubMed Central PMCID: PMCPMC5739291.
86. Xu S, Stern M, McNew JA. Beneficial effects of rapamycin in a Drosophila model for hereditary spastic paraplegia. J Cell Sci. 2017;130(2):453-65. Epub 2016/12/03. doi: 10.1242/jcs.196741. PubMed PMID: 27909242; PubMed Central PMCID: PMCPMC5278673.
87. Kim SY, Buckwalter M, Soreq H, Vezzani A, Kaufer D. Blood-brain barrier dysfunction-induced inflammatory signaling in brain pathology and epileptogenesis. Epilepsia. 2012;53 Suppl 6(0 6):37-44. Epub 2013/01/03. doi: 10.1111/j.1528-1167.2012.03701.x. PubMed PMID: 23134494; PubMed Central PMCID: PMCPMC3703535.

88. Bainton RJ, Tsai LT, Schwabe T, DeSalvo M, Gaul U, Heberlein U. moody encodes two GPCRs that regulate cocaine behaviors and blood-brain barrier permeability in Drosophila. Cell. 2005;123(1):145-56. Epub 2005/10/11. doi: 10.1016/j.cell.2005.07.029. PubMed PMID: 16213219.
89. Cao Y, Chtarbanova S, Petersen AJ, Ganetzky B. Dnr1 mutations cause neurodegeneration in Drosophila by activating the innate immune response in the brain. Proc Natl Acad Sci U S A. 2013;110(19):E1752-60. Epub 2013/04/25. doi: 10.1073/pnas.1306220110. PubMed PMID: 23613578; PubMed Central PMCID: PMCPMC3651420.
90. Kounatidis I, Chtarbanova S, Cao Y, Hayne M, Jayanth D, Ganetzky B, et al. NF-kappaB Immunity in the Brain Determines Fly Lifespan in Healthy Aging and Age-Related Neurodegeneration. Cell Rep. 2017;19(4):836-48. Epub 2017/04/27. doi: 10.1016/j.celrep.2017.04.007. PubMed PMID: 28445733; PubMed Central PMCID: PMCPMC5413584.
91. Stanley D, Kim Y. Prostaglandins and Other Eicosanoids in Insects: Biosynthesis and Biological Actions. Front Physiol. 2018;9:1927. Epub 2019/02/23. doi: 10.3389/fphys.2018.01927. PubMed PMID: 30792667; PubMed Central PMCID: PMCPMC6375067.
92. von Hanstein AS, Tsikas D, Lenzen S, Jorns A, Plotz T. Potentiation of Lipotoxicity in Human EndoC-betaH1 beta-Cells by Glucose is Dependent on the Structure of Free Fatty Acids. Mol Nutr Food Res. 2023;67(5):e2200582. Epub 2023/01/12. doi: 10.1002/mnfr.202200582. PubMed PMID: 36629272.
93. Miao H, Chen L, Hao L, Zhang X, Chen Y, Ruan Z, et al. Stearic acid induces proinflammatory cytokine production partly through activation of lactate-HIF1alpha pathway in chondrocytes. Scientific reports. 2015;5:13092. Epub 2015/08/15. doi: 10.1038/srep13092. PubMed PMID: 26271607; PubMed Central PMCID: PMCPMC4536527.
94. Korbecki J, Bajdak-Rusinek K. The effect of palmitic acid on inflammatory response in macrophages: an overview of molecular mechanisms. Inflamm Res. 2019;68(11):915-32. Epub 2019/08/01. doi: 10.1007/s00011-019-01273-5. PubMed PMID: 31363792; PubMed Central PMCID: PMCPMC6813288.
95. Cattenoz PB, Monticelli S, Pavlidaki A, Giangrande A. Toward a Consensus in the Repertoire of Hemocytes Identified in Drosophila. Front Cell Dev Biol. 2021;9:643712. Epub 2021/03/23. doi: 10.3389/fcell.2021.643712. PubMed PMID: 33748138; PubMed Central PMCID: PMCPMC7969988.
96. Kurucz E, Markus R, Zsamboki J, Folkl-Medzihradszky K, Darula Z, Vilmos P, et al. Nimrod, a putative phagocytosis receptor with EGF repeats in Drosophila plasmatocytes. Curr Biol. 2007;17(7):649-54. Epub 2007/03/17. doi: 10.1016/j.cub.2007.02.041. PubMed PMID: 17363253.
97. Schwabe T, Bainton RJ, Fetter RD, Heberlein U, Gaul U. GPCR signaling is required for blood-brain barrier formation in drosophila. Cell. 2005;123(1):133-44. Epub 2005/10/11. doi: 10.1016/j.cell.2005.08.037. PubMed PMID: 16213218.
98. Li X, Fetter R, Schwabe T, Jung C, Liu L, Steller H, et al. The cAMP effector PKA mediates Moody GPCR signaling in Drosophila blood-brain barrier formation and maturation. Elife. 2021;10. Epub 2021/08/13. doi: 10.7554/eLife.68275. PubMed PMID: 34382936; PubMed Central PMCID: PMCPMC8390003.
99. Giepmans BN, van Ijzendoorn SC. Epithelial cell-cell junctions and plasma membrane domains. Biochim Biophys Acta. 2009;1788(4):820-31. Epub 2008/08/19. doi: 10.1016/j.bbamem.2008.07.015. PubMed PMID: 18706883.
100. Lee DB, Jamgotchian N, Allen SG, Abeles MB, Ward HJ. A lipid-protein hybrid model for tight junction. Am J Physiol Renal Physiol. 2008;295(6):F1601-12. Epub 2008/08/15. doi: 10.1152/ajprenal.00097.2008. PubMed PMID: 18701633; PubMed Central PMCID: PMCPMC2604825.
101. Shigetomi K, Ono Y, Matsuzawa K, Ikenouchi J. Cholesterol-rich domain formation mediated by ZO proteins is essential for tight junction formation. Proc Natl Acad Sci U S A. 2023;120(8):e2217561120. Epub 2023/02/16. doi: 10.1073/pnas.2217561120. PubMed PMID: 36791108; PubMed Central PMCID: PMCPMC9974431.
102. Nusrat A, Parkos CA, Verkade P, Foley CS, Liang TW, Innis-Whitehouse W, et al. Tight junctions are membrane microdomains. J Cell Sci. 2000;113 (Pt 10):1771-81. Epub 2000/04/19. doi: 10.1242/jcs.113.10.1771. PubMed PMID: 10769208.

103. Simons K, Vaz WL. Model systems, lipid rafts, and cell membranes. Annu Rev Biophys Biomol Struct. 2004;33:269-95. Epub 2004/05/14. doi: 10.1146/annurev.biophys.32.110601.141803. PubMed PMID: 15139814.
104. Muhlig-Versen M, da Cruz AB, Tschape JA, Moser M, Buttner R, Athenstaedt K, et al. Loss of Swiss cheese/neuropathy target esterase activity causes disruption of phosphatidylcholine homeostasis and neuronal and glial death in adult Drosophila. J Neurosci. 2005;25(11):2865-73. Epub 2005/03/18. doi: 10.1523/JNEUROSCI.5097-04.2005. PubMed PMID: 15772346; PubMed Central PMCID: PMCPMC1182176.
105. Bundgaard M, Abbott NJ. All vertebrates started out with a glial blood-brain barrier 4-500 million years ago. Glia. 2008;56(7):699-708. Epub 2008/03/15. doi: 10.1002/glia.20642. PubMed PMID: 18338790.
106. Kadry H, Noorani B, Cucullo L. A blood-brain barrier overview on structure, function, impairment, and biomarkers of integrity. Fluids Barriers CNS. 2020;17(1):69. Epub 2020/11/20. doi: 10.1186/s12987-020-00230-3. PubMed PMID: 33208141; PubMed Central PMCID: PMCPMC7672931.
107. Kondo Y, Wenger DA, Gallo V, Duncan ID. Galactocerebrosidase-deficient oligodendrocytes maintain stable central myelin by exogenous replacement of the missing enzyme in mice. Proc Natl Acad Sci U S A. 2005;102(51):18670-5. Epub 2005/12/15. doi: 10.1073/pnas.0506473102. PubMed PMID: 16352725; PubMed Central PMCID: PMCPMC1317926.
108. Tschopp J, Schroder K. NLRP3 inflammasome activation: The convergence of multiple signalling pathways on ROS production? Nat Rev Immunol. 2010;10(3):210-5. Epub 2010/02/20. doi: 10.1038/nri2725. PubMed PMID: 20168318.
109. Sezgin E, Levental I, Mayor S, Eggeling C. The mystery of membrane organization: composition, regulation and roles of lipid rafts. Nat Rev Mol Cell Biol. 2017;18(6):361-74. Epub 2017/03/31. doi: 10.1038/nrm.2017.16. PubMed PMID: 28356571; PubMed Central PMCID: PMCPMC5500228.
110. Yang Y, Lee M, Fairn GD. Phospholipid subcellular localization and dynamics. J Biol Chem. 2018;293(17):6230-40. Epub 2018/03/29. doi: 10.1074/jbc.R117.000582. PubMed PMID: 29588369; PubMed Central PMCID: PMCPMC5925819.
111. Epand RM, Epand RF. Calorimetric detection of curvature strain in phospholipid bilayers. Biophys J. 1994;66(5):1450-6. Epub 1994/05/01. doi: 10.1016/S0006-3495(94)80935-X. PubMed PMID: 8061194; PubMed Central PMCID: PMCPMC1275865.
112. Thelen AM, Zoncu R. Emerging Roles for the Lysosome in Lipid Metabolism. Trends Cell Biol. 2017;27(11):833-50. Epub 2017/08/26. doi: 10.1016/j.tcb.2017.07.006. PubMed PMID: 28838620; PubMed Central PMCID: PMCPMC5653458.
113. Grassi S, Giussani P, Mauri L, Prioni S, Sonnino S, Prinetti A. Lipid rafts and neurodegeneration: structural and functional roles in physiologic aging and neurodegenerative diseases. J Lipid Res. 2020;61(5):636-54. Epub 2019/12/25. doi: 10.1194/jlr.TR119000427. PubMed PMID: 31871065; PubMed Central PMCID: PMCPMC7193971.
114. Udayar V, Chen Y, Sidransky E, Jagasia R. Lysosomal dysfunction in neurodegeneration: emerging concepts and methods. Trends Neurosci. 2022;45(3):184-99. Epub 2022/01/18. doi: 10.1016/j.tins.2021.12.004. PubMed PMID: 35034773; PubMed Central PMCID: PMCPMC8854344.
115. Domon MM, Besson F, Bandorowicz-Pikula J, Pikula S. Annexin A6 is recruited into lipid rafts of Niemann-Pick type C disease fibroblasts in a Ca2+-dependent manner. Biochem Biophys Res Commun. 2011;405(2):192-6. Epub 2011/01/11. doi: 10.1016/j.bbrc.2010.12.138. PubMed PMID: 21216236.
116. Vainio S, Bykov I, Hermansson M, Jokitalo E, Somerharju P, Ikonen E. Defective insulin receptor activation and altered lipid rafts in Niemann-Pick type C disease hepatocytes. Biochem J. 2005;391(Pt 3):465-72. Epub 2005/06/10. doi: 10.1042/BJ20050460. PubMed PMID: 15943586; PubMed Central PMCID: PMCPMC1276947.
117. Seehafer SS, Ramirez-Montealegre D, Wong AM, Chan CH, Castaneda J, Horak M, et al. Immunosuppression alters disease severity in juvenile Batten disease mice. J Neuroimmunol. 2011;230(1-2):169-72. Epub 2010/10/13. doi: 10.1016/j.jneuroim.2010.08.024. PubMed PMID: 20937531; PubMed Central PMCID: PMCPMC3118572.

118. DiRosario J, Divers E, Wang C, Etter J, Charrier A, Jukkola P, et al. Innate and adaptive immune activation in the brain of MPS IIIB mouse model. J Neurosci Res. 2009;87(4):978-90. Epub 2008/10/28. doi: 10.1002/jnr.21912. PubMed PMID: 18951493.
119. Kim SJ, Zhang Z, Hitomi E, Lee YC, Mukherjee AB. Endoplasmic reticulum stress-induced caspase-4 activation mediates apoptosis and neurodegeneration in INCL. Hum Mol Genet. 2006;15(11):1826-34. Epub 2006/04/29. doi: 10.1093/hmg/ddl105. PubMed PMID: 16644870.
120. Tessitore A, del PMM, Sano R, Ma Y, Mann L, Ingrassia A, et al. GM1-ganglioside-mediated activation of the unfolded protein response causes neuronal death in a neurodegenerative gangliosidosis. Mol Cell. 2004;15(5):753-66. Epub 2004/09/08. doi: 10.1016/j.molcel.2004.08.029. PubMed PMID: 15350219.
121. Sheth J, Nair A. Treatment for Lysosomal Storage Disorders. Curr Pharm Des. 2020;26(40):5110-8. Epub 2020/10/17. doi: 10.2174/1381612826666201015154932. PubMed PMID: 33059565.
122. Ozkan N, Koppers M, van Soest I, van Harten A, Jurriens D, Liv N, et al. ER - lysosome contacts at a pre-axonal region regulate axonal lysosome availability. Nature communications. 2021;12(1):4493. Epub 2021/07/25. doi: 10.1038/s41467-021-24713-5. PubMed PMID: 34301956; PubMed Central PMCID: PMCPMC8302662.
123. Wu Y, Whiteus C, Xu CS, Hayworth KJ, Weinberg RJ, Hess HF, et al. Contacts between the endoplasmic reticulum and other membranes in neurons. Proc Natl Acad Sci U S A. 2017;114(24):E4859-E67. Epub 2017/06/01. doi: 10.1073/pnas.1701078114. PubMed PMID: 28559323; PubMed Central PMCID: PMCPMC5474793.
124. Li C, Qian T, He R, Wan C, Liu Y, Yu H. Endoplasmic Reticulum-Plasma Membrane Contact Sites: Regulators, Mechanisms, and Physiological Functions. Front Cell Dev Biol. 2021;9:627700. Epub 2021/02/23. doi: 10.3389/fcell.2021.627700. PubMed PMID: 33614657; PubMed Central PMCID: PMCPMC7889955.
125. Kun-Rodrigues C, Ganos C, Guerreiro R, Schneider SA, Schulte C, Lesage S, et al. A systematic screening to identify de novo mutations causing sporadic early-onset Parkinson's disease. Hum Mol Genet. 2015;24(23):6711-20. Epub 2015/09/13. doi: 10.1093/hmg/ddv376. PubMed PMID: 26362251; PubMed Central PMCID: PMCPMC4634375.
126. Anagnostou G, Akbar MT, Paul P, Angelinetta C, Steiner TJ, de Belleroche J. Vesicle associated membrane protein B (VAPB) is decreased in ALS spinal cord. Neurobiol Aging. 2010;31(6):969-85. Epub 2008/08/15. doi: 10.1016/j.neurobiolaging.2008.07.005. PubMed PMID: 18701194.
127. Wilson EL, Metzakopian E. ER-mitochondria contact sites in neurodegeneration: genetic screening approaches to investigate novel disease mechanisms. Cell Death Differ. 2021;28(6):1804-21. Epub 2020/12/19. doi: 10.1038/s41418-020-00705-8. PubMed PMID: 33335290; PubMed Central PMCID: PMCPMC8185109.
128. Pifferi F, Laurent B, Plourde M. Lipid Transport and Metabolism at the Blood-Brain Interface: Implications in Health and Disease. Front Physiol. 2021;12:645646. Epub 2021/04/20. doi: 10.3389/fphys.2021.645646. PubMed PMID: 33868013; PubMed Central PMCID: PMCPMC8044814.
129. Soardo G, Donnini D, Domenis L, Catena C, De Silvestri D, Cappello D, et al. Oxidative stress is activated by free fatty acids in cultured human hepatocytes. Metab Syndr Relat Disord. 2011;9(5):397-401. Epub 2011/05/13. doi: 10.1089/met.2010.0140. PubMed PMID: 21561340.
130. Ly LD, Xu S, Choi SK, Ha CM, Thoudam T, Cha SK, et al. Oxidative stress and calcium dysregulation by palmitate in type 2 diabetes. Exp Mol Med. 2017;49(2):e291. Epub 2017/02/06. doi: 10.1038/emm.2016.157. PubMed PMID: 28154371; PubMed Central PMCID: PMCPMC5336562.
131. Yasuda M, Tanaka Y, Kume S, Morita Y, Chin-Kanasaki M, Araki H, et al. Fatty acids are novel nutrient factors to regulate mTORC1 lysosomal localization and apoptosis in podocytes. Biochim Biophys Acta. 2014;1842(7):1097-108. Epub 2014/04/15. doi: 10.1016/j.bbadis.2014.04.001. PubMed PMID: 24726883.
132. Kwon SY, Massey K, Watson MA, Hussain T, Volpe G, Buckley CD, et al. Oxidised metabolites of the omega-6 fatty acid linoleic acid activate dFOXO. Life Sci Alliance. 2020;3(2). Epub 2020/01/30. doi: 10.26508/lsa.201900356. PubMed PMID: 31992650; PubMed Central PMCID: PMCPMC6988086.

133. van der Lee SJ, Teunissen CE, Pool R, Shipley MJ, Teumer A, Chouraki V, et al. Circulating metabolites and general cognitive ability and dementia: Evidence from 11 cohort studies. Alzheimers Dement. 2018;14(6):707-22. Epub 2018/01/10. doi: 10.1016/j.jalz.2017.11.012. PubMed PMID: 29316447.
134. Rao JS, Rapoport SI, Kim HW. Altered neuroinflammatory, arachidonic acid cascade and synaptic markers in postmortem Alzheimer's disease brain. Transl Psychiatry. 2017;7(5):e1127. Epub 2017/05/10. doi: 10.1038/tp.2017.97. PubMed PMID: 28485730; PubMed Central PMCID: PMCPMC5534965.
135. Regulska M, Szuster-Gluszczak M, Trojan E, Leskiewicz M, Basta-Kaim A. The Emerging Role of the Double-Edged Impact of Arachidonic Acid- Derived Eicosanoids in the Neuroinflammatory Background of Depression. Curr Neuropharmacol. 2021;19(2):278-93. Epub 2020/08/28. doi: 10.2174/1570159X18666200807144530. PubMed PMID: 32851950; PubMed Central PMCID: PMCPMC8033972.
136. Funk CD. Prostaglandins and leukotrienes: advances in eicosanoid biology. Science. 2001;294(5548):1871-5. Epub 2001/12/01. doi: 10.1126/science.294.5548.1871. PubMed PMID: 11729303.
137. Keating N. A research framework for the United Nations Decade of Healthy Ageing (2021-2030). Eur J Ageing. 2022:1-13. Epub 2022/01/18. doi: 10.1007/s10433-021-00679-7. PubMed PMID: 35035341; PubMed Central PMCID: PMCPMC8753942.
138. Rudnicka E, Napierala P, Podfigurna A, Meczekalski B, Smolarczyk R, Grymowicz M. The World Health Organization (WHO) approach to healthy ageing. Maturitas. 2020;139:6-11. Epub 2020/08/05. doi: 10.1016/j.maturitas.2020.05.018. PubMed PMID: 32747042; PubMed Central PMCID: PMCPMC7250103.
139. Crimmins E, Vasunilashorn S, Kim JK, Alley D. Biomarkers related to aging in human populations. Adv Clin Chem. 2008;46:161-216. Epub 2008/11/14. doi: 10.1016/s0065-2423(08)00405-8. PubMed PMID: 19004190; PubMed Central PMCID: PMCPMC5938178.
140. Brand AH, Perrimon N. Targeted gene expression as a means of altering cell fates and generating dominant phenotypes. Development. 1993;118(2):401-15. Epub 1993/06/01. doi: 10.1242/dev.118.2.401. PubMed PMID: 8223268.
141. Hayashi S, Ito K, Sado Y, Taniguchi M, Akimoto A, Takeuchi H, et al. GETDB, a database compiling expression patterns and molecular locations of a collection of Gal4 enhancer traps. Genesis. 2002;34(1-2):58-61. Epub 2002/09/27. doi: 10.1002/gene.10137. PubMed PMID: 12324948.
142. Kucherenko MM, Marrone AK, Rishko VM, Yatsenko AS, Klepzig A, Shcherbata HR. Paraffin-embedded and frozen sections of Drosophila adult muscles. Journal of visualized experiments : JoVE. 2010;(46). Epub 2011/01/06. doi: 10.3791/2438. PubMed PMID: 21206479; PubMed Central PMCID: PMCPMC3159657.
143. Shcherbata HR, Yatsenko AS, Patterson L, Sood VD, Nudel U, Yaffe D, et al. Dissecting muscle and neuronal disorders in a Drosophila model of muscular dystrophy. EMBO J. 2007;26(2):481-93. Epub 2007/01/12. doi: 10.1038/sj.emboj.7601503. PubMed PMID: 17215867; PubMed Central PMCID: PMCPMC1783456.
144. Mariani S, Li T, Hegermann J, Bounader K, Hanke J, Meyer T, et al. Biocompatibility of an apical ring plug for left ventricular assist device explantation: Results of a feasibility pre-clinical study. Artif Organs. 2022;46(5):827-37. Epub 2021/12/15. doi: 10.1111/aor.14149. PubMed PMID: 34904254.

1

Key Resources Table				
Reagent type (species) or resource	**Designation**	**Source or reference**	**Identifiers**	**Additional information**
antibody	anti-Repo (mouse monoclonal)	Developmental Studies Hybridoma Bank	#8D12	IF(1:50)
antibody	anti-CoraC (mouse monoclonal)	Developmental Studies Hybridoma Bank	#C566.9	IF(1:50)
antibody	anti-Rab7 (mouse monoclonal)	Developmental Studies Hybridoma Bank	#AB2722471	IF(1:50)
antibody	anti-DE-Cad (rat monoclonal)	Developmental Studies Hybridoma Bank	#DCAD2	IF(1:50)
antibody	anti-GFP (chicken polyclonal)	Abcam	#ab13970	IF(1:1000)
antibody	anti-mCherry (rabbit polyclonal)	Abcam	#ab167453	IF(1:1000)
antibody	Anti-β-Galactosidase (mouse monoclonal)	Promega	#Z3781	IF(1:200)
antibody	anti-CathepsinL (mouse)	R&D Systems	#1515-CY-010	IF(1:400)
antibody	anti-NrxIV (rabbit polyclonal)	Gift from Christian Klämbt	anti-NrxIV	IF(1:1000)
antibody	anti-SWS (rabbit polyclonal)	Gift from Doris Kretzschmar	anti-SWS	IF(1:1000)
antibody	Anti-NimC1 (mouse)	Gift from István Andó	anti-NimC1	IF(1:300)
antibody	anti-chicken Alexa 488 (goat polyclonal)	Thermo Fisher Scientific	#A-11039	Secondary antibody IF(1:500)
antibody	anti-rat Alexa 488 (goat polyclonal)	Thermo Fisher Scientific	#A-11077	Secondary antibody IF(1:500)
antibody	anti-rat Alexa 647 (goat polyclonal)	Thermo Fisher Scientific	#A-21247	Secondary antibody IF(1:500)
antibody	anti- rabbit Alexa 488 (goat polyclonal)	Thermo Fisher Scientific	#A-11034	Secondary antibody IF(1:500)
antibody	anti- rabbit Alexa 568 (goat	Thermo Fisher Scientific	#A-11011	Secondary antibody

	polyclonal)			IF(1:500)
antibody	anti-mouse IgG2a Cy3 (goat polyclonal)	Jackson ImmunoResearch	#115-165-206	Secondary antibody IF(1:400)
antibody	anti- mouse IG1 Cy3 (goat polyclonal)	Jackson ImmunoResearch	#115-165-205	Secondary antibody IF(1:500)
antibody	anti-mouse IgG1 647 (goat polyclonal)	Jackson ImmunoResearch	#115-605-205	Secondary antibody IF(1:500)
genetic reagent (*D. melanogaster*)	*w[1118]*	Bloomington Drosophila Stock Center	BDSC 5905	Wild type strain
genetic reagent (*D. melanogaster*)	*Oregon-R*	Bloomington Drosophila Stock Center	BDSC 5	Wild type strain
genetic reagent (*D. melanogaster*)	sws^{1}	Gift from Doris Kretzschmar	sws^{1}	*sws[1]/FM7a* (null mutant)
genetic reagent (*D. melanogaster*)	sws^{4}	Bloomington Drosophila Stock Center	BDSC 28121	*sws[4]/C(1)DX, y[1] w[1] f[1]* (Amino acid replacement: G956D)
genetic reagent (*D. melanogaster*)	*UAS-sws*	Gift from Doris Kretzschmar	*UAS-sws*	*UAS-sws* (*sws* gene under control of UAS promotor)
genetic reagent (*D. melanogaster*)	*sws-Gal4*	Kyoto Stock Center	104592	*y* w* P{GawB}swsNP4072 / FM7c*
genetic reagent (*D. melanogaster*)	*UAS-nlsLacZ, UAS-CD8::GFP*	Gift from Frank Hirth	*UAS-nLacZ, UAS-GFP*	*UAS-nlsLacZ, UAS-CD8::GFP* (nLacZ and GFP constructs under control of UAS promotor)
genetic reagent (*D. melanogaster*)	*UAS-hNTE*	Gift from Robert Wessells	*UAS-hNTE*	*w[1118]; p[PUAST]-hNTE/CyO* (Human NTE under control of UAS promotor)
genetic reagent (*D. melanogaster*)	$UAS\text{-}sws^{RNAi}$	Bloomington Drosophila Stock Center	BDSC 61338	*y[1] v[1]; P{y[+t7.7] v[+t1.8]=TRiP.HMJ23229}attP40* (*sws* RNAi construct under control of UAS promotor)
genetic reagent	*repo-Gal4, UAS-*	Gift from Mikael	*repo-Gal4*	*repo-Gal4, UAS-*

(*D. melanogaster*)	*CD8::GFP/TM6B*	Simons		*CD8::GFP/TM6B*
genetic reagent (*D. melanogaster*)	*Gliotactin-Gal4, UAS-CD8::GFP*	Gift from Mikael Simons	*Gli-Gal4*	*Gliotactin-Gal4, UAS-CD8::GFP*
genetic reagent (*D. melanogaster*)	*moody-Gal4, UAS-CD8::GFP*	Gift from Mikael Simons	*moody-Gal4*	*moody-Gal4, UAS-CD8::GFP*
genetic reagent (*D. melanogaster*)	*nSyb-Gal4*	Bloomington Drosophila Stock Center	BDSC 51945	*y[1] w[1118]; P{y[+t7.7] w[+mC]=nSyb-GAL4.DBD::QF.AD}attP2*
genetic reagent (*D. melanogaster*)	*repo-Gal4, nSyb-Gal4, UAS-CD8::GFP/TM6B, Sb*	This study	*repo-Gal4, nSyb-Gal4*	*repo-Gal4, nSyb-Gal4, UAS-CD8::GFP/TM6B, Sb*
genetic reagent (*D. melanogaster*)	*tub-Gal80^{ts}; repo-Gal4/TM6B*	This study	*tub-Gal80^{ts}; repo-Gal4/TM6B*	*tub-Gal80^{ts}; repo-Gal4/TM6B* (temperature sensitive)
genetic reagent (*D. melanogaster*)	*moody$^{\Delta C17}$*	Gift from Christian Klämbt	*moody$^{\Delta C17}$*	Null mutant
genetic reagent (*D. melanogaster*)	*UAS-moody^{RNAi}*	Bloomington Drosophila Stock Center	BDSC 66326	*y[1] sc[*] v[1] sev[21]; P{y[+t7.7] v[+t1.8]=TRiP.HMC06237}attP2* (*moody* RNAi construct under control of UAS promotor)
genetic reagent (*D. melanogaster*)	*UAS-Dysb^{RNAi}*	Bloomington Drosophila Stock Center	BDSC 67316	*y[1] sc[*] v[1] sev[21]; P{y[+t7.7] v[+t1.8]=TRiP.HMC06420}attP40/CyO* (*Dysb* RNAi construct under control of UAS promotor)
genetic reagent (*D. melanogaster*)	*UAS-Npc1a^{RNAi}*	Bloomington Drosophila Stock Center	BDSC 37504	*y[1] sc[*] v[1] sev[21]; P{y[+t7.7] v[+t1.8]=TRiP.HMS01646}attP40* (*Npc1a* RNAi construct under control of UAS promotor)
genetic reagent (*D. melanogaster*)	*UAS-Pldn^{RNAi}*	Bloomington Drosophila Stock Center	BDSC 67884	*y[1] sc[*] v[1] sev[21]; P{y[+t7.7] v[+t1.8]=TRiP.HMS05728}attP40* (*Pldn* RNAi construct under

				control of UAS promotor)
genetic reagent (*D. melanogaster*)	*UAS-spin^{RNAi}*	Bloomington Drosophila Stock Center	BDSC 27702	*y[1] v[1]; P{y[+t7.7] v[+t1.8]=TRiP.JF 02782}attP2* (*spin* RNAi construct under control of UAS promotor)
genetic reagent (*D. melanogaster*)	*srp(Hemo) 3xmCherry*	Gift from Angela Giangrande	*srp(Hemo)3x mCherry*	*srp(Hemo) 3xmCherry*
software, algorithm	Microsoft Excel	Microsoft	Microsoft Excel	
software, algorithm	Adobe Photoshop	Adobe	Adobe CC	
software, algorithm	Zen 2011	Carl Zeiss	Zen 2011	
software, algorithm	AlphaFold2	https://colab.research.google.com/github/sokrypton/ColabFold/blob/main/AlphaFold2.ipynb	AlphaFold2	
software, algorithm	PyMol	https://pymol.org/	PyMol	
software, algorithm	StepOne Software v2.3	Applied Biosystems	StepOne	
chemical compound, drug	TRIzol reagent	Invitrogen	#15596018	
commercial assay or kit	High Capacity cDNA Reverse Transcription kit	Applied Biosystems	#4368813	
commercial assay or kit	FastSYBR® Green master mix	Applied Biosystems	#435612	
chemical compound, drug	TUDCA	Sigma Aldrich	#580549	Tauroursodeoxycholic Acid
chemical compound, drug	4-PBA	Sigma Aldrich	#567616	4-Phenylbutyric acid
chemical compound, drug	Valsartan	Sigma Aldrich	#PHR1315	
chemical compound, drug	Fenofibrate	Sigma Aldrich	#F6020	
chemical compound, drug	Sodium Salicylate	Sigma Aldrich	#S3007	
chemical compound, drug	Rapamycin	Sigma Aldrich	#R0395	
chemical compound, drug	Deferoxamine mesylate salt	Sigma Aldrich	#D9533	

chemical compound, drug	Liproxstatin-1	Sigma Aldrich	#SML1414	
chemical compound, drug	Sphingosine	Sigma Aldrich	#860025P	
chemical compound, drug	Brilliant Blue	Sigma Aldrich	#80717	
chemical compound, drug	Acetic Acid	Sigma Aldrich	#27225-1L-M	
chemical compound, drug	Chloroform	Sigma Aldrich	#288306-2L	
chemical compound, drug	Glycerol	Sigma Aldrich	#G6279-1L	
chemical compound, drug	Sodium azide	Sigma Aldrich	#S2002-25G	
chemical compound, drug	Formaldehyde, 16%	Polysciences Inc.	#18814-20	methanol free, ultra pure
other	10 kDa Dextran	Molecular Probes	#D1864	Dye labeled with Texas Red
other	DAPI stain	Sigma Aldrich	#D9542-10MG	IF concentration used: 1 µg/mL
other	Normal Goat Serum	Abcam	#ab7481	
other	Paraplast Plus	Sigma Aldrich	#76258-1KG	
other	Casein Blocking Buffer 10x	Sigma Aldrich	#B6429-500ML	
other	Hematoxylin Solution, Mayer’s	Sigma Aldrich	#MHS16-500ML	
other	Eosin Y solution, aqueous	Sigma Aldrich	#HT110232	
other	DPX Mountant for histology	Sigma Aldrich	#06522-100ML	
other	PBS buffer (10X Dulbecco's)	AppliChem	#A0965,9010	
other	LSM700 confocal laser-scanning microscope	Carl Zeiss	LSM700	
other	Hyrax M25 microtome	Carl Zeiss	Hyrax M25	
other	Zeiss EM 900 microscope	Carl Zeiss	Zeiss EM 900	
other	Step One Plus 96 well system	Applied Biosystems	Step One Plus	
organic solvent	acetonitrile	Honeywell	#34851	

organic solvent	toluene	Supelco	#1.08325.1000	
derivatization reagent	pentafluoro-benzyl bromide	Sigma-Aldrich	#101052	
organic base	diisopropyl-ethylamine	Sigma-Aldrich	#496219	
apparatus	GC-MS ISQ	ThermoFisher	Trace 1210 series	
GC column	Optima 17	Macherey-Nagel	#MN726022.15	
free fatty acid	C12:0; C12:1; C14:0; C14:1; C16:0; C16:1; C17:0; C17:1; C18:0; C18:1; C18:2; C18:3; C20:4; C20:5; C21:0; C22:0; C24:0	Merck (Darmstadt, Germany		
free fatty acid	C19:1; C20:0; C21:1	Larodan AB (Solna, Sweden)		
Fixative	Paraformaldehyde	Merck	#1.04005.1000	
Fixative	Glutaraldehyde	Merck	#1.04239.0250	
Fixative	Osmiumtetroxide	Electron Microscopy Sciences	#22400-56	
Buffer	HEPES	Roth	#7020.2	
Acetone	Acetone puriss.p.a. ACS reagent, reag.ISO 99, 5 %	Sigma Aldrich	#:32201-2.5	
Embedding resin	Agar 100 Premix Kit –Hard	Agar Scientific	#R1140	
EM poststain	Tri-Natriumcitrat-Dihydrat	Merck	#1-06448.0500	
EM poststain	Lead (II) nitrate for analysis	Merck	#1.07398.0100	

2

H&E

A Control

50 µm

B *sws[1]/sws[4]*

C

D

Perineurial glia(PG)
Subperineurial glia(SPG)
Cortex glia
Astrocyte-like glia
Ensheathing glia
CB neuropile

sws>CD8::GFP

Repo GFP DAPI

E

50 µm

Single section

F

Overlay

A Control
B *sws*^{1}
C *moody>sws*^{RNAi}
D *sws*^{1}*; moody>hNTE*
CoraC DAPI
50 µm
CoraC
E *moody>CD8::GFP*
F *sws*^{1}*; moody>GFP*
G *moody>GFP,sws*^{RNAi}
CoraC GFP DAPI
GFP
CoraC
50 µm
H
100%
80%
60%
40%
20%
0%
*** *** *** *** *** *n.s.* *n.s.* *** *** *n.s.* *n.s.* *** *** *n.s.* *n.s.*
Control
sws^{1}
sws^{1}/*sws*^{4}
repo,nSyb>*sws*^{RNAi}
repo>/Oregon R
repo>*sws*^{RNAi}
sws^{1};repo>*sws*
sws^{1};repo>*hNTE*
moody>/Oregon R
moody>*sws*^{RNAi}
sws^{1};moody>*sws*
sws^{1};moody>*hNTE*
Gli>/Oregon R
Gli>*sws*^{RNAi}
sws^{1};Gli>*sws*
sws^{1};Gli>*hNTE*
No lesions
Lesions
Lesions&Clusters

A Control

B *sws*^{1}

SWS DAPI

50 µm

A`

B`

SWS

A``

B``

SWS

C

Relative *sws* mRNA levels

7

6

5

4

3

2

1

0

***

**

***

***

***

repo>/Oregon R

repo>sws^{RNAi}

repo>sws

nSyb>/Oregon R

nSyb>sws^{RNAi}

nSyb>sws

repo,nSyb>/Oregon R

repo,nSyb>sws^{RNAi}

moody>CD8::GFP,nlacZ

Gli>CD8::GFP, nlacZ

repo, nSyb>CD8::GFP, nlacZ

Repo GFP βGal DAPI

D

50 µm

E

F

Repo βGal DAPI

D`

E`

F`

GFP

A Control

50 µm

B *sws*^{1}

C *repo>sws*^{RNAi}

D *Gli>sws*^{RNAi}

E *nSyb>sws*^{RNAi}

F *sws*^{1}*; moody>sws*

Control

Human NTE

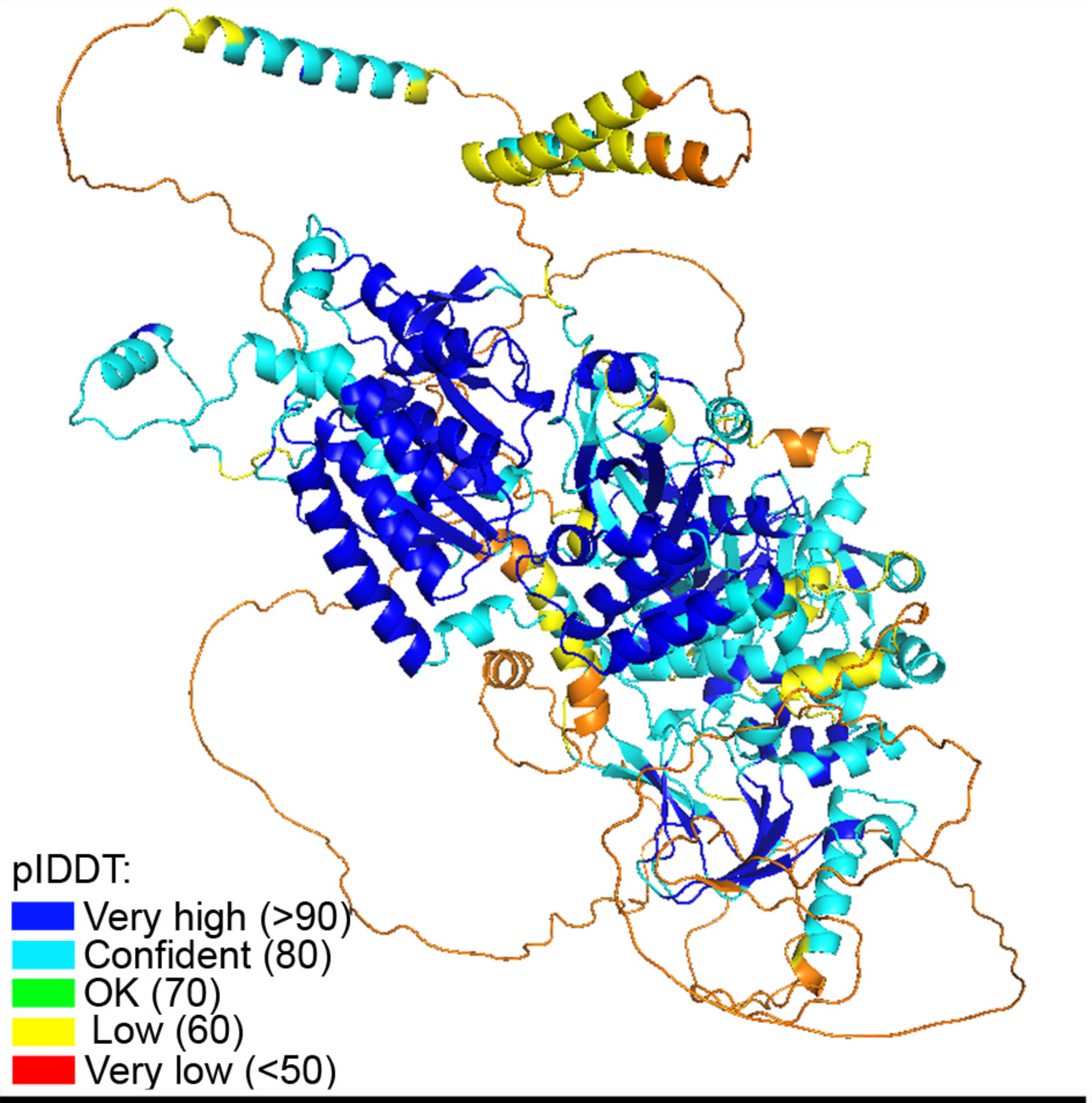

Drosophila SWS

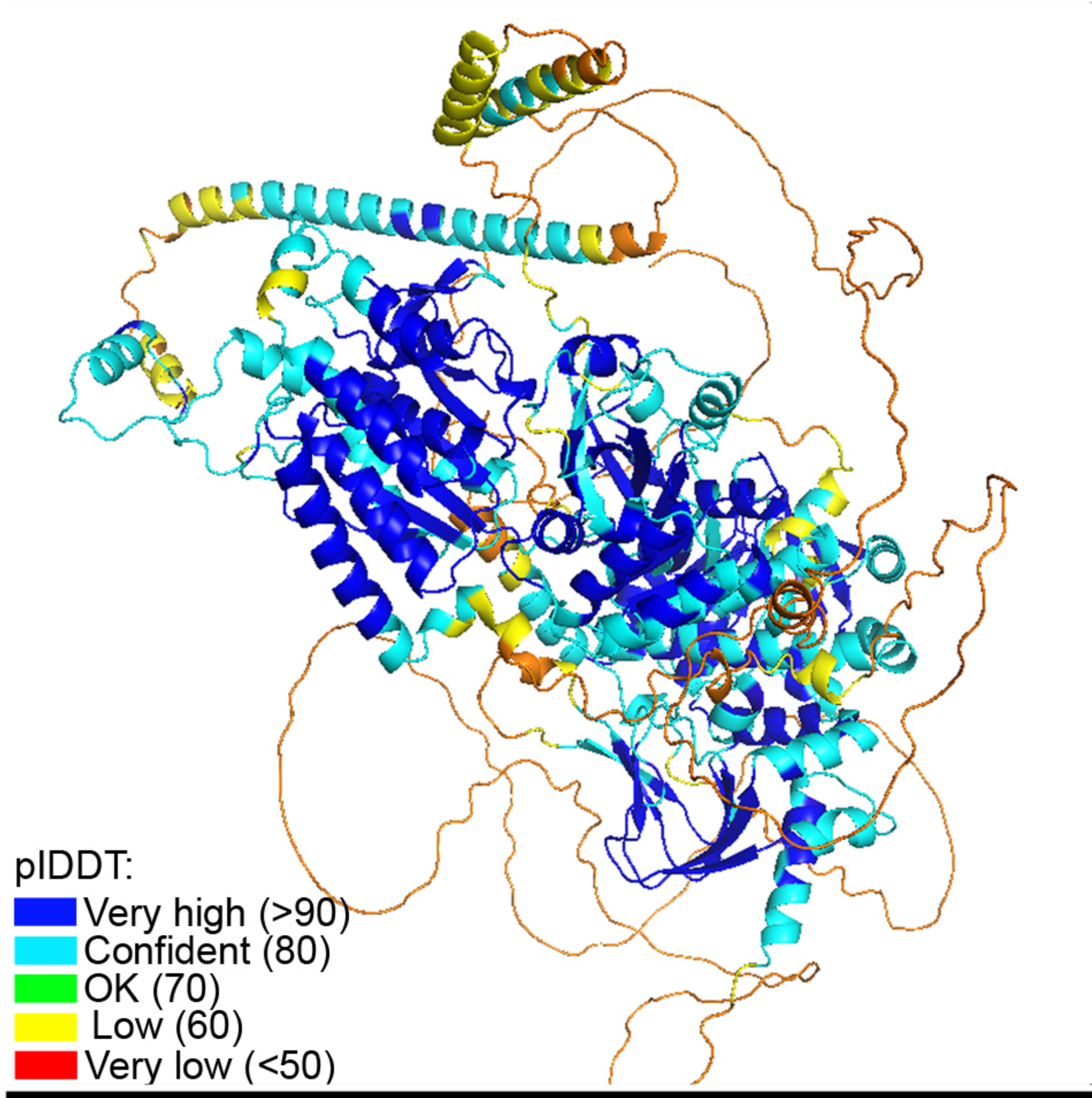

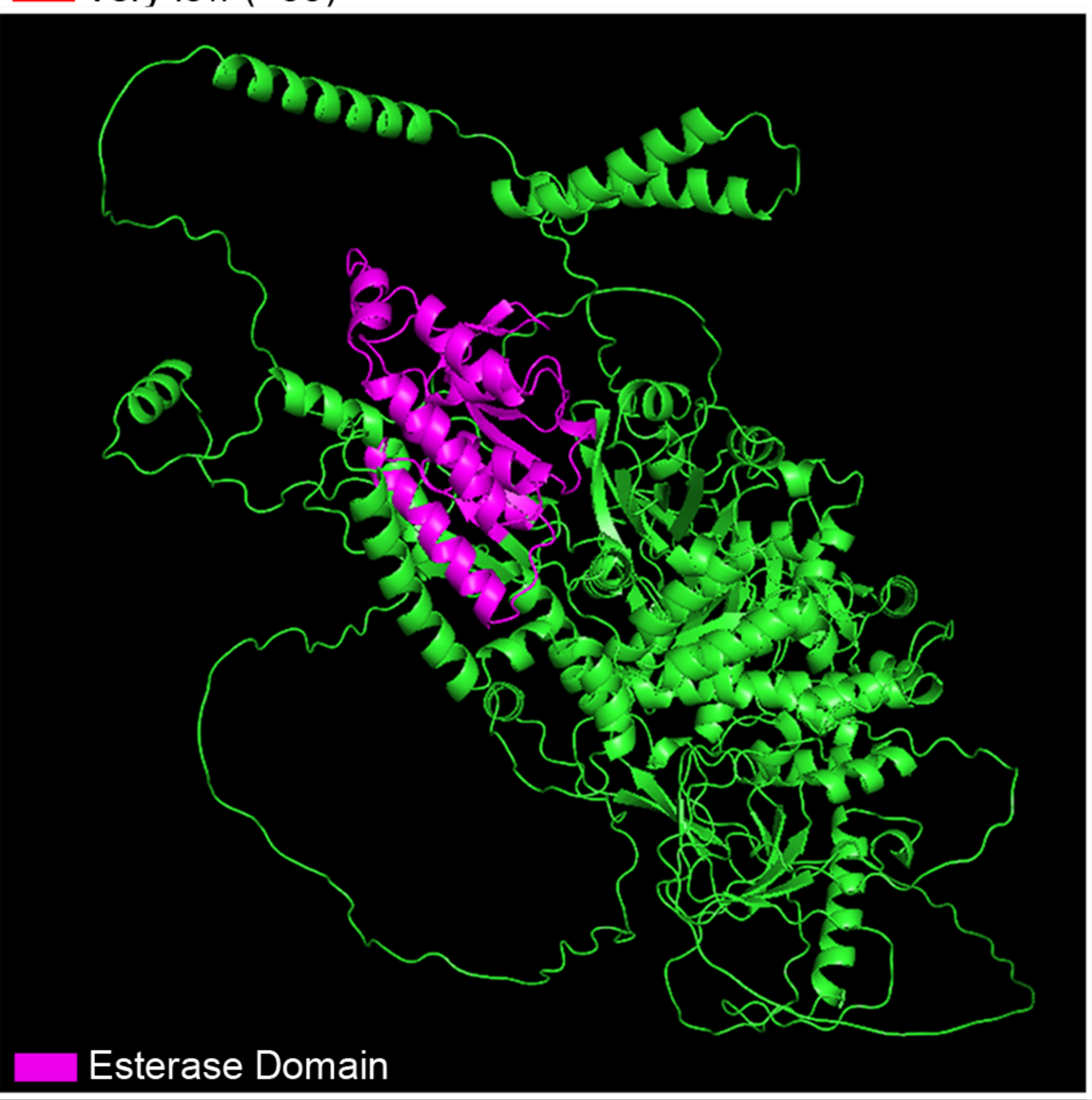

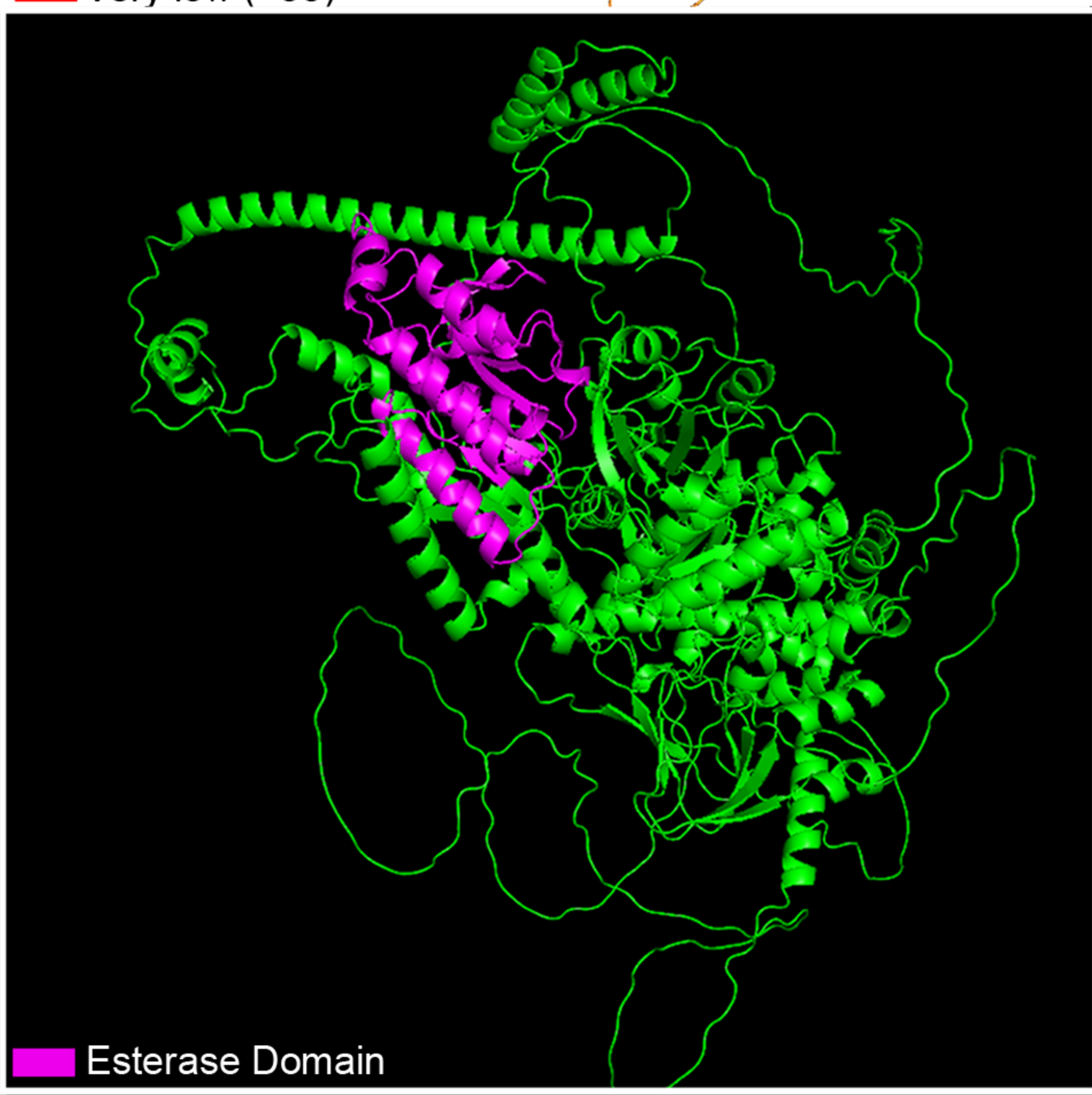

Aligned human NTE and *Drosophila* SWS

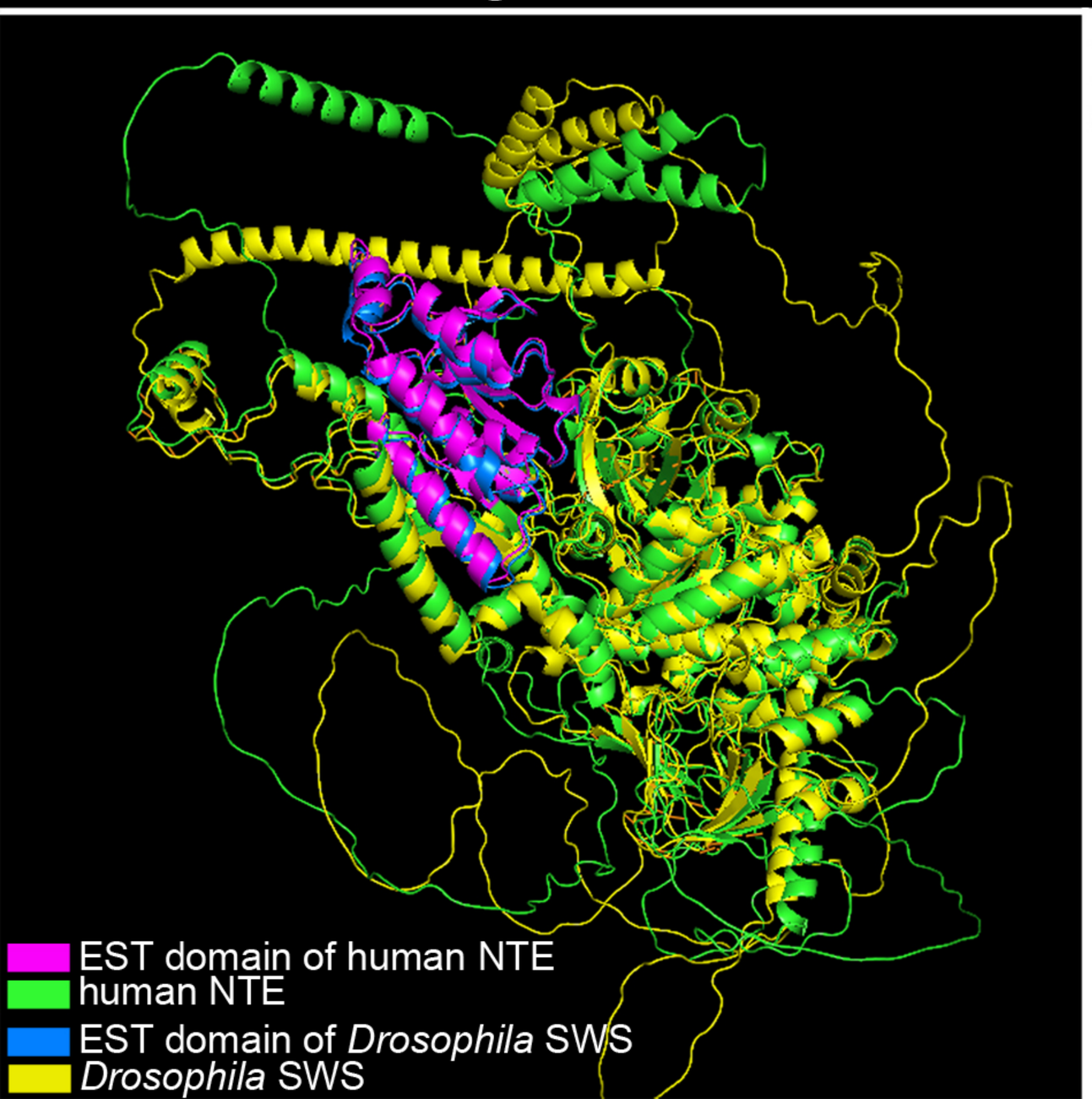


```
NTE  LVLGGGGARGCSHIGVLKALEEAGVPVDLVGGTS    34
SWS  LVLGGGGARGAAHIGMLKAIQEAGIPVDMVGGVS    34
     **********.:***:***::***:***:***.*

     IGSFIGALYAEERSASRTKQRAREWAKSMTSVLE    68
     IGALMGALWCSERNITTVTQKAREWSKKMTKWFL    68
     **:::***:..**. : ..*:****:*.**. :

     PVLDLTYPVTSMFTGSAFNRSIHRVFQDKQIEDL    102
     QLLDLTYPITSMFSGREFNKTIHDTFGDVSIEDL    102
      :******:****:*  **::** .* * .****

     WLPYFNVTTDITASAMRVHKDGSLWRYVRASMTL    136
     WIPYFTLTTDITASCHRIHTNGSLWRYVRSSMSL    136
     *:***.:*******. *:*.:*********:**:*

     SGYLPPLCDPKDGHLLMDGGYINNLPADIAR    167
     SGYMPPLCDPKDGHLLLDGGYVNNLPADVMH    167
     ***:***********:****:******: :
```

A Control

B *sws*^{1}

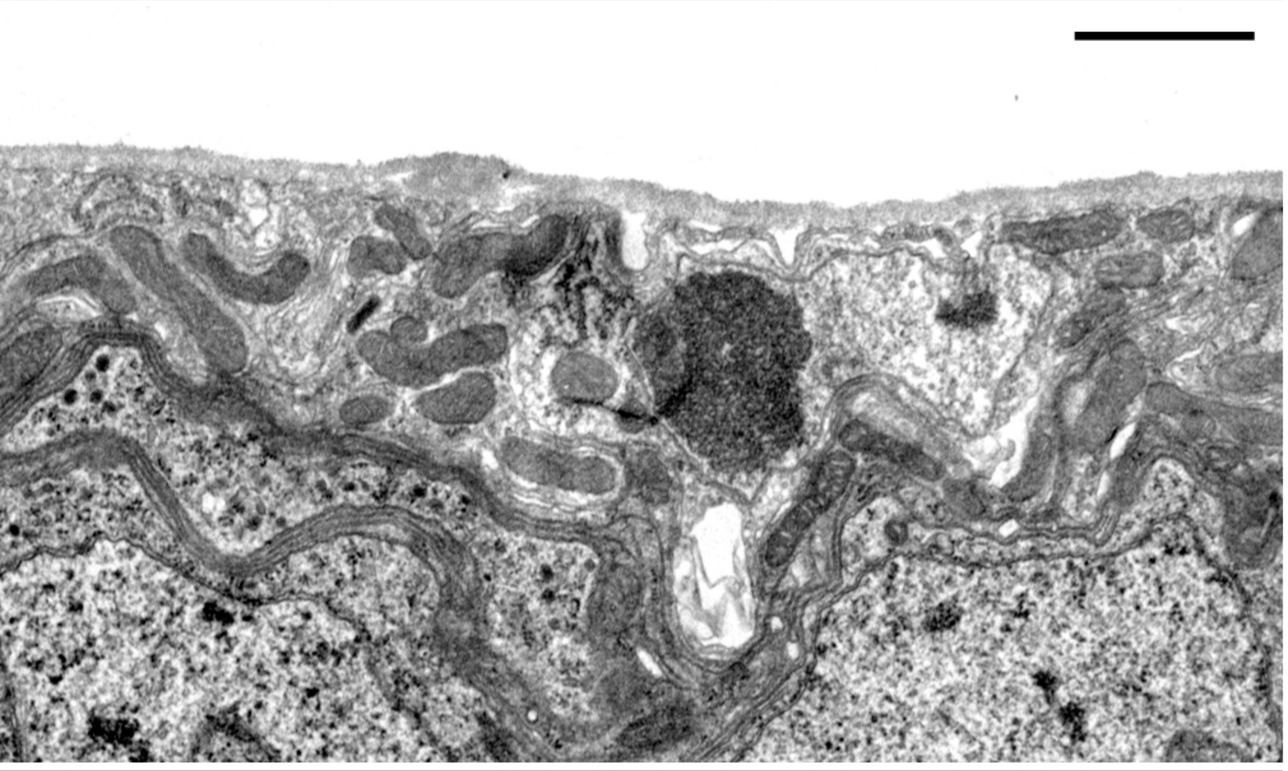

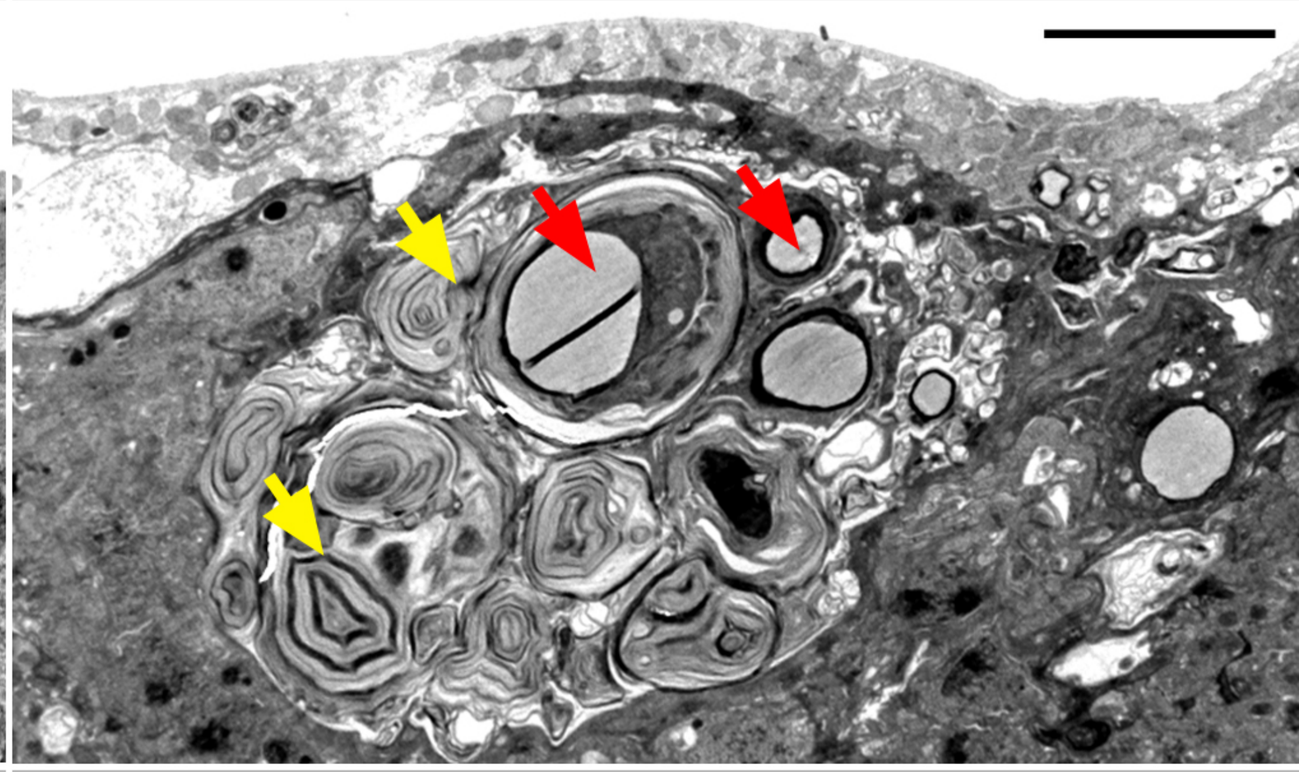

B` *sws*^{1}

C *moody>sws*^{RNAi}

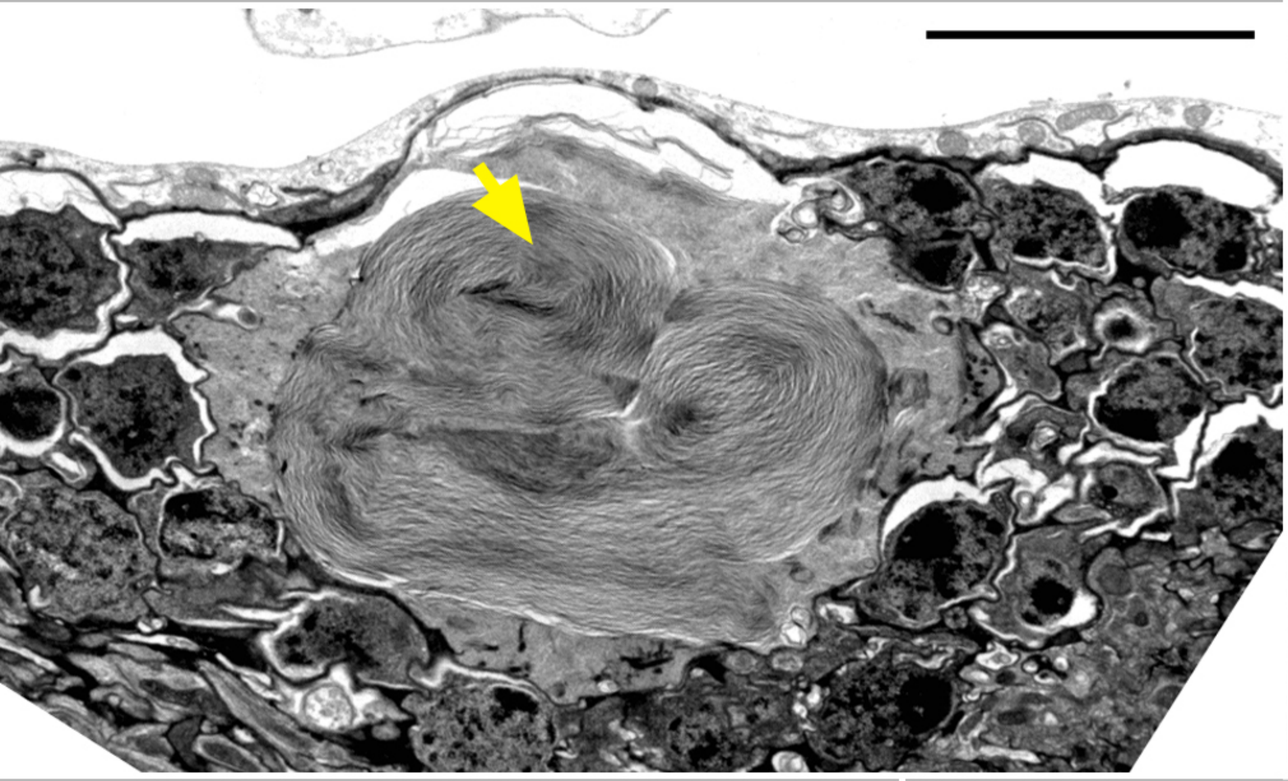

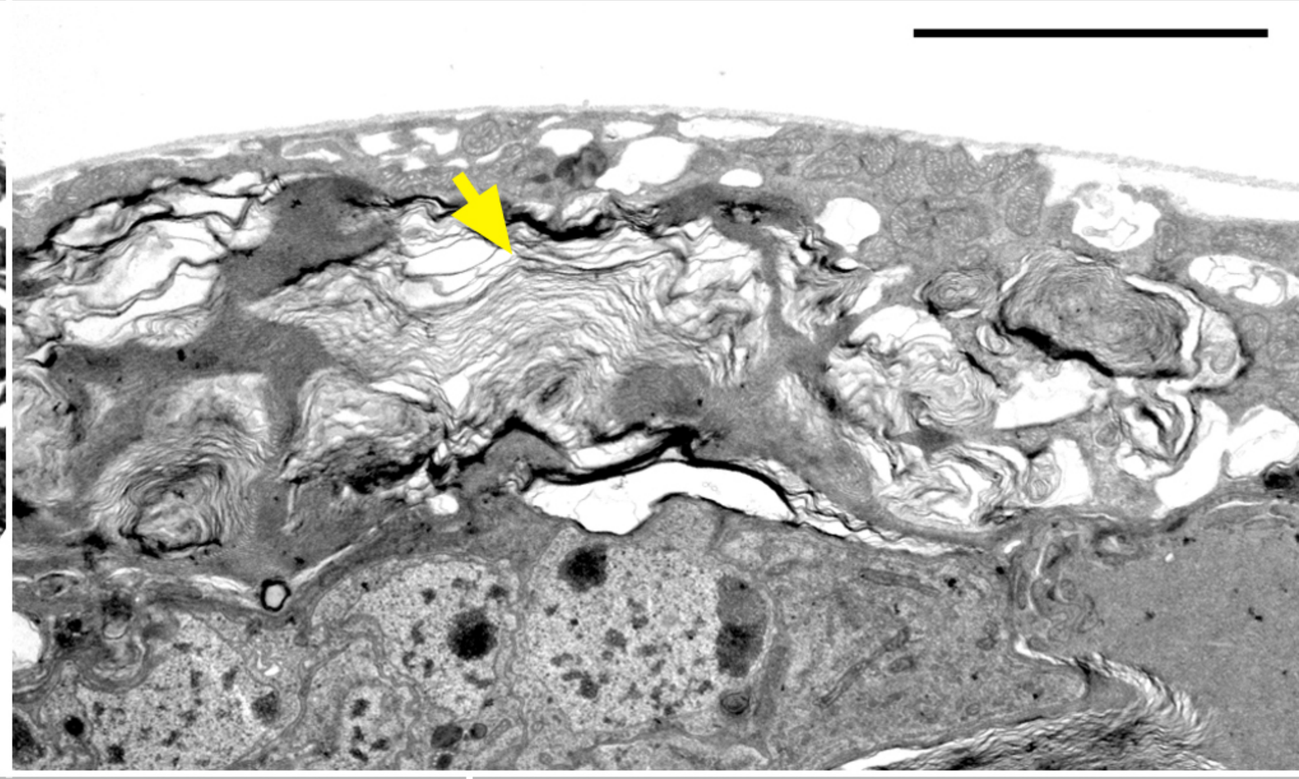

D Control

D` *sws*^{1}

D`` *moody>sws*^{RNAi}

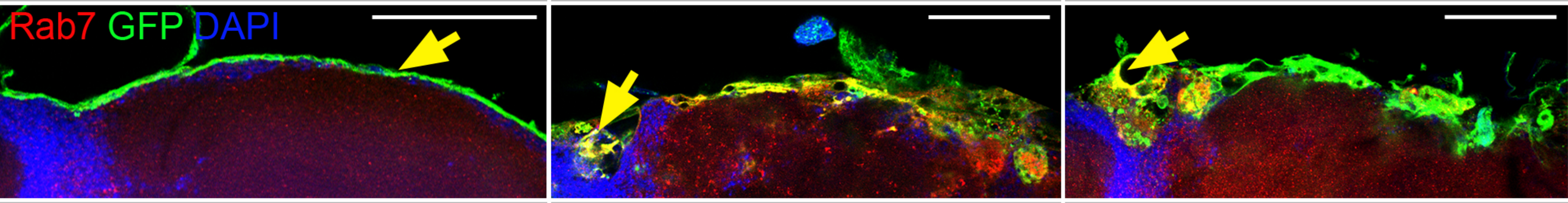

E Control

E` *sws*^{1}

E`` *moody>sws*^{RNAi}

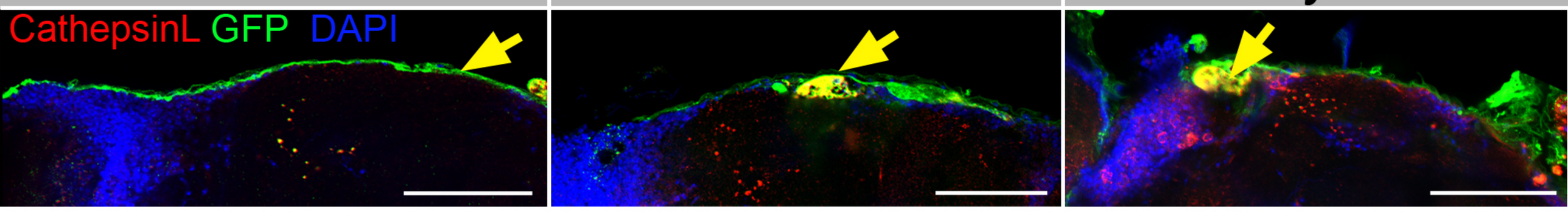

F Rab7 accumulation

G CathepsinL accumulation

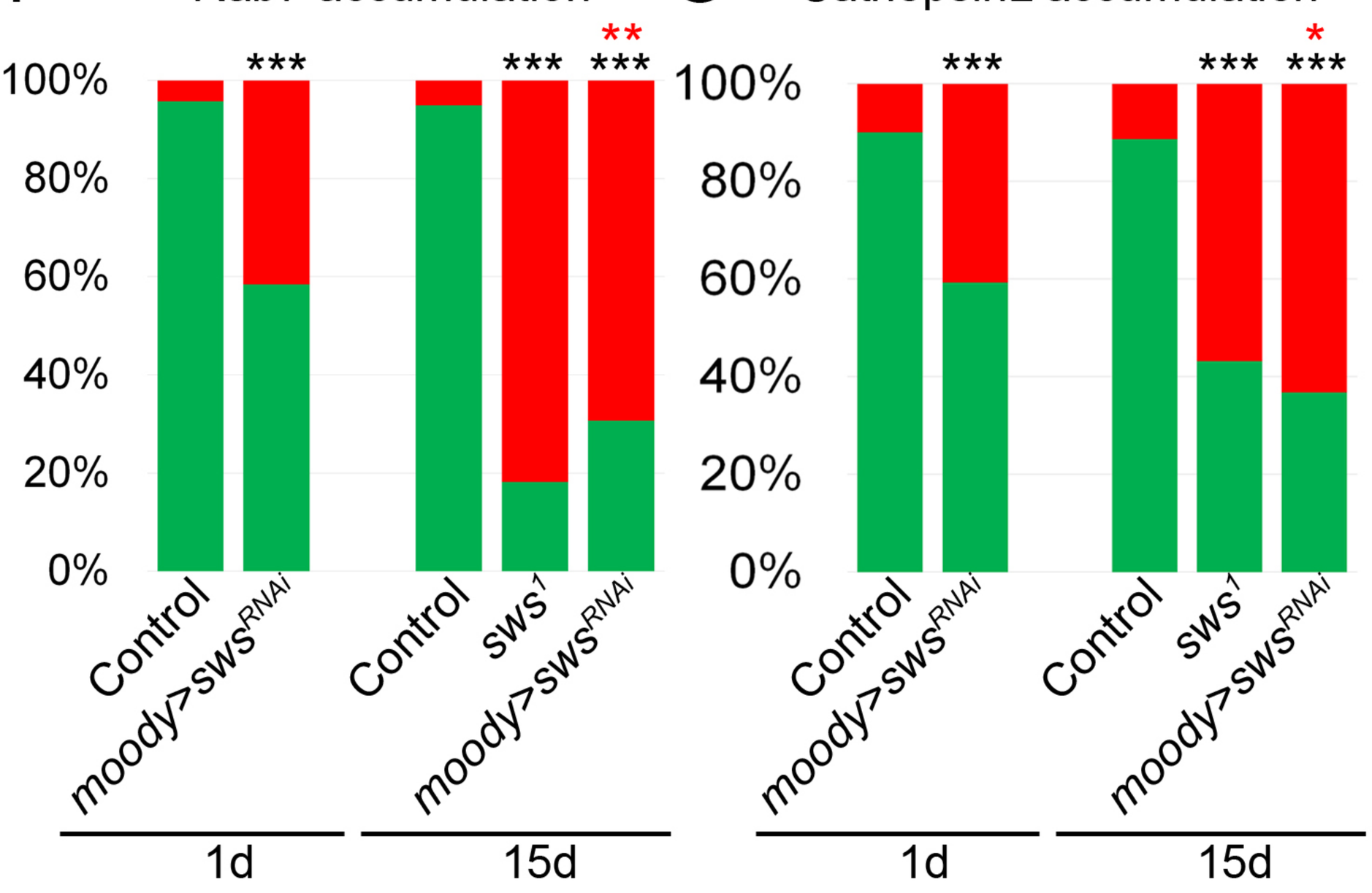

A Dextran injection

>12 hour recovery

Brain dissection

Dextran localization analysis

B Control

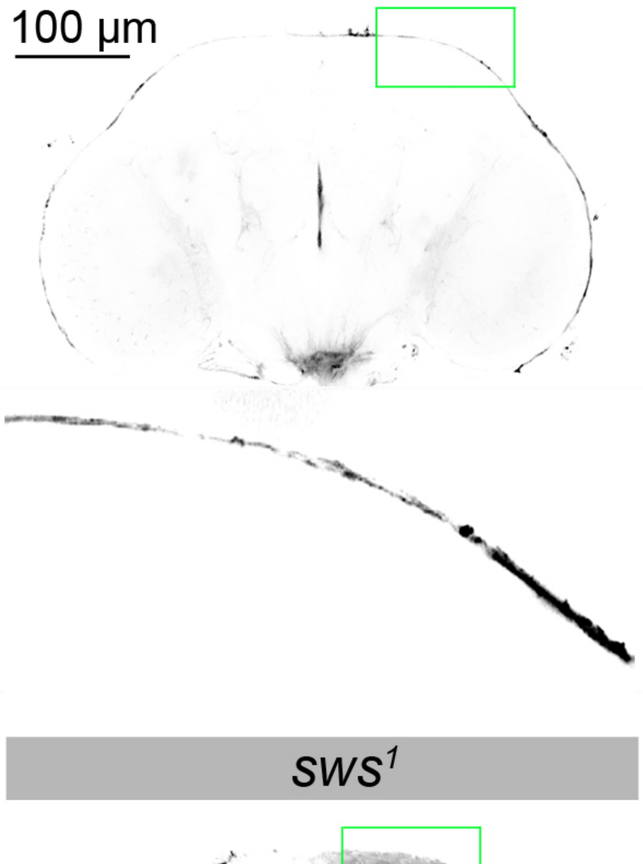

B`

C *sws*^{1}

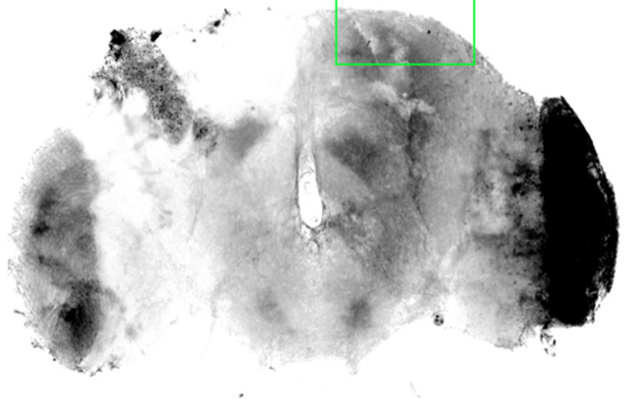

C`

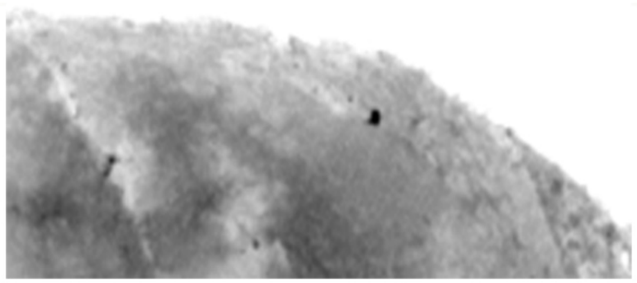

D

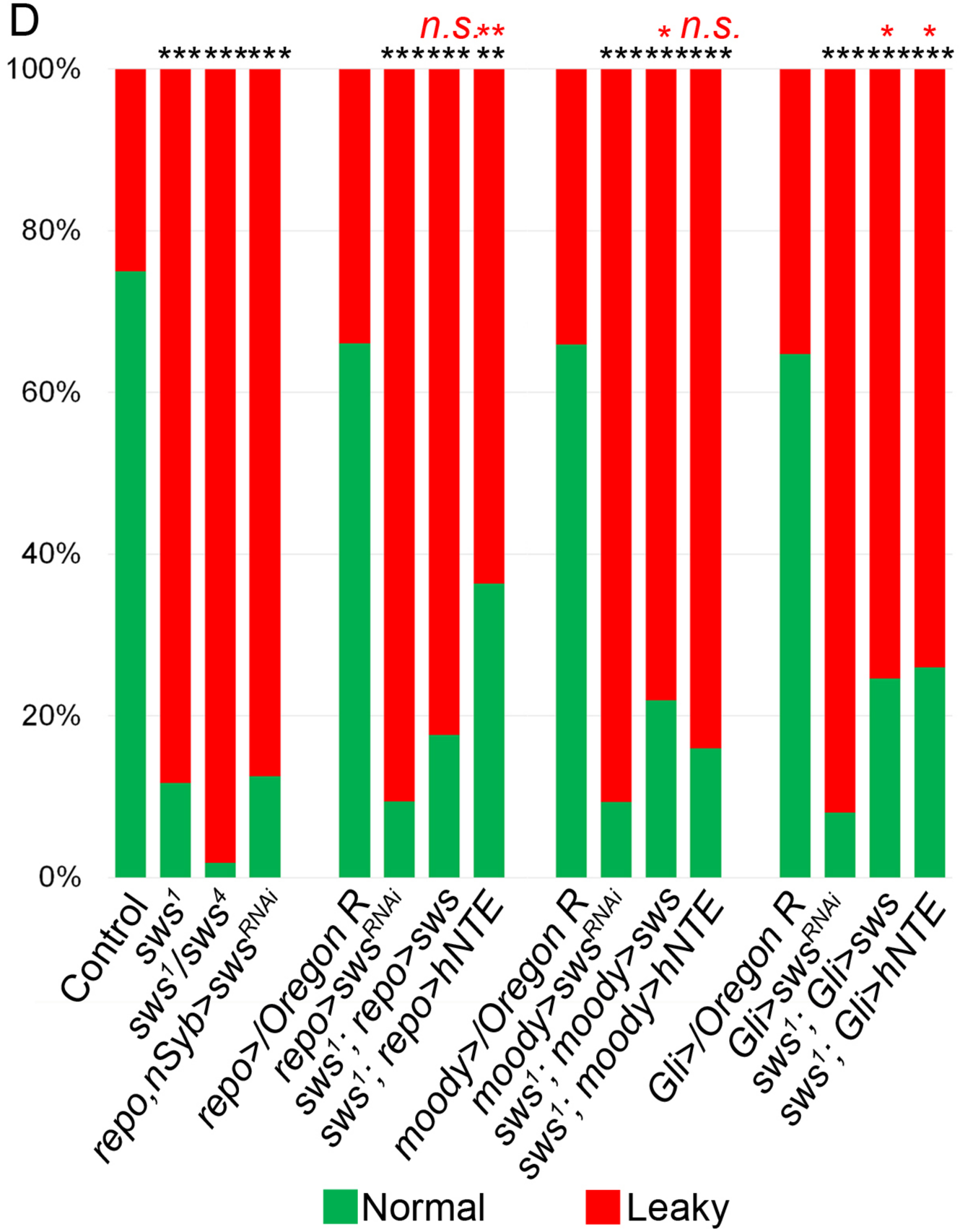

A

inflammation inhibitors reduce glial phenotype in mutants with defective BBB

Delta % of brain hemispheres showed CoraC glial phenotype

sws[1] *moody*[ΔC17]

0% 5% Glucose

*** Sodium Salicylate -30%

** Rapamycin -17%

0% 5% Glucose

* Sodium Salicylate -14%

** Rapamycin -21%

0% -5% -10% -15% -20% -25% -30% -35%

Oregon R *sws*[1]

B

sws and *moody* mutants show upregulated expression of AMPs

Relative mRNA levels

0 1 2 3 4 5 6 7 8

** *** *** *** * *

Attacin A Cecropin A Diptericin

white[1118] *moody*[ΔC17]

C

sws and *moody* mutants show elevated levels of FFA

Relative FA/IS by weight (g)

0 1 2 3 4

*** p=1E-6

*** p=6.7E-9

C14:1 C16:0 C16:1 C18:0 C18:1 C18:2 C18:3 C20:0 C20:4 C20:5

C14:1 - 9-cis-Tetradecenoic acid
C16:0 - Palmitic acid
C16:1 - Palmitoleic acid
C18:0 - Stearic acid
C18:1 - Oleic acid
C18:2 - Linoleic acid
C18:3 - α- and γ-Linolenic acid
C20:0 - Eicosanoic acid
C20:4 - Arachidonic acid
C20:5 - Eicosapentaenoic acid

D

age-dependent increase in AMPs expression is triggered by *sws* loss

Relative mRNA levels

0 10 20 30 40 50 60

15d 30d 15d 30d 15d 30d

Attacin A Cecropin A Diptericin

Oregon R *sws*[1] *sws*[1]; *moody>sws* *moody>*/*Oregon R* *moody>sws*[RNAi]

E

moody>CD8::GFP

NimC1 GFP DAPI 20 µm

NimC1

F

moody>GFP,sws[RNAi]

NimC1 GFP DAPI

NimC1

G

NTE/SWS

Moody

Defective BBB & Elevated FFA levels

Inflammaging

NSAID

A Drug feeding assay

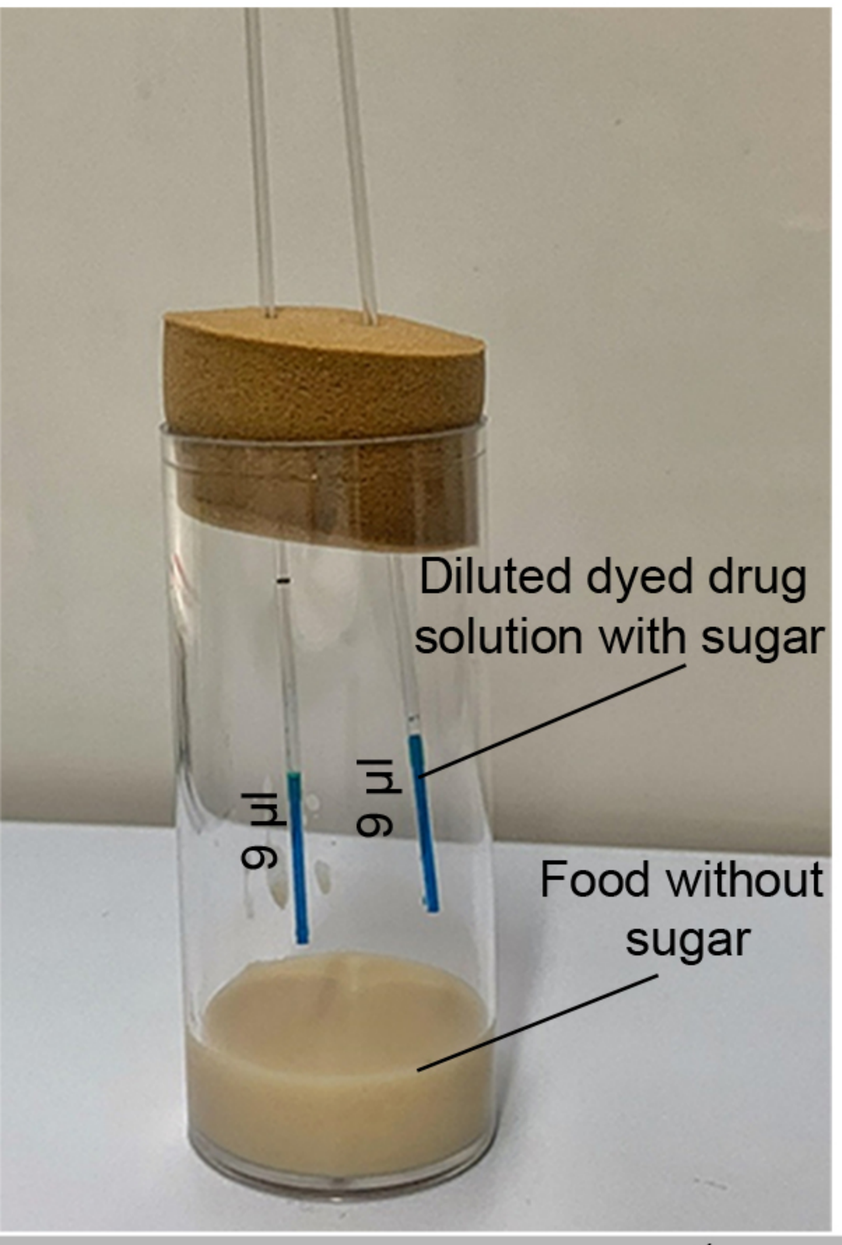

B Anti-inflammatory drugs partially suppress glial phenotype in *sws* mutant

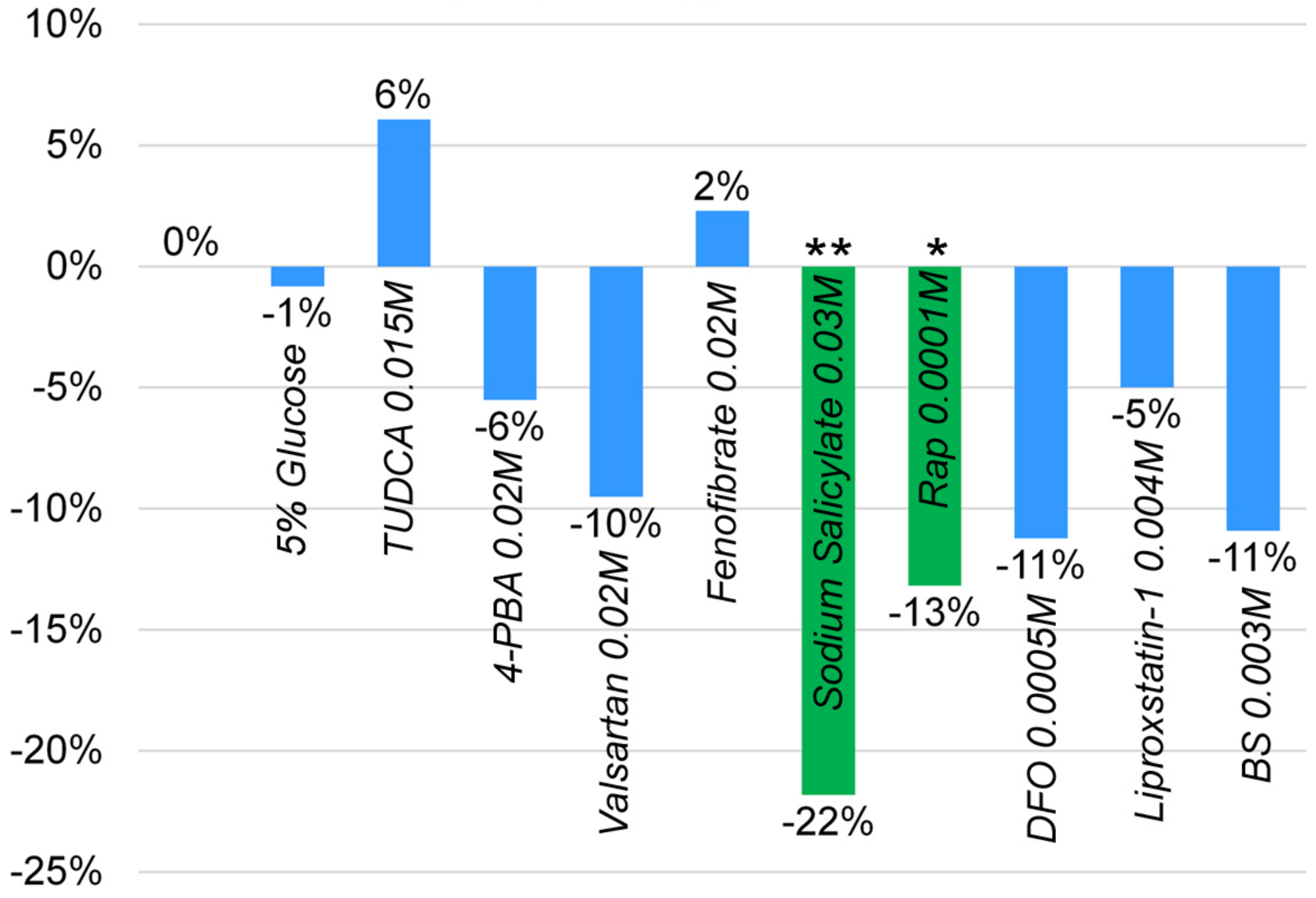

sws[1] | *moody*[ΔC17]

C 5% Glucose | C` Sodium Salicylate | D 5% Glucose | D` Sodium Salicylate

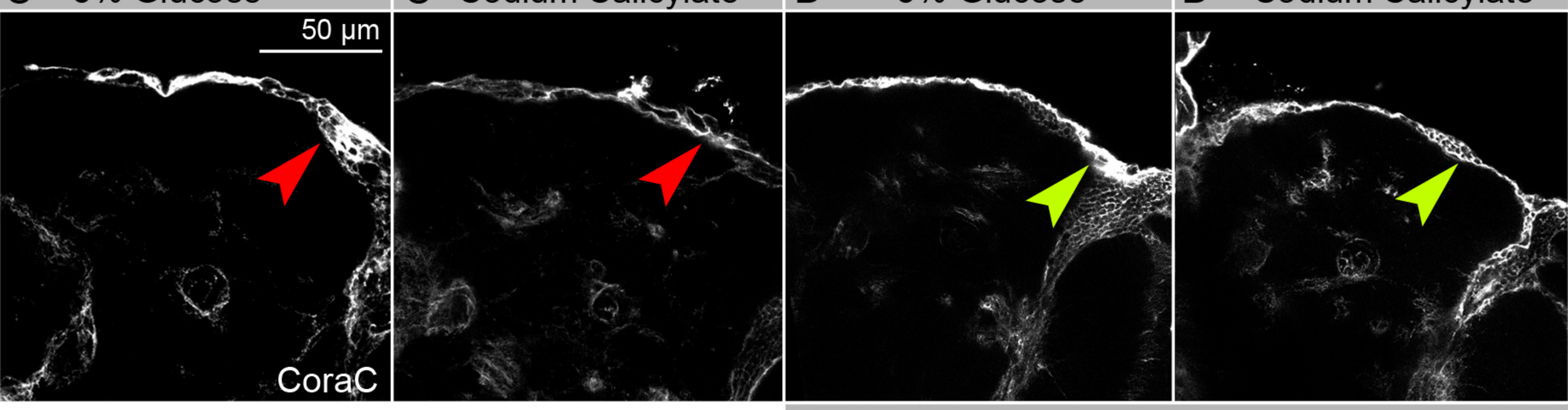

E *sws* downregulation after BBB formation induces inflammation

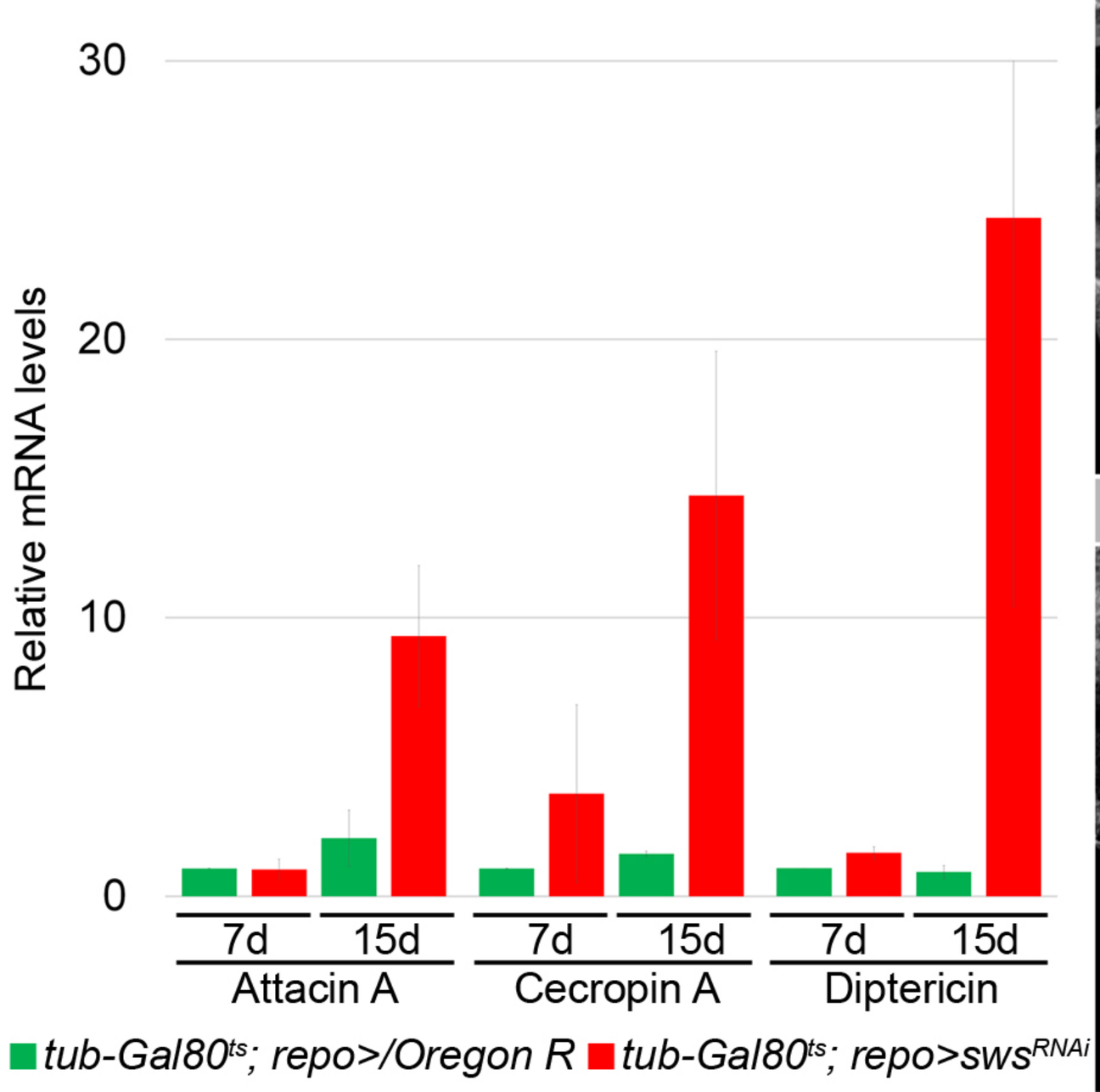

F *OR; srp(Hemo)>mCherry*

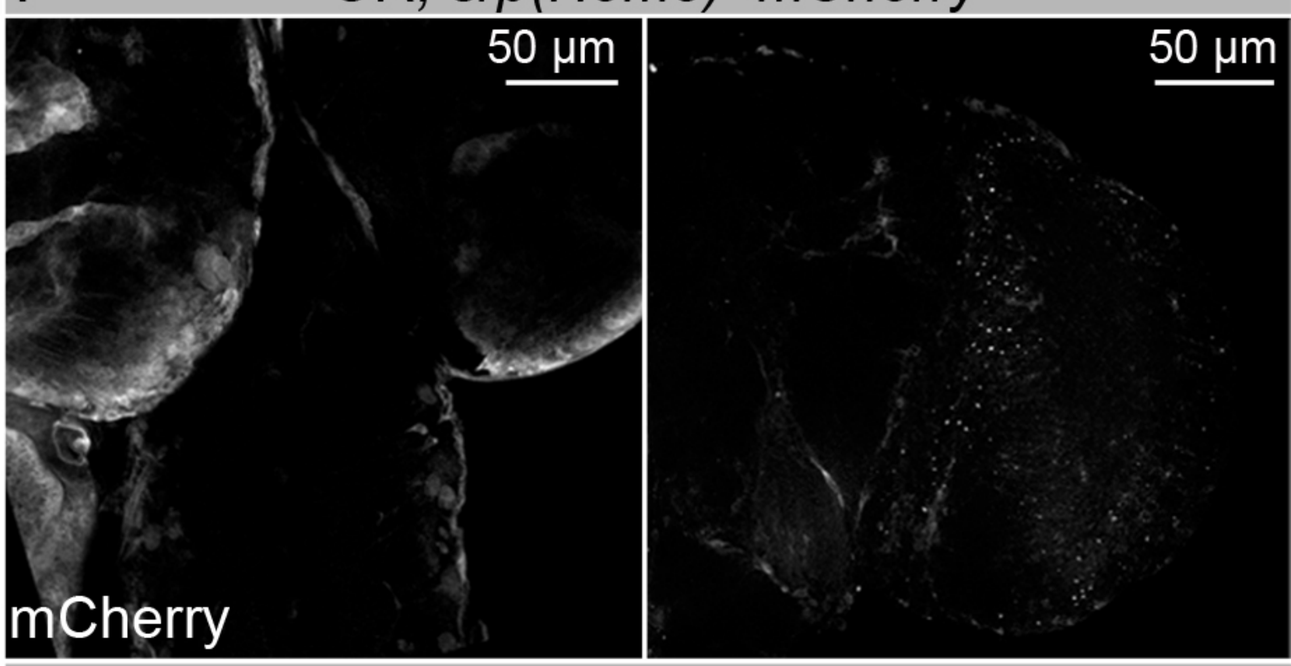

G *sws*[1]*; srp(Hemo)>mCherry*

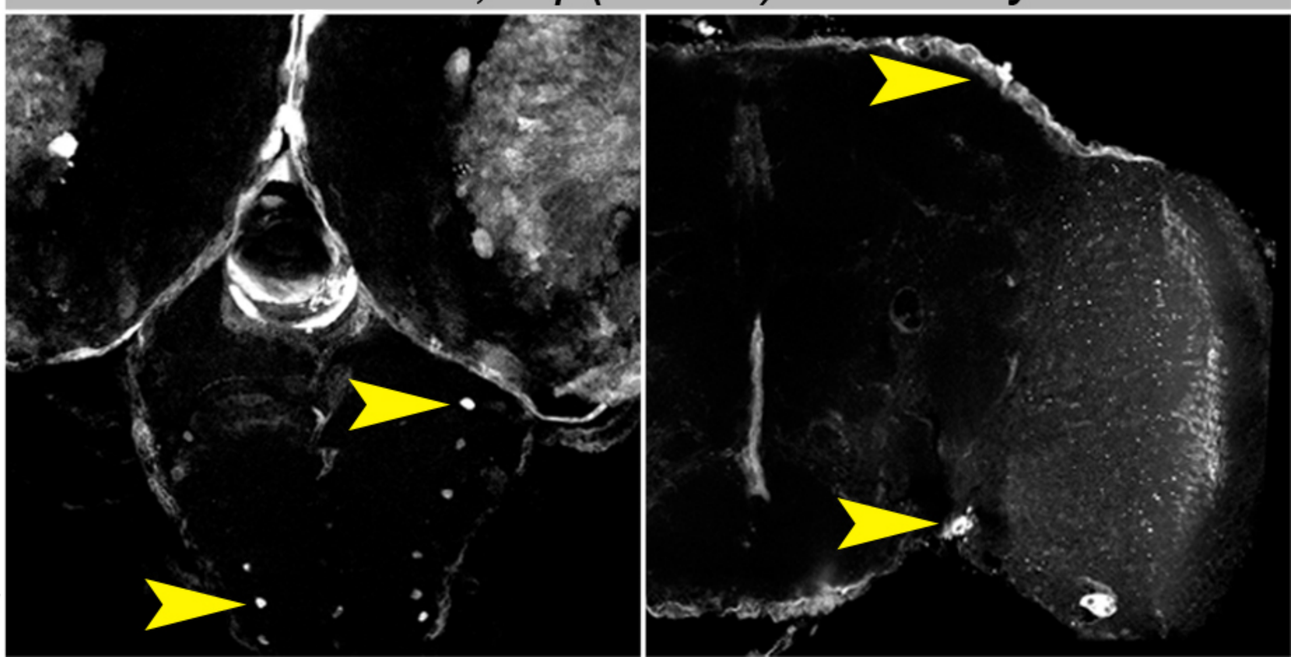

CoraC

A Control

20 µm

B *moody*$^{\Delta C17}$

C *moody>moody*^{RNAi}

D

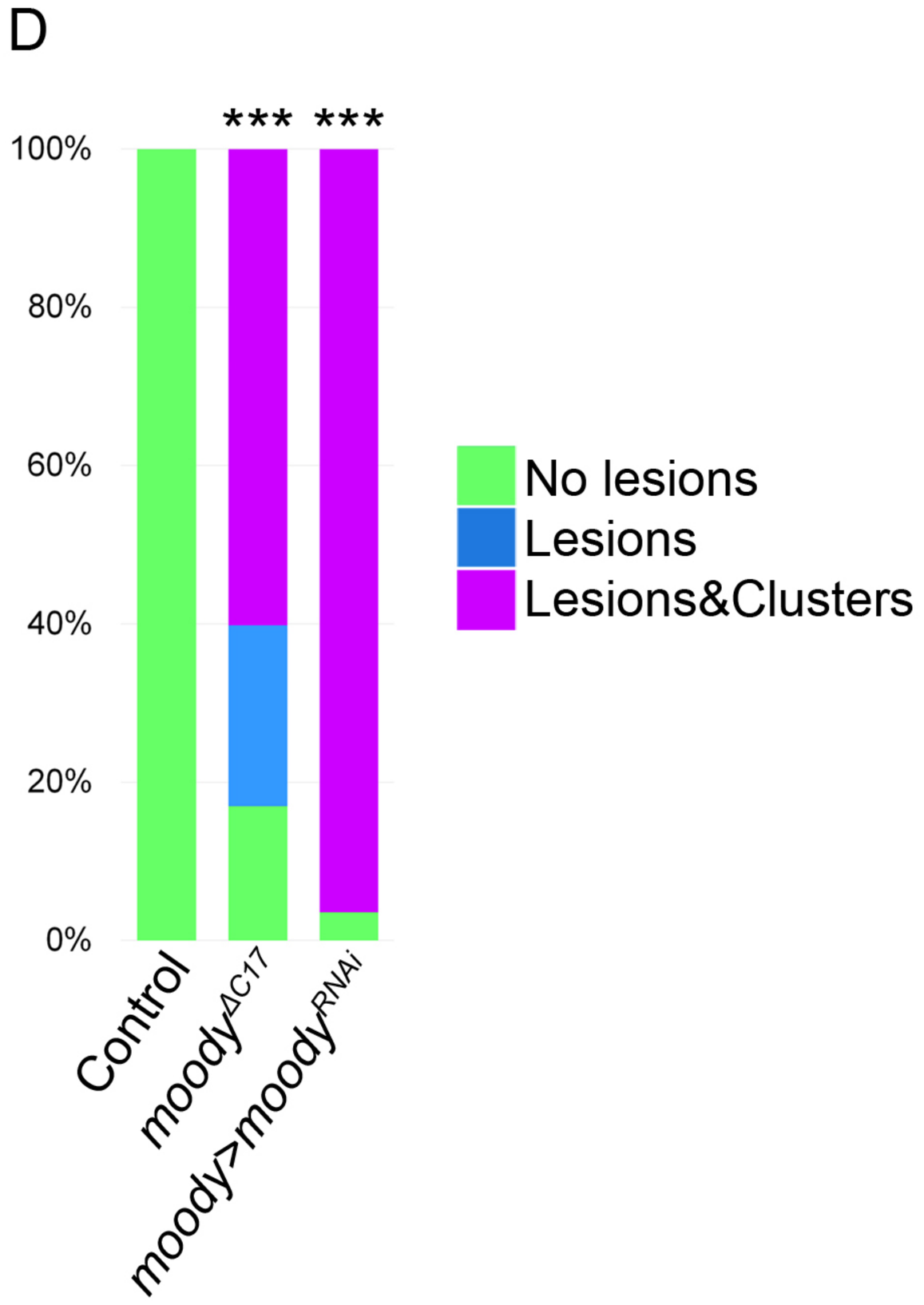

EM

E Control

F *moody*$^{\Delta C17}$

Rab7 NrxIV DAPI

G

20 µm

H

Rab7

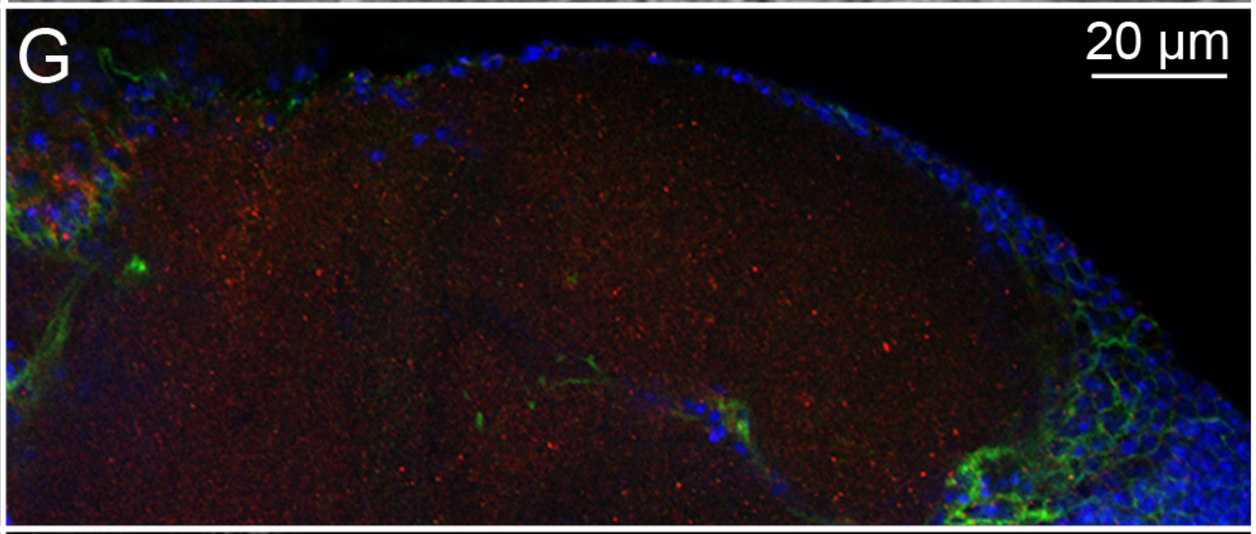

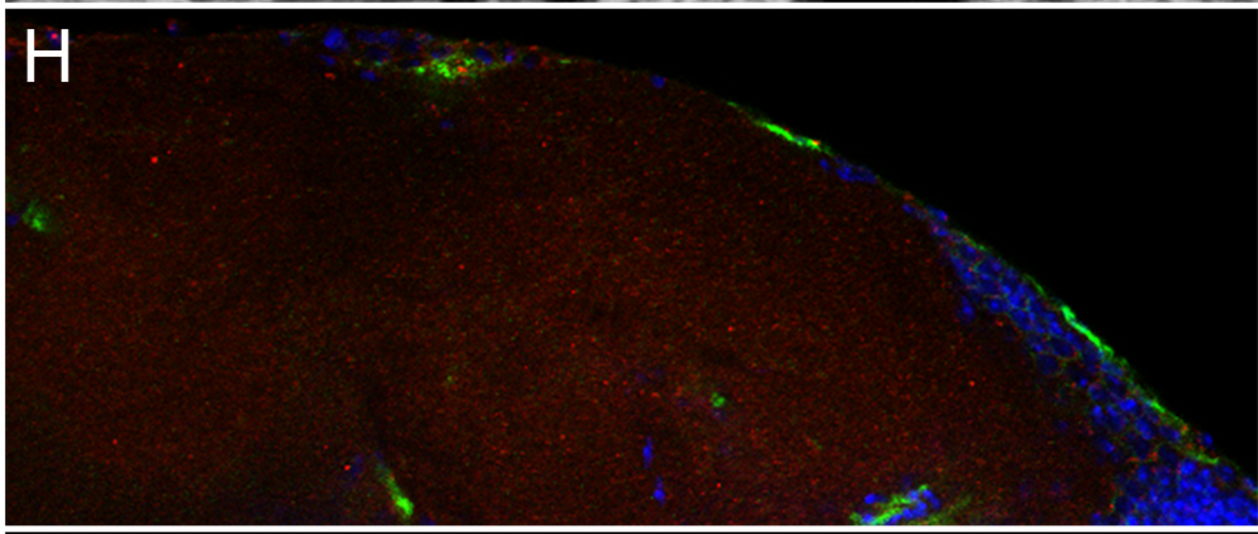

The internal standart does not contribute to Arachidonic acid (AA)

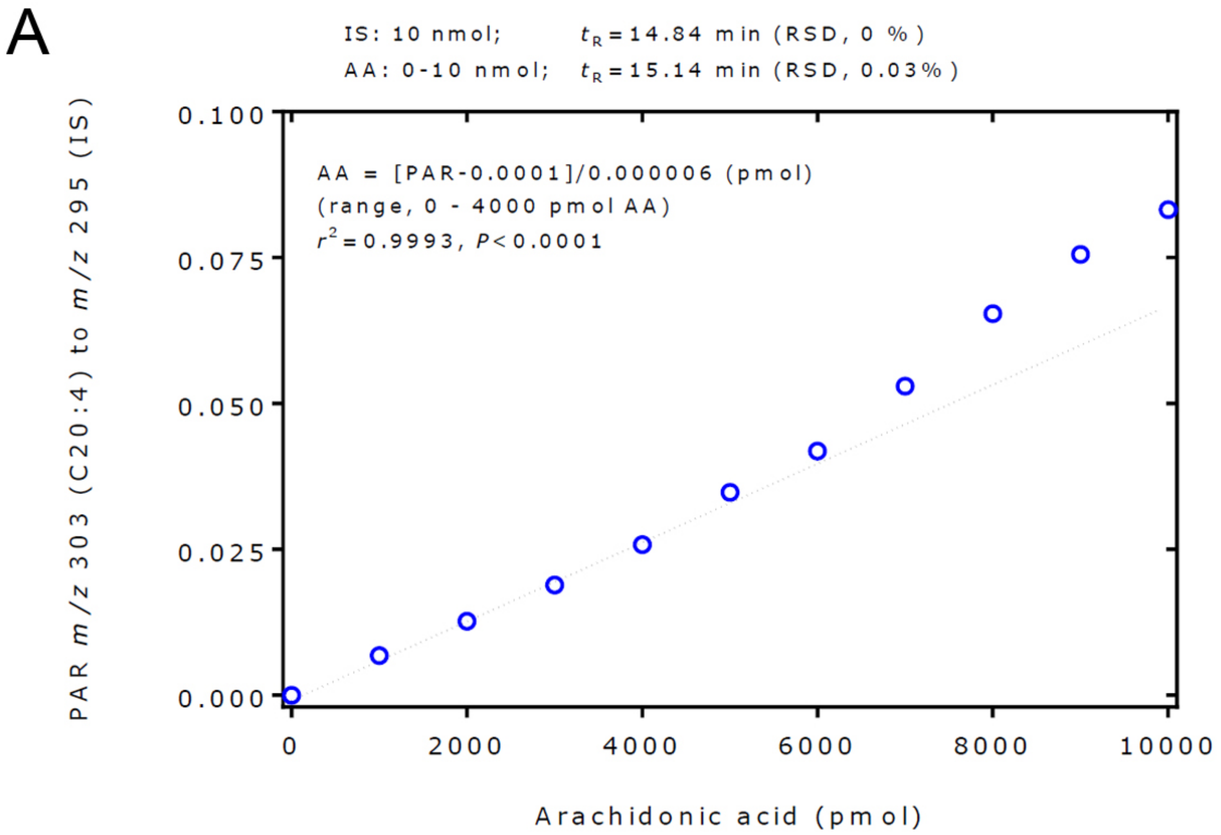

Peak area ratios of free fatty acids (FFA) to the internal standard (IS) obtained from GC-MS analysis

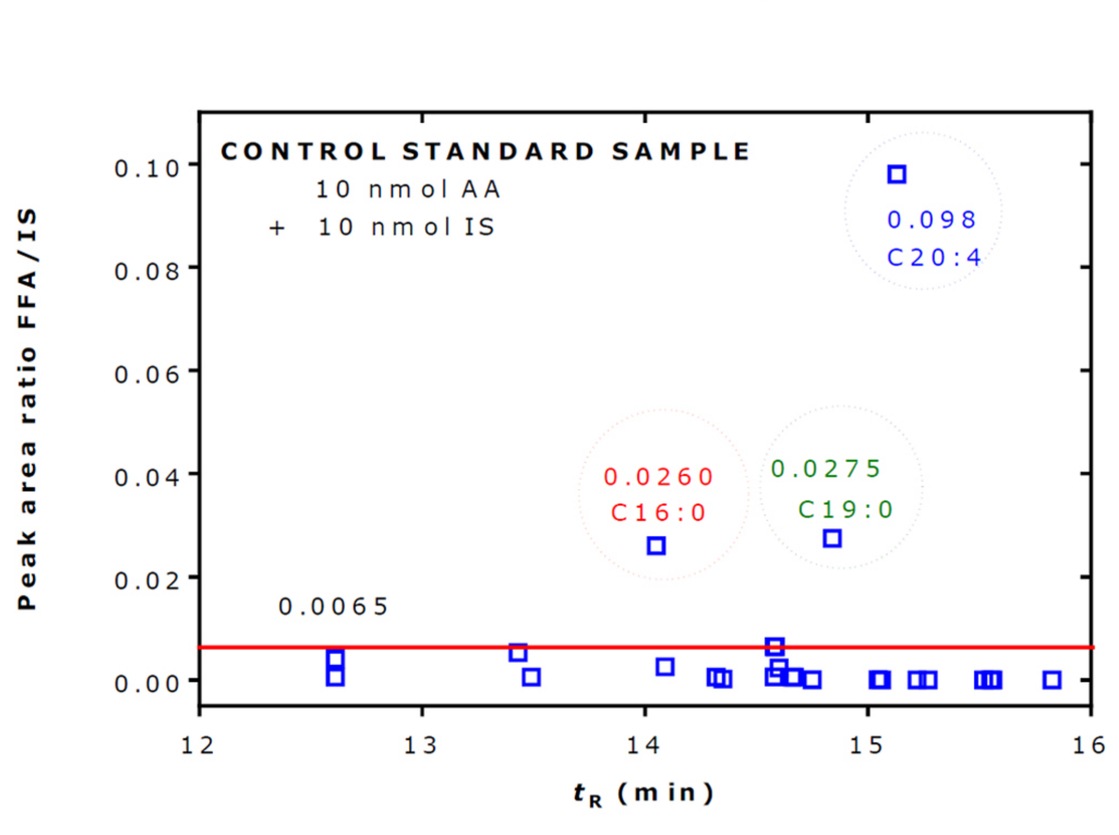

A

Control

NrxIV

Hemolymph

Neural lamella

SJs

PG

SPG

Lysosomes

Neuron

Cortex glia

Membrane domains

B

moody$^{\Delta 17}$

Defective SJs

Membrane domains

C

sws^{1}

Defective SJs

Defective lysosomes

Disorganized membrane domains

D Control

E *sws*^{1}

F *sws*^{1}